University of Nottingham
UK | CHINA | MALAYSIA

Not Dead Yet: High Redshift Recently Quenched Galaxies As Probes Of Galaxy Evolution

Elizabeth Taylor

Thesis submitted to the University of Nottingham
for the degree of Doctor of Philosophy

July 2024

I know nothing with any certainty, but the sight of the stars makes me dream

– Vincent Van Gogh

Supervisors:	Prof. Omar Almaini	
	Prof. Michael Merrifield	
	Dr. David Maltby	
Examiners:	Prof. Jim Geach	(University of Hertfordshire)
	Prof. Nina Hatch	(University of Nottingham)
Submitted:	29th July 2024	
Examined:	2nd October 2024	
Final version:	2nd January 2025	

Contents

Abstract

In this thesis, we explore the roles that galaxy environment, stellar mass and outflows play in the quenching of star formation, by studying recently quenched galaxies at cosmic noon and beyond ($0.5 < z < 4.4$). We utilise photometric data from the UKIDSS Ultra Deep Survey (UDS), the deepest NIR survey over $\sim$1 deg^2, which has sufficient volume to enable samples to be split by stellar mass, redshift and environment. Additionally, we use spectroscopic data for galaxies within the UDS field, from deep observations at ESO VLT (UDSz, VANDELS) and JWST NIRSpec (EXCELS), to study galactic scale winds in the interstellar medium.

We conduct the first study of how the relative quenching probability of galaxies depends on environment over the redshift range $0.5 < z < 3$. By constructing the stellar mass functions for quiescent and post-starburst (PSB) galaxies in high-, medium-, and low-density environments, we find an excess of quenched galaxies in dense environments out to at least $z \sim 2$. Using the growth rate in the number of quenched galaxies, combined with the star-forming galaxy mass function, we calculate the probability that a given star-forming galaxy is quenched per unit time. We find a significantly higher quenching rate in dense environments (at a given stellar mass) at all redshifts. Massive galaxies ($M_* > 10^{10.7}$ $M_\odot$) are on average 1.7 ± 0.2 times more likely to quench per Gyr in the densest third of environments compared to the sparsest third. Finally, we compare the quiescent galaxy growth rate to the rate at which galaxies pass through a PSB phase, finding that the PSB route can explain $\sim$ half of the growth in the quiescent population at high stellar mass, and potentially all of the growth at lower stellar masses.

We then use optical spectra of galaxies selected from the UDS at $z > 1$ to explore the transition in outflow properties along a quenching time sequence. To do this, we perform a stacking analysis of Mg II absorption profiles, investigating outflow velocities as a function of time since the last major burst of star formation (t_{burst}). We find evidence for high-velocity outflows ($v_{out} \sim$ 1000 - 1500 kms^{-1}) in a star-forming progenitor population and for recently quenched galaxies with $t_{burst} < 1$ Gyr. The oldest galaxies ($t_{burst} > 1$ Gyr) show no evidence for significant outflows. Our samples show no signs of AGN in optical observations, however the presence of significant outflows in the older quenched galaxies ($t_{burst} > 0.6$ Gyr) is difficult to explain with starburst activity alone, and may indicate energy input from episodic AGN activity as the starburst fades.

Finally, we complement our ground-based stacking analysis using the JWST NIRSpec

EXCELS survey. We select a sample of 9 post-starburst galaxies in the redshift range $1.8 < z < 4.4$, and utilise the high resolution spectra to establish, for the first time, if outflows are prevalent in post-starburst galaxies at earlier epochs than cosmic noon. The large wavelength coverage and unique sensitivity of JWST allows us to compare outflow properties for both the Mg II and Na D absorption profiles. We first perform a stacking analysis of our sample, finding ~ 1600 kms^{-1} and ~ 290 kms^{-1} outflows from the magnesium and sodium profiles, respectively. We use these outflow velocities to estimate lower limits on the mass outflow rates, of $\dot{M}_{\mathrm{out,\,MgII}} \sim 1\ \mathrm{M}_{\odot}\mathrm{yr}^{-1}$ and $\dot{M}_{\mathrm{out,\,NaD}} \sim 3\ \mathrm{M}_{\odot}\mathrm{yr}^{-1}$, higher than the average SFR of our sample. We then investigate galactic scale winds for individual objects at $z \sim 3$, finding a wide range of outflow velocities, with some galaxies also showing signs of inflowing gas. These results suggest that outflows may play a key role in the quenching of galaxies at these epochs, by removing the gas needed to fuel star formation.

Acknowledgements

First and foremost, I'd like to express my deepest thanks to my Ph.D supervisors, Omar and Mike. Your guidance and support have been crucial and unwavering during the past four years, on both a personal and an academic level. I am very fortunate to have benefited from your wealth of expertise, experience and insight. Additionally, I am sincerely grateful to Dave, for the patience and knowledge you have shared with me throughout my Ph.D – I cannot thank you all enough.

To the wider UDS group, thank you for your collaboration and genuine interest, no matter how many times you saw the same galaxy spectrum. Lizzie E, Karel, Jimi and Tom, you have been fabulous. I also wish to thank my collaborators Kate and Vivienne, for making me feel so welcome during my visits, and for your invaluable feedback. I am very grateful to the rest of the staff at CAPT for your endlessly helpful scientific discussion, and delicious cakes on a Friday afternoon. Phil, thank you for always sorting my little computer issues, and Ella, thank you for your help in getting my attendance to various conferences sorted.

My Inflativerse gang – Roan, CB, Kellie, Jimi, Jen and Fiona: thank you for all the fun, encouragement and debriefings after every wild school visit. To my friends and office mates throughout the years: Mick, Roan, Jacob, Karel, CB, Dan, Kellie, Jimi, Jen, Callum, Matt, Julian and so many more – you have made this worth it 10 times over. Special thanks go to Kellie, Karel and CB, for always finding time for a girls night and a laugh – I adore you. Grace, thank you for being the best housemate and friend anyone could have asked for. Sophie, Charlotte, James, Harry and Leo: I have experienced endless joy with you guys. Lauryn, Maisie and Jordan – Saturday club is a force to be reckoned with, and I cherish you girls.

To my family: I will never be able to express how much your love, support and humour has buoyed me throughout these past four years. Granny, Granddad, all my aunts, uncles and cousins – thank you. Pip, thanks for putting up with my constant petting, and for not bringing in *too* many mice at 4 a.m. recently. Annie, you inspire me every day, both with your passion and paintings, and with your tales in the group chat. Patrick, I am forever grateful for your wisdom, wit and scathing remarks about my tiny hands. Mum, I am so lucky to have your compassion, badly spelled texts and infinite belief in me, always.

I could not, and would not, have done this without my greatest support, Alex. You have

been, and continue to be, my biggest cheerleader, my favourite chef, and an incredible person. For everything, thank you.

Finally, to my Dad. You are my hero, and this is for you. I love and miss you, always. Cheers.

Published works

The majority of the material presented in this thesis has already been published in — or has been submitted to — a journal as the following works.

I **Taylor, E.**, Almaini O., Merrifield M., Maltby D., Wild V., Hartley W. G., Rowlands K., 2023, MNRAS, 522, 2297: *'The role of mass and environment in the build-up of the quenched galaxy population since cosmic noon'*.

II **Taylor, E.**, Maltby D., Almaini O., Merrifield M., Wild V., Rowlands K., Harrold, J., 2024, MNRAS, submitted: *'Not dead yet: high-velocity outflows seen in old $z > 1$ recently-quenched galaxies with no AGN signatures'*.

Chapter 2 is based on material published in Paper I. Chapter 3 is based on material from the forthcoming Paper II.

The vast majority of work presented here was carried out by the author, with advice from the paper authors above. Where the work contains the product of larger collaborations, this is mentioned in the relevant chapter.

Chapter 1

Introduction

Despite thousands of years of humanity speculating on the nature of the Universe, it was only in the 1920s that astronomers first concluded that separate 'island universes', or galaxies, exist outside of our own Milky Way. In 1924, following the 'Great Debate' between Harlow Shapley and Herber Curtis, Edwin Hubble used the distance to Cepheid variable stars to show that Andromeda was indeed far beyond the Milky Way (Hubble, 1925a,b). Since then, the advent of whole sky surveys and space telescopes has led to a wealth of new discoveries within the field of extra-galactic astronomy. However, there is still much left to be understood – one such puzzle is how and why galaxies stop forming stars.

1.1 Galaxy Classification and Bimodality

In general, the baryonic matter within a galaxy is contained either in stars or the gas and dust in between (the interstellar medium, ISM). Hotter, younger stars are generally more luminous and massive, with shorter lives and bluer colours, while older stars tend to be cooler, smaller and redder in colour. The stellar makeup of a galaxy largely influences its colour and structure; highly star-forming, gas-rich galaxies are generally blue with spiral structures, and a galaxy which is primarily red in colour is likely to be passive and no longer forming new stars. There are numerous methods used by astronomers to classify galaxies based on their appearances and internal properties (e.g. morphology,

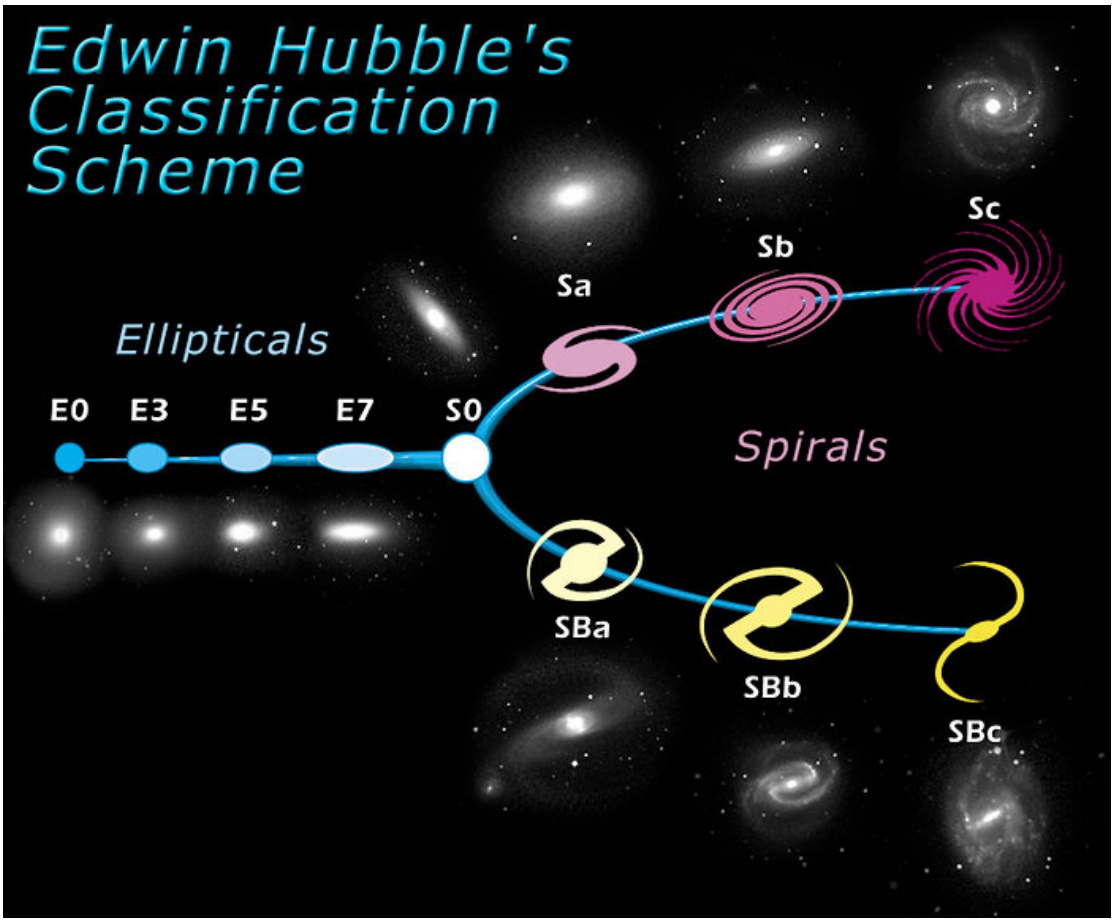

Figure 1.1: The Hubble sequence, or Hubble tuning fork (first described in Hubble, 1936), accompanied by images of real galaxies. Elliptical galaxies (early-types) are to the left of the diagram, designated the letter 'E', and become less elliptical towards the centre of the fork. Spiral galaxies (late-types) are to the right, with non-barred spirals ('S') along the top and barred spirals ('SB') along the bottom. Lenticular ('S0') galaxies lie at the centre of the diagram. *Image credit: NASA & ESA*

colour, star formation rate and spectral characteristics), and these are outlined below.

1.1.1 Morphology

One of the earliest classification schemes used for extragalactic objects is the Hubble sequence (Hubble, 1936, see Figure 1.1), based on a galaxy's observed structure. Hubble classified galaxies into two broad groups: early- and late-types. Early-type galaxies (ETGs) are those with elliptical or lenticular ('S0') morphologies, and late-type galaxies (LTGs) have spiral structures. Elliptical ('E') galaxies have smooth, often featureless

light distributions and spheroidal shapes, while spiral galaxies have flat disks with spiral arm structures. Spiral galaxies are further split into those with bars extending from the central bulge ('SB') and those without ('S'). S0s show features in between the two former categories, with bright, central bulges resembling elliptical galaxies, surrounded by a non-spiral disk.

Morphology can vary with wavelength, as stellar populations with different colours generally reside in different parts of a galaxy. This variation can also be due to dust extinction, which preferentially attenuates light at UV wavelengths. Since young, hot OB stars emit huge amounts of radiation in the UV, star-forming galaxies are generally more affected by dust extinction than passive galaxies with little to no ongoing star formation (e.g., Bohlin et al., 1991; Taylor-Mager et al., 2007).

1.1.2 Colour

Galaxy colours are one of the most easily determined properties, and contain important information about the star formation history of the object. Optical colours are broadly correlated with Hubble type, with spiral galaxies being generally blue in colour and ellipticals being red. The correlation of morphology, color and stellar populations has long been studied (e.g. Humason, 1936), but the advent of massive surveys such as the Sloan Digital Sky Survey (SDSS, York et al., 2000) allowed detailed studies of vast numbers of galaxies. A strong bimodal distribution of galaxies in colour-colour and colour-magnitude space is seen (Strateva et al., 2001; Baldry et al., 2004; Bell et al., 2004; Schawinski et al., 2014, see Figure 1.2), with the two peaks corresponding roughly to early-types (termed the 'red sequence') and late-types (the 'blue cloud'). This bimodality has since been found to hold out to $z \sim 2.5$ (Franzetti et al., 2007; Williams et al., 2009; Brammer et al., 2009). The region between the red sequence and blue cloud in colour-magnitude space is thought to be inhabited by galaxies transitioning between the two populations, and is commonly referred to as the 'green valley'.

The interpretation of colour can be complicated, however, by two additional factors: (i) dust, as described in Section 1.1.1, and (ii) galaxy metallicity. Metal-rich stars appear redder than metal-poor stars, leading to the age-metallicity degeneracy (Worthey, 1994). Measurements of spectral lines such as the Balmer series (which are sensitive to stellar age) and metal lines (which are sensitive to metallicity) can be used to help break the

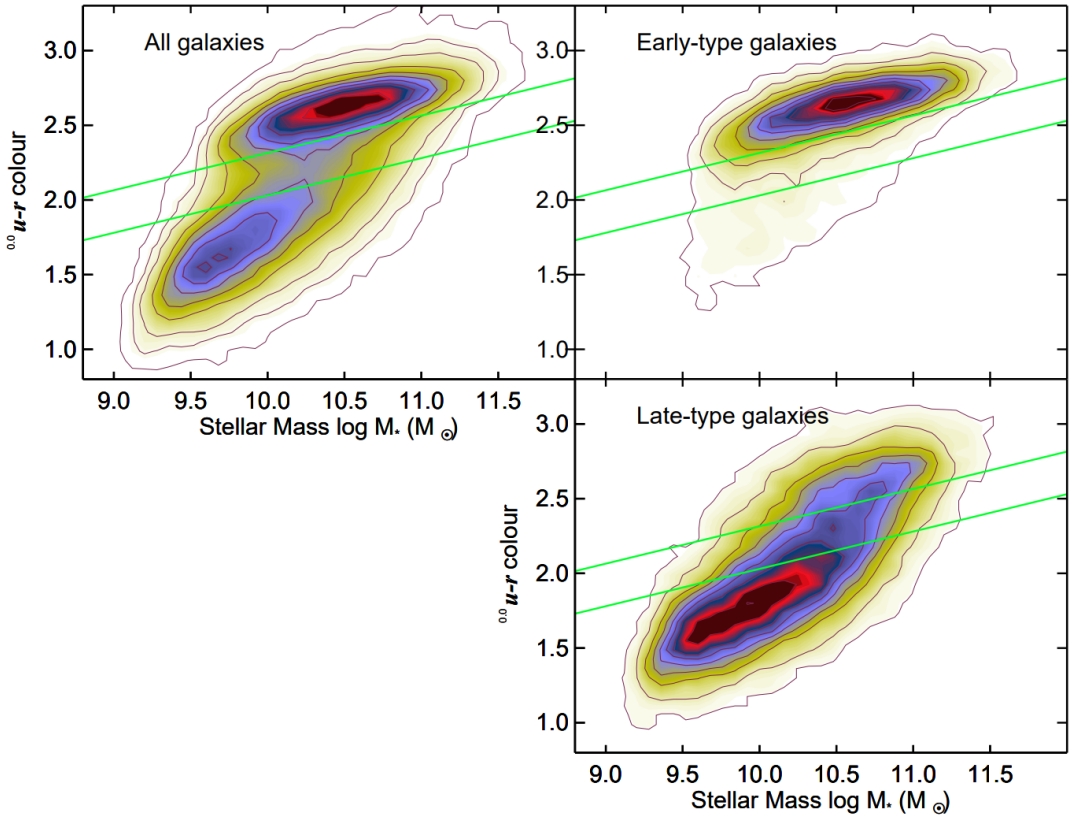

Figure 1.2: The *u-r* colour-mass diagram, taken from Schawinski et al. (2014). Green diagonal lines represent the 'green-valley'. The diagram clearly shows a bimodality in the distribution of galaxy colours: early-types (top-right) form a tight sequence, with high stellar masses and red colours, while late-type galaxies (bottom-right) are blue, and generally of lower stellar mass.

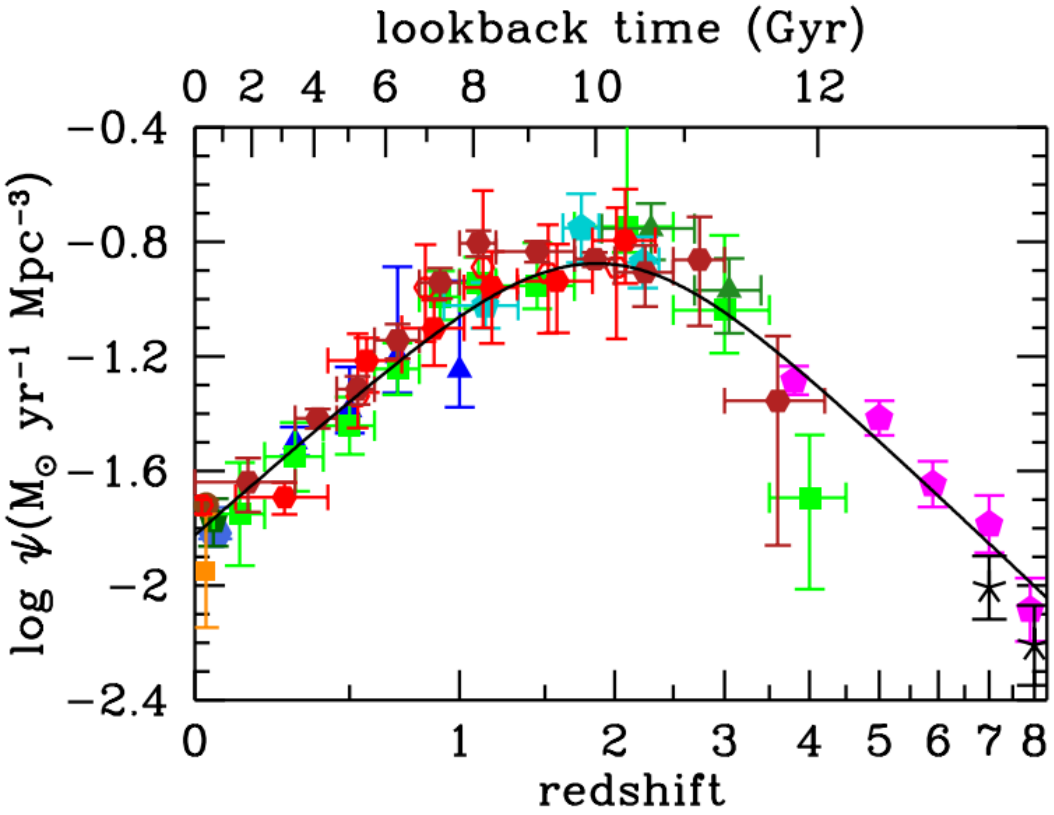

Figure 1.3: The history of cosmic star-formation, taken from Madau & Dickinson (2014). The black line shows the best-fitting star-formation rate density, based on FUV and IR luminosity measurements. Galaxies had a peak SFR roughly 10 billion years ago, and the rate of star-formtion has been declining since.

degeneracy.

1.1.3 Star-formation Rate

The star-formation rate (SFR) of a galaxy can be determined using various diagnostics sensitive to the presence of young stars (see Kennicutt & Evans, 2012; Madau & Dickinson, 2014). The most commonly used estimators are the UV and IR continuum luminosities, since these are dominated by OB star radiation (and emission from heated dust grains absorbing this radiation). X-ray and radio luminosities can also be used, as well as Hα and [O II] luminosities when spectral data is available. The star formation rate density (SFRD) of the Universe is the SFR per unit volume at a given epoch, and has

been studied out to $z \sim 8$. The SFRD was at its maximum at $z \sim 2$, with stars forming at a peak rate approximately 9 times higher than today (Madau & Dickinson, 2014, see Figure 1.3). This period is commonly referred to as 'cosmic noon'.

There is a tight relationship seen between SFR and the stellar mass (M_*) of star-forming galaxies, known as the star-forming main sequence (Brinchmann et al., 2004; Wuyts et al., 2011). The correlation has been studied out to $z \sim 6$ (Popesso et al., 2022), and is thought to have been in place since at least $z \sim 2$ (Daddi et al., 2007; Noeske et al., 2007). Starburst galaxies commonly lie above the main sequence, whilst quiescent galaxies lie below.

1.1.4 Spectral Properties of Galaxies

The stellar and gas content of galaxies can also be determined using spectral energy distributions (SEDs) and spectroscopy. With respect to continuum emission, young OB stars emit strongly in the UV and blue-optical, older stars and dust contribute to the IR and red-optical, and hot gas within the ISM emits in the X-ray range. If a galaxy contains an active galactic nuclei (AGN), this can have a large effect on the overall SED, as AGN emit strongly in the UV, optical, X-ray and (sometimes) radio wavelengths. Thus, the shape of an SED can give insight into the contents of a galaxy.

Absorption and emission lines present in galaxy spectra can also provide clues. The absorption line strengths of different stars vary due to differences in temperature; hotter stars have fewer absorption lines, while cooler stellar photospheres allow molecules which produce absorption features to form. Spectra may also show a discontinuity in the continuum flux at 4000Å, caused by the blanket absorption of radiation by metals in the stellar atmospheres of older stars, representing a deficiency of hot, young stars. Additionally, the flux ratio of the continuum either side of 4000Å, the D4000 index, can be used as an indication of the age of the stellar population within a galaxy (Poggianti & Barbaro, 1997). The spectra of galaxies hosting AGN may show forbidden emission lines, such as [O III], produced only in regions of very low-density gas, as well as strong, broad emission lines caused by the bulk, high-velocity motion of gas near the nucleus. Some absorption lines, such as Mg II and Na D, are good tracers of cool gas within the ISM (Veilleux et al., 2020), and the shape of their absorption features has been used to trace outflowing winds in some galaxies (see Section 1.3.1.1).

In general, quiescent galaxies have stronger absorption features, and few to no emission lines, and a strong 4000Å break.

1.2 Galaxy Environments

Galaxies have been found to reside in different environments. The currently accepted model for the formation of the Universe is the ΛCDM cosmological model (e.g. Deruelle & Uzan, 2018), in which the Universe is thought to be 13.7 billion years old, with a composition of baryons (~ 4.9%), dark matter (~ 26.8%) and dark energy (~ 68.3%). The process of structure formation within ΛCDM is hierarchical, where small density fluctuations in the very early Universe grow and collapse under gravity to form dark matter haloes. These haloes then merge, forming larger haloes which provide the potential wells for baryons to fall into. The baryonic matter compresses under gravity, eventually forming the stars and galaxies we see today (see, e.g. Silk, 1977; White & Rees, 1978; Peebles, 1982; White & Frenk, 1991). Galaxies are expected to form first within the highest density peaks in the underlying dark matter distribution. This is known as 'biased' galaxy formation, which leads to galaxies being typically more strongly clustered than the underlying dark matter (Coil, 2013). Hierarchical structure formation results in a non-uniform distribution of galaxies throughout the Universe; galaxies are commonly found in huge gravitationally bound groups and clusters. Groups often contain tens of galaxies with low relative velocities (~ 200 kms^{-1}), while galaxy clusters can contain thousands of galaxies moving at very high speeds (~ 800 - 1000 kms^{-1}, see, e.g. Hubble & Humason, 1931; Abell, 1965; Kravtsov & Borgani, 2012).

Galaxy environments can be measured using a variety of methods (see Muldrew et al., 2012, for a summary). Nearest neighbour techniques use the distance from the galaxy of interest to its *n*th-nearest neighbour, defining denser environments as those with smaller distances between galaxies (e.g. Brough et al., 2011). Alternatively, aperture densities can be found using a fixed volume around a given galaxy, within which the number of galaxies are counted (e.g. Croton et al., 2005; Lani et al., 2013). A higher number of galaxies indicates a higher-density environment. Finally, 'friends-of-friends' algorithms (Huchra & Geller, 1982; Socolovsky et al., 2018) find overdensities based on a fixed linking distance. If objects lie within the linking distance of the galaxy of interest, they are considered members of the same structure/dark matter halo.

Many studies have linked the internal properties of a galaxy to its environment:

1. *The morphology-density relation*. There is an observed increase in the fraction of elliptical and lenticular galaxies in increasingly dense environments at $z \sim 0$ (Oemler, 1974; Dressler, 1980). At higher redshifts ($z \sim 0.5$), the fraction of ellipticals in dense environments remains similar to the local universe, however the fraction of S0 galaxies is found to decrease. The deficit in lenticulars is matched by an increase in the fraction of spiral galaxies, indicating that high-z spirals are likely the progenitors of S0s in present day clusters (Dressler et al., 1997; Poggianti et al., 2006). It is therefore natural to assume that clusters and high-density environments may play a role in transforming the morphology of spiral galaxies. Mei et al. (2023) studied the local environment of cluster galaxies at $z \sim 2$, finding that the morphology-density relation may have already been in place by this epoch.

2. *The colour-environment relation*. Galaxies in high-density environments exhibit redder colours than their field counterparts (Kodama et al., 2001; Baldry et al., 2006; Bhambhani et al., 2023), and some studies observe this relationship out to $z \sim 1.4$ (e.g. Lemaux et al., 2019). However, other studies find that the relation is undetectable past $z = 1$ (Cucciati et al., 2006), or depends strongly on stellar mass (Grützbauch et al., 2011).

3. *The SFR-environment relation*. The SFR of galaxies in higher-density environments has been found to be lower than their field counterparts (Balogh et al., 1997; Gómez et al., 2003; Vulcani et al., 2010, see Figure 1.4), and this trend has been seen out to $z < 2$ (Noirot et al., 2018). In some $z > 1$ clusters, however, there is an observed reversal of the SFR-environment relation seen at lower redshift. Some clusters have been found to have enhanced SFRs in their cores (Tran et al., 2010; Santos et al., 2015; Wang et al., 2016). A strong dependence of the SFR-density relation on stellar mass has been noted by some authors (e.g. Lin et al., 2014; Tomczak et al., 2019).

4. *The size-environment relation*. Studies have also found evidence of a correlation between galaxy sizes and their environments, for low-mass galaxies. Maltby et al. (2010) found the sizes of only low-mass SFGs showed an environmental dependence; the environment had no effect on the sizes of high-mass SFGs or

quiescent galaxies (see also Huertas-Company et al., 2013; Yoon et al., 2023). In general, at $z > 0.5$, massive quiescent galaxies in high-density environments have larger radii than comparable field galaxies (Papovich et al., 2012; Cooper et al., 2012; Delaye et al., 2014). Kuchner et al. (2017) also found SFGs in clusters to be smaller than those in the field.

1.3 Galaxy Quenching

There is still a gap in our understanding, however, as to what leads to the cessation of star formation in star-forming galaxies, causing their evolution onto the red sequence. This process is commonly referred to as quenching, and comprises many possible physical mechanisms (discussed below) that could theoretically lead to a gas-rich galaxy experiencing a drop in star formation.

One way to investigate quenching is to study the evolution of the galaxy stellar mass functions (SMFs) that define the number density of galaxies of different masses. SMFs allow us to trace the assembly of stellar mass through cosmic time, and thus they provide a useful tool for studying quenching by quantifying the transformation of star-forming galaxies into quiescent[1] systems (e.g. Bell et al., 2003; Baldry et al., 2008; Pozzetti et al., 2010; Moustakas et al., 2013). Star formation in massive galaxies was at its peak from $z \sim 3$ to $z \sim 1$, a period often referred to as "cosmic noon", and over this relatively short time, these systems formed roughly half their current stellar mass (see Schreiber & Wuyts, 2020). Furthermore, there is strong evidence that most massive quiescent galaxies were already in place by $z \sim 1$ (e.g. Ilbert et al., 2013; Muzzin et al., 2013; Papovich et al., 2018; Wright et al., 2018; Leja et al., 2020; McLeod et al., 2021; Santini et al., 2022; Weaver et al., 2023). Ilbert et al. (2013) found that the number density of quiescent galaxies increases from $z \sim 3$ to $z \sim 1$ over all stellar masses, with no significant evolution at the high-mass end below $z \sim 1$. Similarly, McLeod et al. (2021) found that while passive galaxies contributed < 10 per cent to the total stellar mass density of the Universe at $z \sim 3$, they dominate by $z \sim 0.75$.

[1]Throughout this thesis, I use the terms 'quiescent' and 'passive' interchangeably, to refer to red and dead systems which are no longer forming stars.

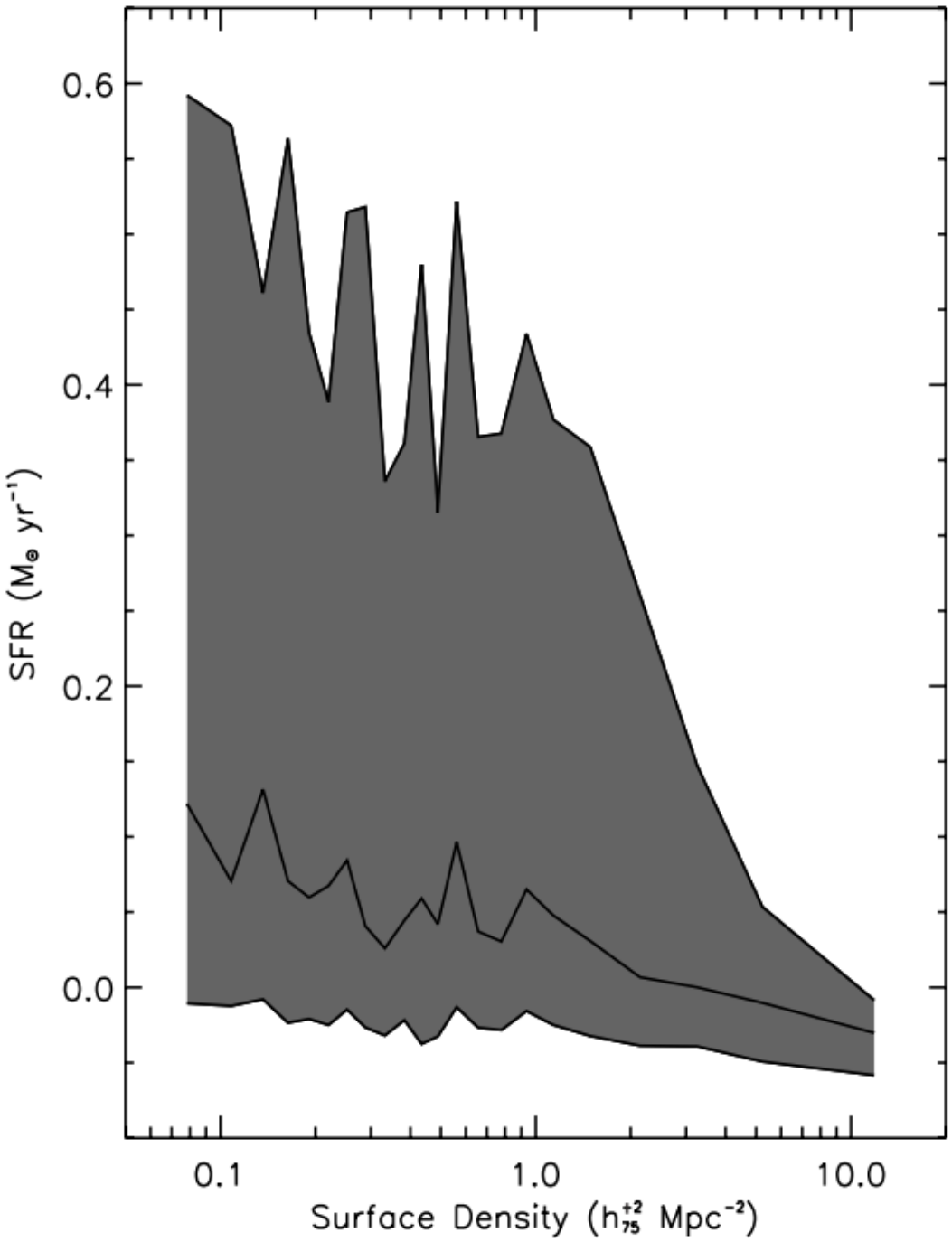

Figure 1.4: The SFR-environment relation, taken from Gómez et al. (2003). The shaded area represents the distribution of SFRs, between the 25th and 75th percentiles. The central solid line shows the median SFR. There is a clear decline in the SFR of galaxies residing in denser environments.

1.3.1 Quenching Mechanisms

Different quenching mechanisms are expected to act on different timescales, leading to varying spectral features and morphological properties in the quenched systems. The proposed mechanisms can be broadly separated into two classes: (i) internal processes and (ii) external processes related to the galaxy's environment.

1.3.1.1 Internal Mechanisms

Internal, or secular, quenching mechanisms can occur in all galaxies, regardless of their environment. A selection of these processes are described below.

Supernovae feedback. High-mass stars ($M_* \sim 8$ - $25\ M_\odot$) at the end of their life release large amounts of energy into the ISM via Type II supernovae (see, e.g. Heckman & Thompson, 2017; Rupke, 2018; Veilleux et al., 2020). This energy injection drives outflowing galactic winds, which can clear dense gas from star-forming regions (Sokal et al., 2016), and/or heat the cool gas within a galaxy via shocks, preventing further star formation (Alatalo et al., 2016). Supernovae feedback is expected to be more effective in low-mass galaxies, which have a weaker gravitational hold on their gas (Larson, 1974; Dekel & Silk, 1986). Simulations also indicate this mechanism is effective at suppressing star formation rates (Springel & Hernquist, 2003), and could remove up to $\sim$ 60 per cent of gas in the lowest-mass galaxies (Efstathiou, 2000). Outflows driven by supernovae are a common feature of galaxies with high star-formation rates out to redshifts of $z \sim$ 2-3 (e.g. Murray et al., 2011; Bradshaw et al., 2013; Borthakur et al., 2013; Geach et al., 2014; Rupke, 2018).

AGN feedback. Supermassive black holes (SMBHs) at the centre of galaxies emit significant amounts of energy via the accretion of surrounding material – the accreted material loses gravitational potential energy which is converted into heat and radiated away. AGN feedback is a key ingredient in cosmological simulations of galaxy evolution (Hopkins et al., 2006; Debuhr et al., 2012; Schaye et al., 2015; Sijacki et al., 2015), where it is invoked to prevent the build-up of too many massive galaxies. There are two main modes of AGN feedback commonly invoked to explain quenching: radiative mode and radio mode (see, e.g. Silk & Rees, 1998; Fabian, 2012; Combes, 2017; Morganti, 2017; Harrison & Ramos Almeida, 2024).

1. *Radiative mode*, or quasar mode, AGN feedback occurs when a highly luminous SMBH is accreting matter at close to the Eddington limit. Once the accretion limit is reached, the SMBH radiation begins to drive huge outflows which eject surrounding material. This process can potentially shut down future star formation, as the radiation can couple with cold gas and clear it from the galaxy (e.g. Fabian, 1999; Benson et al., 2003).

2. *Radio mode*, or maintenance mode, feedback occurs in galaxies with a BH accreting at lower rates which produce powerful radio jets. These jets heat gas within the circumgalactic medium (CGM), preventing the galaxy from accreting further cool gas for star formation (e.g. McNamara & Nulsen, 2007; Bower et al., 2012). Radio mode AGN are typically associated with massive galaxies in the centres of groups and clusters (McNamara et al., 2005; Voit et al., 2015).

In general, AGN feedback is thought to have more impact on high-mass galaxies, since galaxy mass is correlated with black hole mass (Silk & Rees, 1998; Best et al., 2005). Observations of outflows in galaxies hosting AGN at both low (Rupke & Veilleux, 2011; Sturm et al., 2011) and high redshift (Alexander et al., 2010; Maiolino et al., 2012) provide evidence for the feedback processes taking place.

High-velocity outflows are ubiquitous in star-forming galaxies at cosmic noon, both with (Feruglio et al., 2010; Hainline et al., 2011; Harrison et al., 2012; Cicone et al., 2014) and without AGN (Bradshaw et al., 2013; Geach et al., 2014; Talia et al., 2017), but are not detected in old quiescent galaxies at the same epoch (e.g. Maltby et al., 2019). Recent work has found evidence that outflow velocity depends on various properties, such as SFR and SFR density (e.g. Heckman et al., 2015; Heckman & Borthakur, 2016), and (more weakly) on stellar mass (Davis et al., 2023), suggesting that star-formation may be the root of galactic-scale winds. Some studies conclude that, although AGN activity can boost outflow velocity compared to outflows driven solely by star-formation (Cicone et al., 2014), even AGN driven winds may not be sufficient to fully clear cold gas from a galaxy (e.g., Fluetsch et al., 2019).

In addition to driving outflows, AGN may also influence star formation in more subtle ways, e.g. by injecting turbulence in the ISM, effectively smoothing it on small scales and preventing collapse to very high densities (e.g., Guillard et al., 2015; Smercina et al., 2018, 2022). Very strong molecular lines suggest turbulent/shock heating, but the lack

of other molecular species suggest gas isn't collapsing to form dense molecular clouds.

Morphological quenching. The velocity of stars and gas within a galactic bulge increases proportional to bulge mass (Kormendy & Illingworth, 1982). Any bulge growth leads to an increase in gas velocity, and consequently, temperature, preventing star formation (Martig et al., 2013; Gensior et al., 2020). The basic idea of morphological quenching is that a galaxy can quench internally without the removal of cold gas (Martig et al., 2009), and may help explain observations of local quiescent galaxies containing significant atomic or molecular gas reservoirs (Young et al., 2009; Donovan et al., 2009). The initial bulge growth may be triggered by external mechanisms such as mergers, however, which are discussed below.

1.3.1.2 External Mechanisms: galaxy-galaxy interactions

The hierarchical growth of structure in the Universe results in large, central galaxies being surrounded by smaller satellite galaxies. Interactions between close neighbours can cause disruptions to the baryonic matter within a galaxy.

Mergers. If two systems are moving with low relative velocities, they may collide and undergo a merger, combining their stellar and gaseous material (Icke, 1985; Bekki, 1998). Mergers are thought to be most efficient in lower-density environments such as galaxy groups, since galaxy velocities in clusters are too high to allow direct collisions (Ostriker, 1980; van Dokkum et al., 1999; Ellison et al., 2010; Kampczyk et al., 2013; Delahaye et al., 2017; Sureshkumar et al., 2024). Mergers can be categorised based on the masses of the galaxies colliding (major or minor mergers), or their gas content (wet or dry mergers).

1. *Major mergers* involve galaxies with mass ratios of 1:4 or greater (Conselice, 2014), and can lead to structural changes within the stellar distribution of the resulting system (Toomre & Toomre, 1972). During a major merger, gas can flow inwards into the galaxy centre, triggering extreme starbursts (Ellison et al., 2013; Baron et al., 2020; Lotz et al., 2021), AGN activity (Springel et al., 2005; Goulding et al., 2018; Gao et al., 2020) and shocks (Cox et al., 2004; Alatalo et al., 2016). Feedback from star formation and AGN may then result in outflows (see Section 1.3.1.1), clearing star-forming fuel from the galaxy, whilst shocks may

heat cool gas preventing further star formation.

2. *Minor mergers* involve galaxies with lower mass ratios (Conselice, 2014). These events are less violent than major mergers, but are expected to be more frequent (Jogee et al., 2009; Conselice et al., 2022) and may still trigger radial inflows and starbursts (Mihos & Hernquist, 1994; Lambas et al., 2012; Jackson et al., 2019).

3. *Wet mergers* of gas-rich galaxies can trigger large amounts of star-formation as gas is driven inwards (Barton et al., 2000; Bridge et al., 2007; Lin et al., 2008), and induce AGN activity (Hopkins et al., 2006).

4. *Dry mergers* of gas-poor galaxies result in little increase to star formation rates, but may lead to size growth of already quenched galaxies (van Dokkum, 2005; Bell et al., 2006). The energy of the merger cannot be dissipated by the gas and/or triggered star-formation, and hence causes an expansion of the stellar distribution.

Mergers are typically identified by selecting galaxies which show signs of disturbances in their stellar distributions such as asymmetry or tidal tails (Conselice et al., 2003; Lotz et al., 2011; Whitney et al., 2021), or by selecting close galaxy pairs (Bluck et al., 2012; Mundy et al., 2017). Merger rates have been shown to decrease with cosmic time (Casteels et al., 2014; Duncan et al., 2019; Whitney et al., 2021).

Harassment. Galaxies within high-density environments such as cluster cores have high relative velocities, and often undergo high-speed 'fly-bys' (Moore et al., 1996; Smith et al., 2010; Bialas et al., 2015). The cumulative effect of several high-speed interactions is known as harassment, and can result in tidal tails and asymmetry in galaxy stellar distributions, with much of the stellar material stripped (Moore et al., 1999). Harassment is thought to be more effective at stripping low-mass galaxies, due to the weaker gravitational hold on gas and stars within the galaxy.

1.3.1.3 External Mechanisms: galaxy-cluster interactions

There exists a hot, X-ray emitting gas between galaxies in a cluster, known as the intracluster medium (ICM), the density of which rises towards the cluster centre. As a galaxy moves through a high-density environment, the hot ICM exerts pressure on the galaxy ISM, causing the gas in a galaxy to be stripped.

Ram pressure stripping. If ICM pressure is strong enough to overcome the gravitational potential of the galaxy, it can remove the gas contained within the ISM via ram-pressure stripping (RPS, Gunn & Gott, 1972). RPS affects the gas and dust within a galaxy, but is unable to alter the stellar distribution directly (Boselli et al., 2022). Simulations have found that ram pressure could strip up to 50 per cent of a galaxy's cool gas (Bahé & McCarthy, 2015). RPS is expected to reach peak intensity in cluster cores, as ICM density decreases radially – outside a given cluster-centric radius, the ICM ram pressure may not be sufficient to overcome the gravitational potential of a galaxy (Cortese et al., 2021; Boselli et al., 2022). At low redshift, RPS is thought to be the most common process stripping gas from satellite galaxies (e.g., Marasco et al., 2016), but may be less prominent in early clusters where the ICM is not yet dense enough to supply sufficient pressure (Balogh et al., 2016; Hwang et al., 2018). Wetzel et al. (2015) found increasing quenching timescales with increasing stellar mass, consistent with the idea that RPS efficiency is lower for higher-mass galaxies due to the stronger gravitational hold on their gas.

Strangulation/starvation. Galaxies infalling into clusters experience tidal forces which can remove the hot gas in their CGM, cutting off the replenishment of fuel for star formation ('*strangulation*', Cole et al., 2000; Balogh & Morris, 2000) and/or preventing accretion of further cold gas ('*starvation*', Larson et al., 1980). Feedback from star formation and AGN activity may expel gas into the CGM, which is then removed, accelerating strangulation. Starvation and strangulation are thought to be more dominant than RPS in cluster outskirts and young clusters, where the ICM is not sufficiently dense to strip a galaxy's ISM fully, but may remove the less gravitationally bound hot gas from the CGM (Cortese et al., 2021).

1.3.1.4 Mass or Environment?

Quenching mechanisms are often broadly grouped into 'mass quenching' and 'environmental quenching' (e.g Peng et al., 2010; Muzzin et al., 2012; Papovich et al., 2018). Mass quenching involves mechanisms driven by stellar mass or internal galaxy properties (Section 1.3.1.1), whereas environmental quenching mechanisms are those driven by a galaxy's environment or external processes (Sections 1.3.1.2 and 1.3.1.3). Peng et al. (2010) found that the effects of mass and environment on quenching were completely separable out to $z \sim 1$, and were able to reproduce the evolution of the SMFs of blue

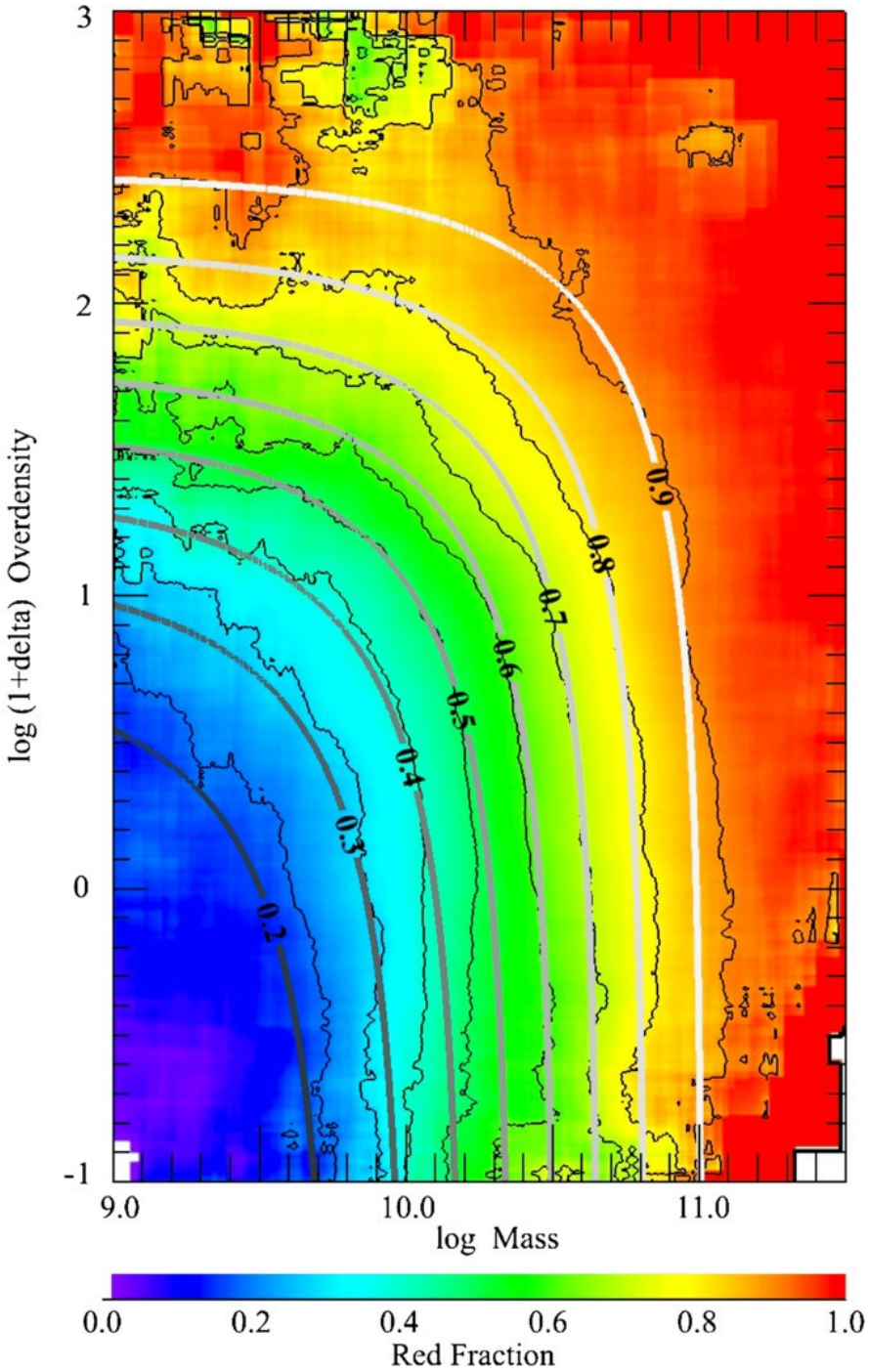

Figure 1.5: The red fraction as a function of galaxy stellar mass and environment at $z <$ 1, taken from Peng et al. (2010). In this study, the effects of mass and environment on galaxy quenching were found to be independent. The fraction of red galaxies increases with overdensity at fixed stellar mass, and increases with stellar mass at fixed overdensity.

and red galaxy populations with this quenching formalism (see Figure 1.5). They found that the efficiency of mass quenching is proportional to the star formation rate (SFR), and that the efficiency of environment quenching depends on the galaxy density field, with galaxies in the highest density environments having a higher likelihood of being quenched (see also Kovac et al., 2014; Knobel et al., 2015). In contrast, some studies of groups and clusters find that the same formalism used by Peng et al. may not hold past $z \sim 0.7$ (e.g., Balogh et al., 2016; McNab et al., 2021). Studies at higher redshifts suggest either a declining influence from environmental quenching (e.g., Nantais et al., 2016; Kawinwanichakij et al., 2017; González Delgado et al., 2022) or potentially no additional quenching due to environment (Darvish et al., 2016). Furthermore, De Lucia et al. (2012) propose that in the real Universe it is unexpected that mass and environment separability holds at any redshift, as the two are physically connected (see also Pintos-Castro et al., 2019). **Observationally, however, the role played by environment in quenching galaxies remains unclear at $z > 1$.**

1.4 Post-starburst Galaxies

Studying galaxies in transitionary stages may provide the key to understanding the processes responsible for terminating star formation. One such class are post-starburst galaxies (PSBs, e.g., Dressler & Gunn, 1983; Tran et al., 2004; Wild et al., 2009; French, 2021), which are thought to be systems that have undergone a recent, major burst of star formation (or an extended period of high star formation) followed by rapid quenching.

PSBs are typically identified by their spectra showing both strong Balmer absorption lines typical of a population dominated by young A/F stars, and weak or absent nebular emission lines, indicating the lack of ongoing star-formation. One traditional PSB selection method uses cuts on the Hδ absorption and [OII] emission lines, due to their close proximity in spectra (e.g., Zabludoff et al., 1996; Goto, 2005; French et al., 2015, see Figure 1.6). However, the requirement for low or absent emission lines can bias sample selections against active galactic nuclei (AGN) and galaxies exhibiting shocks. Shocks may be expected in galaxies which have undergone a recent merger (Rich et al., 2011; Soto et al., 2012; Mortazavi & Lotz, 2019), and thus selecting against these objects may exclude a sample of young, more recently quenched galaxies. Recently, Alatalo et al. (2016) selected sample of 'shocked post-starbursts', or SPOGs, by allowing for emission

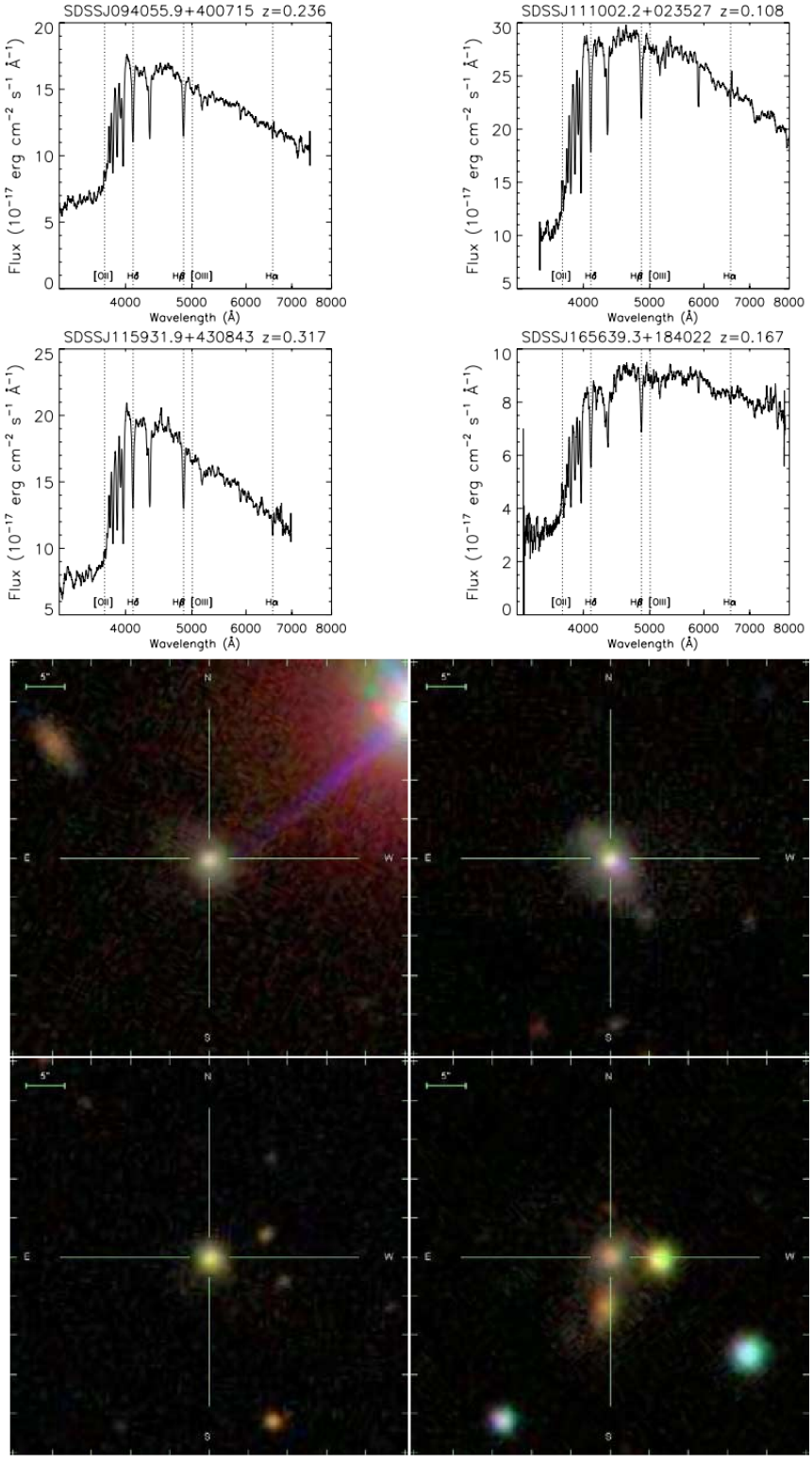

Figure 1.6: Example PSB spectra (*top*) and the corresponding imaging (*bottom*), taken from Goto (2007). These objects show the typical triangular shape of PSB spectra, and have a commonly observed red, compact appearance.

line ratios consistent with shocks, and found their sample to be at an earlier stage of transition than those selected to have no emission. Photometry can also be used to select PSBs, as they populate a unique position in UVJ diagrams (Whitaker et al., 2012; Suess et al., 2020), and their SEDs have a distinct triangular shape (when displayed in F_λ, see Figure 1.6), due to the dominance of A/F-type stars. To allow for PSB samples including AGN, Wild et al. (2007, 2009) performed a principal component analysis (PCA) over the 4000Å region of galaxy spectra, finding two principal components correlated with the Lick $H\delta_A$ (Worthey & Ottaviani, 1997) and D_n4000 (Bruzual A., 1983) indices. The D_n4000 index can select against ongoing star formation while allowing for some AGN activity. In subsequent work, Wild et al. (2014, 2016) applied a similar PCA method to galaxy SEDs, finding a well distinguished PSB population without the need for extensive and expensive spectroscopy.

PSBs constitute only a small fraction of the total galaxy population. Wild et al. (2016) found that they are rare at all epochs: less than 1% of local massive galaxies are PSBs, with this number rising to $\sim 5\%$ at $z \sim 2$. Studies have found that PSBs could potentially evolve to produce up to $\sim 50\%$ of the massive red sequence, depending on the assumptions made about their visibility timescales and star formation histories (e.g Wild et al., 2016; Belli et al., 2019; Wild et al., 2020).

1.4.1 How do Post-starburst Galaxies Become Quenched?

As discussed previously, there are a whole host of different quenching mechanisms which have varying effectiveness depending on a galaxy's internal properties, environment and redshift. Therefore, it is natural to expect PSBs to be produced by distinct routes with different combinations of quenching mechanisms (e.g., Pawlik et al., 2019).

Various authors have found that PSBs are more abundant in denser environments to $z \sim 1$, suggesting a strong link to environmental quenching (e.g Poggianti et al., 2009; Vergani et al., 2010; Muzzin et al., 2012; Socolovsky et al., 2018; Paccagnella et al., 2019). Poggianti et al. (2009) find that PSBs at $0.4 < z < 0.8$ reside preferentially in high-density environments, with a higher prevalence of PSBs in clusters with higher velocity dispersions, indicating quenching in their sample is due to ICM related processes. Studies of PSBs in clusters at both $z \leq 0.1$ (Paccagnella et al., 2017; Owers et al., 2019) and $z \sim 1$ (Muzzin et al., 2014) detect a higher incidence of PSBs closer to the cluster

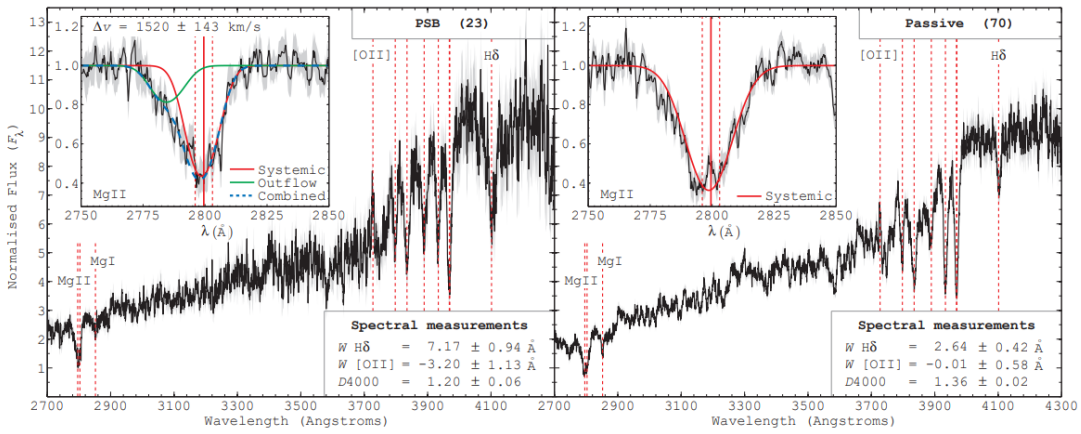

Figure 1.7: Stacked optical spectra of $1 < z < 1.4$ PSBs (*left*) and passive galaxies (*right*), taken from Maltby et al. (2019). The inset in each panel shows the Mg II absorption feature for the stack, with a best-fitting two component Gaussian model (blue dashed line). The model is comprised of a rest-frame ISM component (red), and a component to model any outflowing gas (green). The post-starburst galaxy stack shows clear asymmetry in the Mg II profile, indicating outflowing gas with velocity ~ 1000 kms^{-1} as determined from the fit. The passive galaxies show no evidence of outflows.

core, and suggest ram-pressure stripping is the most plausible candidate for the cause of quenching (however, see von der Linden et al., 2010). Werle et al. (2022) use spatially resolved spectroscopy of 21 cluster PSBs at $0.3 < z < 0.4$, and find the majority of their sample show evidence for 'outside-in' quenching, attributing this to RPS. The authors also observe three galaxies at the high-mass end of their sample with signs of 'outside-in' quenching, two of which host an AGN, implying internal processes are the more probable cause. Socolovsky et al. (2018) study the stellar mass functions of galaxies in different environments at $0.5 < z < 1$, finding a strong excess of low-mass PSBs in clusters, and a corresponding deficit of low-mass star-forming galaxies. They determine that 74 per cent of their $M_* < 10^{10.5}$ $M_\odot$ cluster galaxies were rapidly quenched, while the remaining objects were quenched via a slower pathway.

With the exception of the work contained within this thesis, to date, there have been no studies of the link between PSBs and environment at higher redshifts ($z > 1.5$), when massive ($M_* > 10^{10}$ $M_\odot$) PSBs were much more common (Wild et al., 2016). Studies of this nature could provide insight into the mechanisms responsible for quenching massive galaxies at this crucial epoch.

Feedback from both AGN and star formation has also been inferred in many PSBs

through the presence of outflows. Locally, Alatalo et al. (2011) detect a $\sim$ 400 kms^{-1} outflow in the PSB NGC 1266, and determine that star formation alone is insufficient to drive the outflow and AGN feedback is needed. Outflows have been detected in z $\sim$ 0.1 PSBs hosting AGN by Baron et al. (2017, 2018, 2020), along with disturbed gas providing evidence for minor mergers. At $z \sim 0.6$, $\sim$ 1000 kms^{-1} outflows have been observed, with debate over whether the winds originate from highly compact starbursts (Coil et al., 2011; Diamond-Stanic et al., 2012; Sell et al., 2014; Perrotta et al., 2021) or from AGN feedback (Tremonti et al., 2007). PSBs have been found to be highly compact, both at low (e.g., Luo et al., 2022; Otter et al., 2022) and high redshift (e.g., Almaini et al., 2017; Maltby et al., 2018), suggesting that compact central starbursts could be a common feature in this population.

At higher redshift, studies have found similar results. Maltby et al. (2019) find similarly high-velocity outflows (v_{out} $\sim$ 1150 kms^{-1}) in a sample of 40 PSBs at $z > 1$ which show no AGN signatures in their optical data (Figure 1.7). They conclude that these PSBs were either quenched solely by stellar feedback from an intense episode of star-formation, or that any AGN episode which may have contributed to the winds has now faded. Conversely, Man et al. (2021) detect $\sim$ 1500 kms^{-1} outflows in two gravitationally lensed recently-quenched galaxies at $z \sim 3$ with emission line ratios that could indicate AGN activity (see also: Belli et al., 2023). Similarly, Davies et al. (2024) find 14 galaxies in their sample ($1.7 < z < 3.5$) with neutral gas outflows they attribute to AGN feedback. Recently, some work has been done to investigate how outflows evolve alongside their host galaxy in the local Universe; Sun et al. (2024) find outflow velocities decreasing with time since a starburst in a sample of 80,000 galaxies using SDSS.

There is also evidence for different quenching routes being dominant for during different epochs in general (e.g., Carnall et al., 2019; Tacchella et al., 2022; Hamadouche et al., 2023), and for PSBs specifically. By analysing the structure of PSBs at $0.5 < z < 2$, Maltby et al. (2018) find significant differences at different redshifts. At $z > 1$, PSBs in their sample are highly compact with structures similar to massive quiescent galaxies, whilst PSBs at $z < 1$ are generally lower-mass and similar to passive discs. The authors suggest two distinct quenching routes, where high-mass ($M_* > 10^{10.5}$ $M_\odot$), high redshift PSBs experience a major disruptive event (such as a gas-rich major merger) that leads to compaction (see also, Almaini et al., 2017), whereas low-mass, low redshift PSBs undergo a gentler, less disruptive quenching process. Belli et al. (2019) model the number density evolution of quiescent galaxies and find evidence for a fast quenching

route which produces compact PSBs – likely gas-rich major mergers –, and a slow quenching route that affects primarily larger galaxies. Wilkinson et al. (2021) study the clustering of PSBs from $0.5 < z < 3$, finding low-mass PSBs at $z < 1$ reside preferentially in high-mass haloes, while high-mass PSBs are more weakly clustered at this epoch. The authors combine this with structural properties of PSBs to conclude that secular quenching is dominant at $z > 1$ and environmental quenching is dominant at lower redshifts. Combined, the structural studies, mass functions, and large-scale structure, all point to two rapid quenching routes: one at high-mass and high redshift, and the other at low-mass and low redshift.

1.5 Structure of this Thesis

In this thesis, we explore the roles that galaxy environment, stellar mass and outflows play in the quenching of star formation, by studying recently quenched galaxies – those which have had their star-formation quenched within the last 1Gyr, such as PSBs – at cosmic noon and beyond ($0.5 < z < 4.4$). The structure of this thesis is as follows. In Chapter 2, we determine the influence of stellar mass and environment on the build up of the quiescent population since $z = 3$, by investigating galaxy stellar mass functions split by environment. We use this analysis to calculate the probability of quenching for a galaxy of a given mass, in a given environment. In Chapter 3, we employ a stacking analysis of VLT optical spectra of high redshift ($z \geq 1$) PSBs and recently quenched galaxies, along with highly star-forming and passive galaxies. This allows us to determine how outflow velocity varies with time since a starburst, and whether AGN play a key role in quenching at cosmic noon. We build on this work in Chapter 4, by analysing the JWST NIRSpec data of 9 (7) PSBs at redshifts $z > 1.8$ (3). We utilise these high resolution spectra to establish, for the first time, if outflows are prevalent in post-starburst galaxies at earlier epochs than cosmic noon. JWST allows us to explore outflows in individual galaxies, which is very challenging to do with ground-based spectra. Finally, in Chapter 5, we present the conclusions and discuss the potential future work to be undertaken.

Throughout this thesis, we adopt the AB magnitude system and a flat ΛCDM cosmology with $\Omega_M = 0.3$, $\Omega_\Lambda = 0.7$, and $H_0 = 100\,h$ kms^{-1} Mpc^{-1} where $h = 0.7$.

Chapter 2

Mass and Environment: Effects on Quenching Since Cosmic Noon

The work presented in this chapter has been published in Taylor et al. (2023). In this chapter, all statistical analyses are my own work, however measurements of stellar mass, redshifts and any relevant galaxy classifications are drawn from the principal component analysis published in Wilkinson et al. (2021). Environment measurements used were undertaken by my collaborator and co-author, David Maltby.

2.1 Introduction

One way to investigate quenching is to study the evolution of the galaxy stellar mass functions (SMFs) that define the number density of galaxies of different masses. SMFs allow us to trace the assembly of stellar mass through cosmic time, and thus they provide a useful tool for studying quenching by quantifying the transformation of star-forming galaxies into quiescent systems (e.g. Bell et al., 2003; Baldry et al., 2008; Pozzetti et al., 2010; Moustakas et al., 2013). Star formation in massive galaxies was at its peak from $z \sim 3$ to $z \sim 1$, a period often referred to as "cosmic noon", and over this relatively short period of time these systems formed roughly half their current stellar mass (see Schreiber & Wuyts, 2020). Furthermore, there is strong evidence that most massive quiescent galaxies were already in place by $z \sim 1$ (e.g. Ilbert et al., 2013; Muzzin et al.,

2013; Wright et al., 2018; McLeod et al., 2021). Ilbert et al. (2013) found that the number density of quiescent galaxies increases from $z \sim 3$ to $z \sim 1$ over all stellar masses, with no significant evolution at the high mass end below $z \sim 1$. Similarly, McLeod et al. (2021) found that while passive galaxies contributed < 10 per cent to the total stellar mass density of the Universe at $z \sim 3$, they dominate by $z \sim 0.75$.

Quenching mechanisms are often broadly grouped into 'mass quenching' and 'environmental quenching' (e.g Peng et al., 2010; Muzzin et al., 2012; Papovich et al., 2018, see Section 1.3.1.4). Peng et al. (2010) found that the effects of mass and environment on quenching were completely separable out to $z \sim 1$. The authors state that the efficiency of mass quenching is proportional to the star formation rate (SFR), and that the efficiency of environment quenching depends on the galaxy density field (see Figure 1.5, Section 1.3.1.4). In contrast, some studies of groups and clusters find that the same formalism used by Peng et al. may not hold past $z \sim 0.7$ (e.g., Balogh et al., 2016; McNab et al., 2021). Studies at higher redshifts suggest either a declining influence, or no additional quenching, from the environment (e.g., Nantais et al., 2016; Darvish et al., 2016; Kawinwanichakij et al., 2017; González Delgado et al., 2022). Observationally, however, the role played by environment in quenching galaxies remains unclear at $z > 1$.

Studying galaxies in transitionary stages, such as post-starburst galaxies (PSBs, see Section 1.4), may provide the key to understanding the processes responsible for terminating star formation. PSBs are rare at all epochs: Wild et al. (2016) found that less than 1% of local massive galaxies are PSBs, with this number rising to $\sim 5\%$ at $z \sim 2$. PSBs could potentially evolve to produce up to $\sim 50\%$ of the massive red sequence, depending on the assumptions made about their visibility timescales and star formation histories (e.g Wild et al., 2016; Belli et al., 2019; Wild et al., 2020). To date there have been no studies of the link between PSBs and environment at higher redshifts ($z > 1.5$), where massive ($M_* > 10^{10}$ $M_\odot$) PSBs were much more common (Wild et al., 2016). Work of this nature could provide insight into the mechanisms responsible for quenching massive galaxies at this crucial epoch.

In this chapter, we investigate the influence of stellar mass and environment on the build up of the quiescent population since $z = 3$. We study the evolution of PSBs and the galaxy mass functions, but now (for the first time) separated by environment. We then calculate both the growth rate of the quiescent population and the quenching rate in separate redshift, mass and environment bins to analyse whether these factors are indeed

separable out to high redshift. The deep imaging from the Ultra-Deep Survey (UDS, Almaini et al., in prep) is ideal for this study, allowing us to probe typical galaxies ($\sim 10^{10}$ $M_{\odot}$) to $z \sim 3$, with sufficient volume to enable samples to be split by stellar mass, redshift and environment.

The structure of this chapter is as follows: In Section 2.2, we present our data, the galaxy classification method, and the environment measurements. In Section 2.3, we present our results on the quenching rates in different environments, before performing a series of robustness tests in Section 2.4. In Section 2.5, we explore the contribution of PSBs to the build-up of the passive galaxy population. We end with our conclusions and a brief summary in Section 2.6.

2.2 Data and Method

2.2.1 The UDS

The UDS is the deepest NIR survey conducted over ~ 0.8 deg^2, and the deepest component of the United Kingdom Infrared Telescope (UKIRT) Infrared Deep Sky Survey (UKIDSS; Lawrence et al., 2007). We use the UDS Data Release 11 (DR11) catalogue, which reaches a 5σ limiting depth of $J = 25.6$, $H = 25.1$, and $K = 25.3$ in 2-arcsec diameter apertures. Further details can be found in Almaini et al. (2017) and Wilkinson et al. (2021). Full details of the DR11 catalogue and photometric redshifts will be presented in Almaini et al. (in prep).

The UKIDSS imaging is complemented by deep photometric data in 9 other bands: *B*, *V*, *R*, *i'* and *z'*-band optical observations from the Subaru XMM-Newton Deep Survey (SXDS, Furusawa et al., 2008), *U'*-band photometry from the CFHT Megacam, mid-infrared photometry (3.6μm and 4.5μm) from the *Spitzer* UDS Legacy Program (SpUDS, PI:Dunlop) and deep *Y*-band data from the VISTA VIDEO survey (Jarvis et al., 2013). The area of the UDS covered by all 12 bands is 0.62 deg^2.

In the UDS, photometric redshifts were computed using the method outlined in Simpson et al. (2013), using the EAzY code (Brammer et al., 2008) to fit a linear combination of template SEDs to the photometry at each redshift grid point. The set-up broadly

follows the default EAzY configuration for the 12 Flexible Stellar Population Synthesis (FSPS) SED components (Conroy & Gunn, 2010), with the addition of three simple stellar population (SSP) templates. This combination gave the best results in terms of the scatter and outlier fraction when compared to the available spectroscopic redshifts. The three SSP models have ages of 20, 50 and 150 Myr, using a Chabrier IMF and sub-solar metallicity (0.2 solar), and represent recent bursts of star formation to complement the complex and continuous star-formation histories of the FSPS templates. It was found that varying the metallicities of these bursts was unimportant to the results. The UDS contains $\sim$ 8000 sources with secure spectroscopic redshifts, and comparison of the photometric redshifts yields a mean absolute dispersion in $(z_{phot} - z_{spec})/(1 + z)$ of $\sigma_{NMAD} = 0.019$ with an outlier fraction ($|\Delta z|/(1 + z) > 0.15$) of $\sim$ 3%. Further detail on the determination of photometric redshifts can be found in Simpson et al. (2013) and Hartley et al. (in prep.).

2.2.2 Galaxy Classification

To separate star-forming galaxies, passive galaxies, and PSBs, we use the principal component analysis (PCA) technique established by Wild et al. (2014, 2016) (with further spectroscopic confirmation by Maltby et al., 2016). In brief, the aim of the PCA method is to describe the broad range of galaxy SEDs using the linear combination of a small number of components. It is found that three components are needed to sufficiently account for the variance in SEDs, with the amplitude of each component being termed a 'supercolour' (SC). The first two supercolours, SC1 and SC2, are the most useful in determining whether a galaxy is a good PSB candidate. SC1 correlates with sSFR and mean stellar age, and SC2 correlates with the fraction of a galaxy's stellar mass formed within the last billion years. Galaxies can be classified based on their position in a SC1-SC2 diagram, where the population boundaries are determined by comparison to model SEDs and spectroscopy. PSBs are identified as galaxies with a low value of SC1 (low sSFR) and a high value of SC2 (> 10% stellar mass built up in the last Gyr). The "dusty" star-forming class identified by Wild et al. (2014) are combined with other star-forming galaxies for our analysis. For a more detailed explanation of the supercolour analysis, see Wild et al. (2014).

This technique was originally established using the UDS DR8 catalogue, but here we

use an updated SC analysis applied to the full DR11 catalogue, explained in more detail in Wilkinson et al. (2021). The main modification made for the DR11 catalogue is to extend the redshift range (adding in analysis for $2 < z < 3$), which required a slight modification to the rest-frame wavelength range analysed. The DR11 catalogue is also deeper, with more accurate photometric redshifts (see Section 2.2.1).

2.2.3 Galaxy properties

Stellar masses are calculated using a Bayesian analysis, following the method outlined in Wild et al. (2016). Tens of thousands of Bruzual & Charlot (2003) population synthesis models are constructed with a range of star-formation histories, and then fitted to our supercolours (see Section 2.2.2). The resulting internal errors in the stellar masses are typically ± 0.1 dex at fixed redshift, allowing for the degeneracy between fitted parameters (see Wild et al., 2016). Further discussion of systematic stellar mass uncertainties can be found within Almaini et al. (2017). The 90% stellar mass completeness limits are calculated using the method of Pozzetti et al. (2010) and are given for the different galaxy populations in Table 2.1. We note that these limits are conservative, as they are evaluated at the upper end of each redshift interval, as this allows the samples to be volume complete. Star formation rates (SFR) are generated by comparison of the observed galaxy supercolours with those of the Bruzual & Charlot models (Wild et al., 2016; Wilkinson et al., 2021).

Table 2.1: 90% stellar mass completeness limits in units $\log(M_*/M_\odot)$ for the star-forming, quiescent and PSB populations in each redshift bin. Mass completeness limits are calculated following the method of Pozzetti et al. (2010).

	0.5 < z < 1	1 < z < 1.5	1.5 < z < 2	2 < z < 3
Star-forming	8.85	9.22	9.53	9.95
Quiescent	9.2	9.74	10.17	10.72
PSB	9.06	9.48	9.81	10.22

2.2.4 Environment Measurements

We measure the galaxy environments in a statistical manner, following a similar method to Lani et al. (2013), but applied to the newer DR11 catalogue and photometric redshifts.

In brief, each galaxy has their local density (ρ_{250}) measured by construction of a cylinder centred on the galaxy of fixed radius 250 kpc and depth equivalent to ± 0.5 Gyr along the redshift direction. The number of galaxies within the cylinder is counted and normalised to the expected number, given the density of galaxies in the wider field within the same redshift range (allowing for holes and edges). The depth of ± 0.5 Gyr is assigned as it is significantly larger than the 1σ uncertainty of $\delta z = 0.0187(1+z)$ on the photometric redshifts (Almaini et al., in preparation): for example, at $z = 1$, the 1σ redshift error corresponds to 0.151 Gyr, and hence a depth of 0.5 Gyrs corresponds to 3.3σ. It should be noted we cannot say with certainty if an individual galaxy is in a cluster or in the field; however, due to the large sample size, we can group galaxies into high- and low-density environments, to investigate density-dependent behaviour in a statistical manner. The robustness of our environmental measurements is explored further in Section 2.4.

We split the catalogue into broad redshift intervals, and within each redshift interval galaxies are sorted into three environmental bins: high, medium, and low density. The three categories are obtained by sorting galaxies by ρ_{250} and splitting into equal thirds (equal numbers of galaxies in each category) for galaxies with stellar mass $M_* > 10^{9.91}$ $M_\odot$, as shown in Figure 2.1. This stellar mass represents the 90 per cent completeness limit for galaxies at our upper redshift bound ($z = 3$), as described in Section 2.2.1. We measure environments using only galaxies above this mass limit, to ensure that environments are compared with reference to a similar galaxy population at all redshifts. Galaxies below this mass limit are also assigned environmental bins, but using environments defined by the galaxies with $M_* > 10^{9.91}$ $M_\odot$. In the later analysis, we are implicitly assuming, for simplicity, that galaxies will remain within their broad density thirds as they evolve, even if the galaxy itself is transformed or quenched. The impact of these assumptions will be explored and tested further in Section 2.4.

2.3 Results

2.3.1 Global Mass Functions

In Figure 2.2, we show the global SMFs of star-forming, quiescent and PSB galaxies as a function of redshift. The number density uncertainties are simply the Poisson counting errors. We see the expected result (see e.g. Muzzin et al., 2013): the star-forming mass

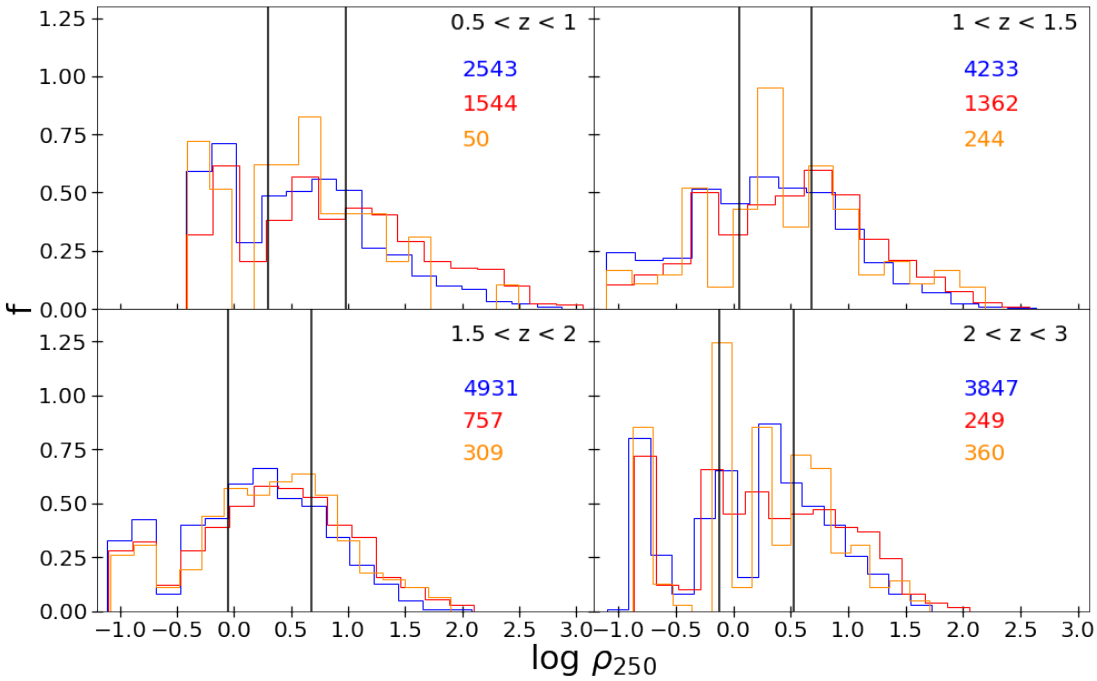

Figure 2.1: Histograms of environmental density ρ_{250} in our four redshift intervals, displayed separately for the star-forming (blue), quiescent (red) and post-starburst (yellow) galaxy populations. Our ρ_{250} values are calculated as described in Section 2.2.4. Solid black vertical lines in each panel represent the ρ_{250} values at which we split the total (combined) population to provide three density bins containing equal numbers of galaxies with $M_* > 10^{9.91}$ $M_\odot$. The total number of galaxies in each population is indicated.

function shape remains almost constant across cosmic time, while the quiescent mass function shows a large build up in number density towards low redshift, especially at the high-mass end. At redshifts below $z = 1$, the quiescent galaxy SMF shows a more significant build up at the low mass end. We see a change in the PSB mass function across redshift, confirming the results of Wild et al. (2016); at high redshift ($z > 1.5$), the PSB mass function is similar to that of the quiescent population, but at lower redshifts there is an upturn in the relative number of PSBs at lower stellar masses, more closely resembling the shape of the star-forming galaxy mass function (see also Maltby et al., 2018). Our extension to $z = 3$ confirms that the PSB and quiescent mass functions are essentially the same at the highest redshifts; performing a Kolmogorov–Smirnov (KS) test on the shape of the PSB and quiescent SMFs in the redshift range $2 < z < 3$, we cannot reject the null hypothesis that they are drawn from the same underlying distribution (p = 0.27). This similarity suggests that quiescent galaxies in this redshift

bin could be quenched by the same mechanisms that quenched PSBs. The upturn in the PSB mass function at low redshifts suggests there may be two separate pathways to form PSBs, with a mechanism that creates low-mass PSBs acting preferentially at $z < 1$ (see Wild et al., 2016; Maltby et al., 2018).

2.3.2 Mass Functions Split by Environment

Figure 2.3, row 1 shows the SMFs for the star-forming galaxy populations as a function of redshift and environment. The SMFs are very similar overall in amplitude as expected, however there is evidence for a relative deficit of low mass star-forming galaxies in high-density environments at low redshift ($z < 1$). Comparing star-forming galaxies in high-density and low-density environments, at low stellar mass ($M_* < 10^{10}$ $M_\odot$) and low redshift ($z < 1$) the difference is formally significant to 16σ.

Figure 2.3, row 2 shows the SMFs for the quiescent galaxies as a function of redshift and environment. As expected, we see growth in the number density of quiescent galaxies towards low redshift. In the redshift interval $1.5 < z < 3$ the mass functions across all three environments are similar. We see that from $z = 2.0$ to $z = 0.5$ there is evidence for an increase in the relative abundance of quiescent galaxies in dense environments versus sparse environments, suggesting that quenching is more effective in dense environments towards lower redshift. This is especially significant ($\sim 7\sigma$) for low mass quiescent galaxies ($M_* < 10^{10}$ $M_\odot$) at $z < 1.5$. Similar results have been found in earlier work (e.g. Mortlock et al., 2015; Annunziatella et al., 2016; van der Burg et al., 2018; Socolovsky et al., 2018; van der Burg et al., 2020).

Figure 2.3, row 3 shows the SMFs for PSBs within the UDS, as a function of redshift and environment. There is only marginal evidence for an excess of PSBs in the dense environments at high stellar mass, but at low stellar mass ($M_* < 10^{10}$ $M_\odot$) we see an up-turn in the relative abundance of PSBs in dense environments at $z < 1.5$, mirroring a similar trend in the older quiescent galaxies. In the redshift bin $0.5 < z < 1$, for low-mass galaxies ($M_* < 10^{10}$ $M_\odot$), the excess of PSBs in high versus low-density environments is formally significant to $\sim 9\sigma$. The PSB SMFs are similar in all environments at $z > 2$, indicating that environment may only play a role in rapid quenching at lower redshifts. These results are consistent with the work of Socolovsky et al. (2018), who also found an excess of lower mass PSBs in dense environments at $z < 1$, in their case by splitting

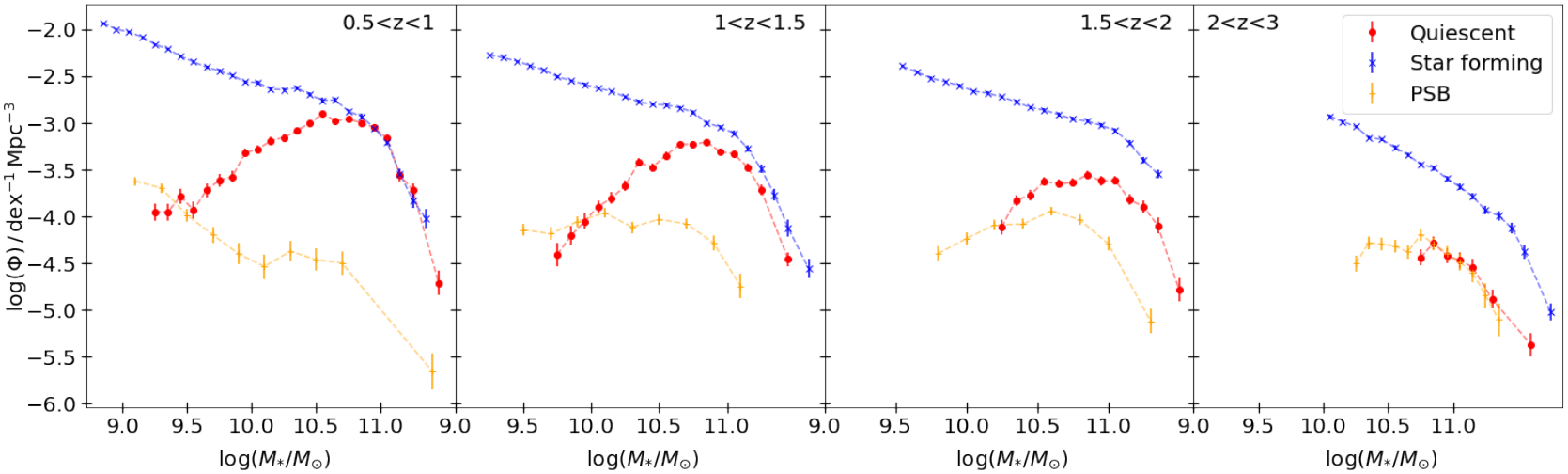

Figure 2.2: Global stellar mass functions for the quiescent (red), star-forming (blue) and PSB (yellow) populations as a function of redshift. The mass functions are cut off at the 90% mass completeness limit for each population, evaluated at the upper end of each redshift bin. Poisson error bars are shown.

the UDS galaxies into 'cluster' and 'field' environments using a friends-of-friends algorithm.

2.3.3 The Growth in the Number of Passive Galaxies and Dependence on Environment

In this section, and Section 2.3.4, we investigate the rate of growth in the number density of passive galaxies in order to estimate a quenching rate. Given the relatively small numbers of PSBs, we combine PSBs and older quiescent galaxies into a single 'passive' galaxy population. Figure 2.4 shows the resulting evolution in number density of the combined passive population from $z = 3$ to $z = 0.5$. The three panels compare the number density evolution split by environment (as defined in Section 2.2.4) in three mass bins (increasing from left to right). We see that the number density of quenched galaxies is higher in high-density environments at all redshifts, especially at the highest masses. The slope of the number density evolution (quantified in Figure 2.5) is also steepest for the highest density environments, indicating star-forming galaxies are more likely to be quenched over a given timescale.

Figure 2.5 shows the growth rate in the passive galaxy number density within the UDS. We calculate this rate by approximating the derivative of the number density evolution:

$$\frac{d\phi_{\mathrm{red}}}{dt} \approx \frac{\phi_{\mathrm{red,\ low\ z}} - \phi_{\mathrm{red,\ high\ z}}}{\Delta t}, \tag{2.1}$$

where $\phi_{\mathrm{red,\ low\ z}}$ and $\phi_{\mathrm{red,\ high\ z}}$ are the passive galaxy number densities in the lower and upper redshift bins respectively, and Δt is the difference in Gyrs between the midpoint of each redshift bin. Errors are propagated from the Poisson counting errors. There is evidence that high-density environments show the highest growth rate at all stellar masses. This trend is most significant in the highest mass bin: comparing low and high-density environments, the differences are significant at 3.3, 3.6 and 2.9σ for $z = 1$, $z = 1.5$ and $z = 2$ respectively. The growth rate in the number of high-mass passive galaxies ($M_* > 10^{10.7}$ $M_\odot$) in the densest environments shows only a small decrease across cosmic time, which seems to imply that the mechanisms causing enhanced quenching for this population are in place from at least $z = 3$.

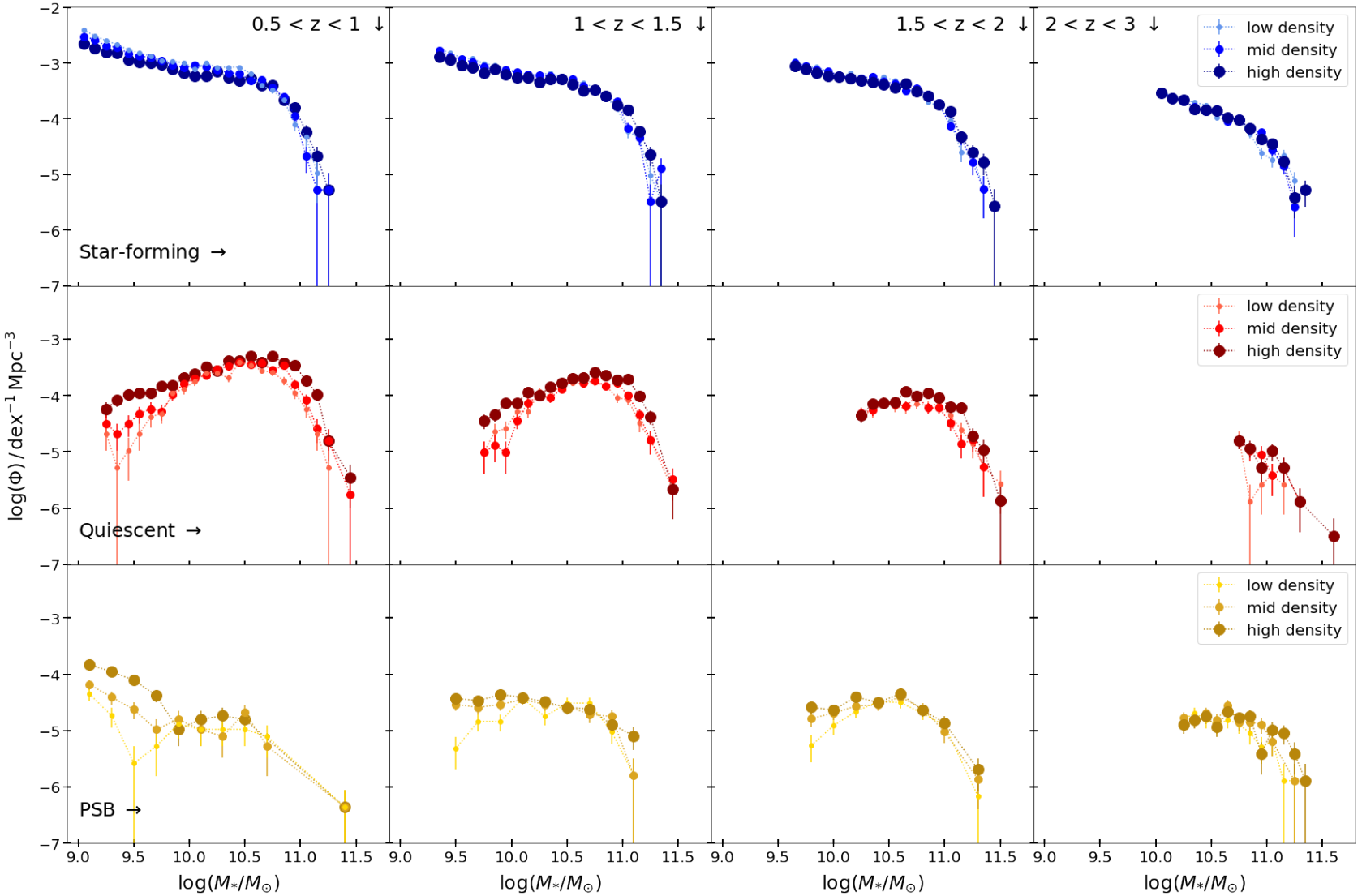

Figure 2.3: Global stellar mass functions for the star-forming (*blue, row 1*), quiescent (*red, row 2*) and PSB (*yellow, row 3*) populations, shown in four redshift intervals, each split into three environmental bins. The three environmental bins are obtained using the combined galaxy population, sorted by ρ_{250} (see Section 2.2.4). Poisson error bars are shown. The mass functions are cut off at the 90% mass completeness limit for each population for the given redshift bin.

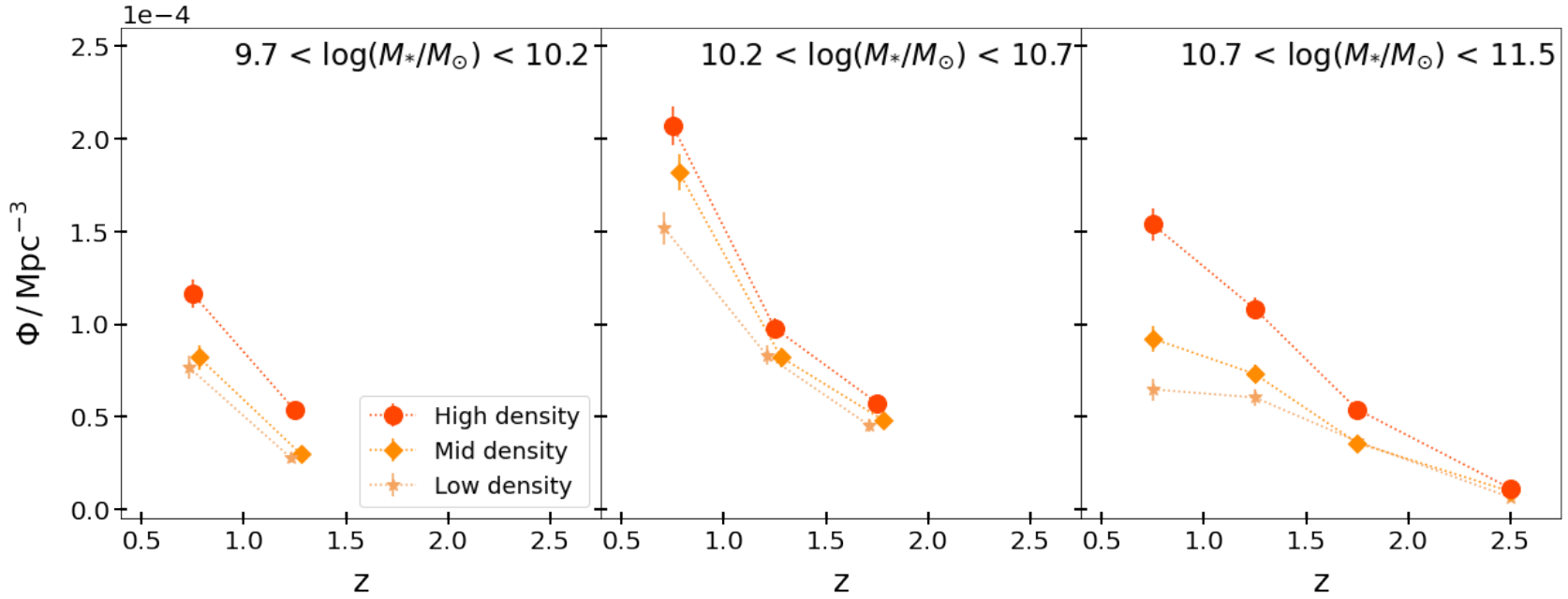

Figure 2.4: The evolution of passive galaxy number density as a function of redshift, split by mass and environment. Density bins are given in the legend, with darker colours and larger markers representing denser environments. Points are plotted at the midpoint of their respective redshift interval and are offset slightly for clarity. Poisson error bars are shown.

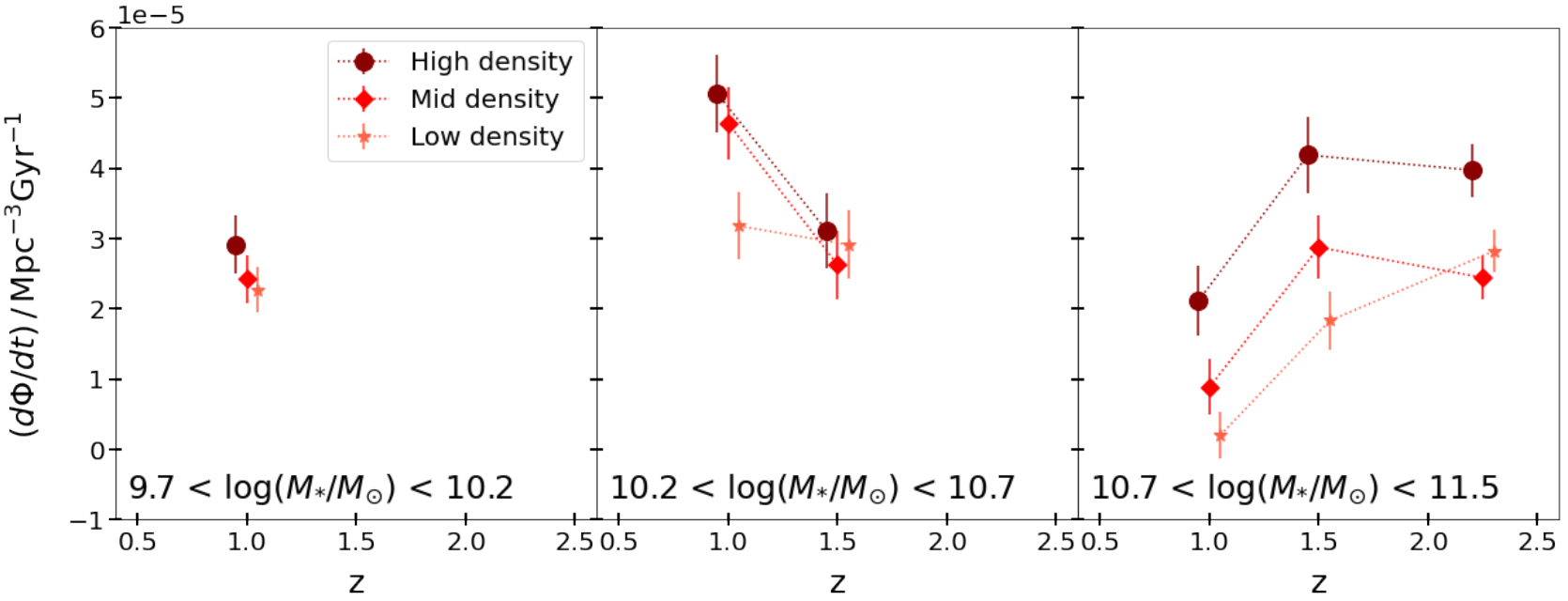

Figure 2.5: The number density growth rate of passive galaxies as a function of redshift, split by mass and environment. Density bins are given in the legend, with darker colours and larger markers representing denser environments. Points are plotted at the boundary between the two redshift intervals used in their calculation and are offset slightly for clarity. Errors are propagated from the Poisson error.

2.3.4 The Probability of Quenching and Dependence on Environment

In Section 2.3.3 we calculated the growth rate in the passive galaxy mass function, but in order to physically interpret this rate as quenching probability we need to consider how many star-forming galaxies are available to be quenched. Figure 2.6 shows the fraction of star-forming galaxies in a given mass and environment bin that are quenched per Gyr, given by:

$$\lambda = \frac{d\phi_{\text{red}}}{dt}\frac{1}{\phi_{\text{SF, high z}}} = \frac{\phi_{\text{red, low z}} - \phi_{\text{red, high z}}}{\phi_{\text{SF, high z}}\,\Delta t}, \tag{2.2}$$

Equation 2.2 is the growth rate (Equation 2.1) divided by the number density of star-forming galaxies in the higher redshift bin – in other words, we calculate the fraction of star-forming galaxies that were available to be quenched from the last timestep that went on to be quenched by the next redshift interval. This simple methodology neglects merging, and also ignores star-forming galaxies that are added to a given mass bin and quenched between the intervening time intervals; the potential impact of these assumptions is explored further in Section 2.4.

At all redshifts and stellar masses we find the quenching rate is higher in the densest environments (see Table 2.2). There is also evidence that the quenched fraction increases with stellar mass, as we see an upward trend at a given redshift from the left to right panels in Figure 2.6.

Perhaps the most striking trend in Figure 2.6 is the enhanced quenching probability in dense environments at a given redshift and stellar mass. The final row in Table 2.2 gives the ratio of the quenching rate in high-density compared to low-density environments. On average, the highest mass galaxies ($M_* > 10^{10.7}$ $M_\odot$) are 1.7 ± 0.2 times more likely to quench per Gyr in the densest third of environments than in the lowest density third. This value is a weighted mean of the high- and low-density ratios in the three redshift bins. If we use all mass bins we find that a galaxy is 1.5 ± 0.1 more likely to quench in the densest third of environments compared to the low-density third.

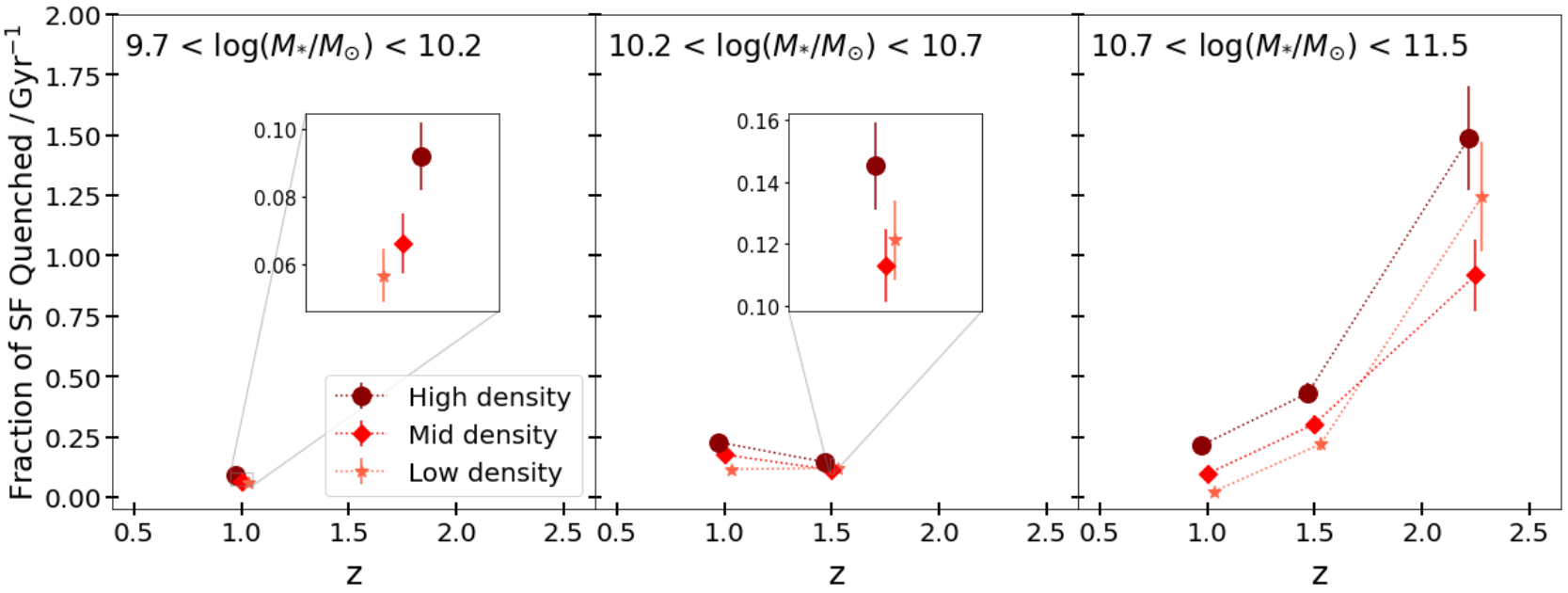

Figure 2.6: The fraction of star-forming galaxies quenched per Gyr as a function of redshift, shown for three density bins and over three ranges in stellar mass. Points are plotted at the boundary between the two redshift intervals used in their calculation and are offset slightly for clarity. Errors are propagated from the Poisson error.

Table 2.2: Fraction of star-forming galaxies quenched per Gyr for each mass and density bin, at each redshift (plotted in Figure 2.6). The final row shows the ratio of high-density to low-density points for each bin.

	$9.7 < \log(M_*/M_\odot) < 10.2$	$10.2 < \log(M_*/M_\odot) < 10.7$		$10.7 < \log(M_*/M_\odot) < 11.5$		
	z = 1	z = 1	z = 1.5	z = 1	z = 1.5	z = 2.25
Low-density	0.057 ± 0.008	0.116 ± 0.012	0.121 ± 0.013	0.023 ± 0.003	0.220 ± 0.028	1.244 ± 0.227
Medium-density	0.066 ± 0.009	0.176 ± 0.016	0.113 ± 0.012	0.097 ± 0.011	0.303 ± 0.037	0.919 ± 0.148
High-density	0.092 ± 0.010	0.228± 0.020	0.145 ± 0.014	0.213 ± 0.021	0.432 ± 0.045	1.488 ± 0.217
High-density / Low-density	1.620 ± 0.285	1.972 ± 0.249	1.198 ± 0.171	9.279 ± 1.522	1.957 ± 0.322	1.196 ± 0.279

2.3.5 Comparison to Low Redshift Empirical Trends

One area of great interest in the literature is whether the effects of galaxy environment and stellar mass on quenching are separable, as this may shed light on the likely physical mechanisms resposible. Peng et al. (2010) looked at this in detail, and concluded that mass quenching and environment quenching are indeed distinct out to $z \sim 1$. Peng et al. identify a mass quenching rate λ_m (their equation 21) which they find depends only on the SFR as follows

$$\lambda_m = \left(\frac{\mathrm{SFR}}{40\, M_\odot\, \mathrm{yr}^{-1}} \right) \mathrm{Gyr}^{-1}. \tag{2.3}$$

To compare our observed overall quenching rate λ with the predicted λ_m from Equation 2.3, we use the median SFR (see Section 2.2) for star-forming galaxies in low-density environments in each of the mass and redshift bins, divided by 40 $\mathrm{M}_\odot$ yr $^{-1}$ as derived empirically by Peng et al. (2010), to produce a prediction the mass quenching rate. We use galaxies in the low-density environments only, to minimise the potential influence of environment. This simple comparison is plotted in Figure 2.7, where the observed and predicted quenching rates are shown in red and blue respectively. In general terms we find that our observed quenching rates broadly follow the mass-quenching predictions from Peng et al. (2010), steadily increasing with both stellar mass and redshift. Formally, the predictions slightly over-predict the observed quenching rates at low densities, particularly at low stellar mass. As noted in Section 2.1, other studies have found evidence for a more complex relationship between quenching and environment at $z > 1$ (e.g Balogh et al., 2016; Kawinwanichakij et al., 2017; Mao et al., 2022), but a detailed comparison is beyond the scope of this work. In broad terms, however, we find that the evolution of the quenching rates do broadly follow the trends expected if quenching is driven by two independent mechanisms: one related to SFR, and the other related to environment.

2.4 Robustness Tests

In this section we explore some of the simplifying assumptions that we have made to this point, and discuss some of the resulting caveats.

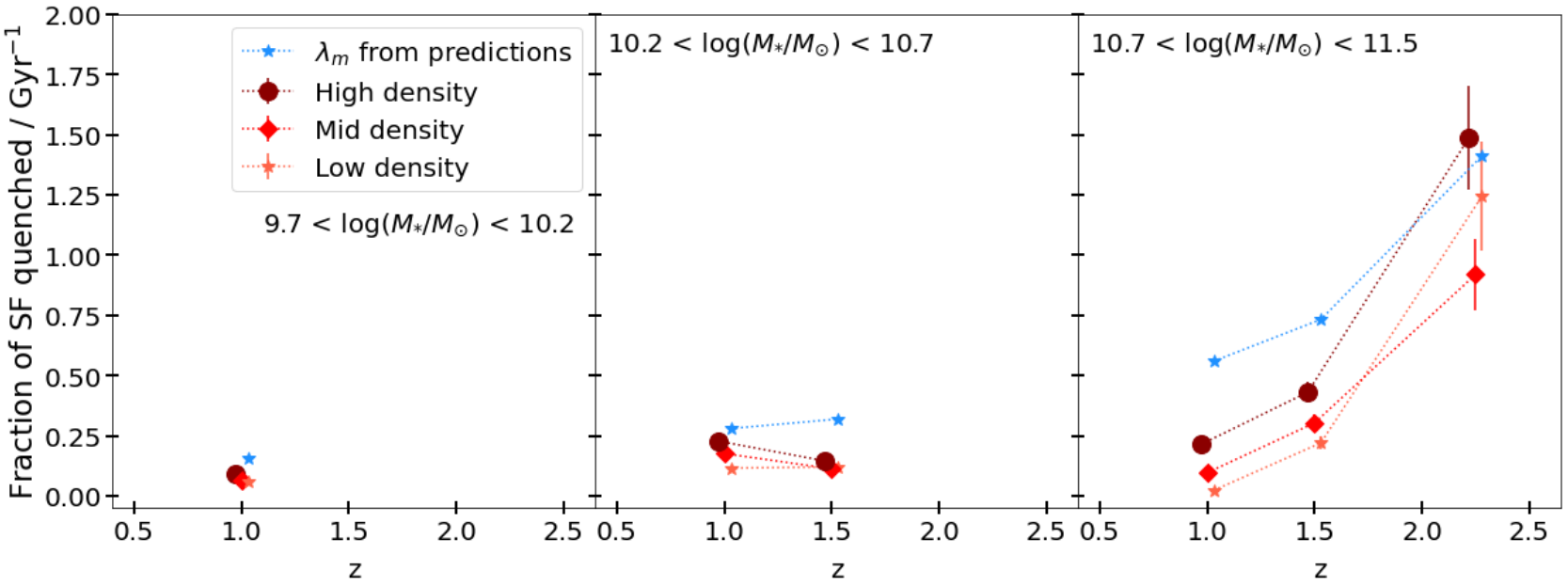

Figure 2.7: A simple comparison of the quenched fraction of star-forming galaxies (red points) to λ_m predictions using Equation 2.3 (blue points). Points are plotted at the midpoint of their respective redshift interval and are offset slightly for clarity. Errors are propagated from the Poisson error.

2.4.1 Growth Through Mergers

One issue that we have not considered thus far is that galaxies no longer forming stars may still increase in stellar mass via mergers, and consequently move to higher mass bins, contributing to a change in the mass functions. To estimate the magnitude of the effect mergers may have on the derived quenching rates, we use the fractional (major) merger rate found for the UDS by Mundy et al. (2017), which at these redshifts is approximately $\mathcal{R}(z) \sim 5 \times 10^{-2}$ Gyr^{-1}. Applying this rate to the quiescent galaxies, we find that correcting for major mergers has only a small impact on the quenched fraction, increasing the number by ~ 10 %. It is worth noting, however, that while the overall impact is expected to be small, the impact of mergers may not be the same in all environments.

Minor mergers may also occur, and growth due to minor mergers is thought to be similar to that of major mergers (e.g. Ownsworth et al., 2014). However, since the mass bins we use to estimate quenching rates are relatively wide, and minor mergers involve galaxies with mass ratios of 1:10 or higher, they should not cause a significant impact on the results. Galaxies may move to slightly higher masses, but in general this will not have a major effect on the overall number densities of the quiescent populations.

2.4.2 Replenishment of Star-forming Galaxies

Another factor to consider is that the pool of star-forming galaxies may not be entirely complete for the redshift intervals studied. While some star-forming galaxies are being quenched and becoming quiescent, others are being formed, or moved to higher stellar mass through star formation, and thus potentially becoming available for quenching in the higher mass bin. We can estimate the upper limit for the number of additional star-forming galaxies that are available to be quenched, using the fact that the star-forming stellar mass function is approximately constant over the redshift range of interest (see Figure 2.3). Therefore, to first order, any galaxies quenched are replaced with galaxies of the same stellar mass. To quantify this effect, we can modify Equation 2.2 by adding the number of quenched galaxies back into the star-forming sample:

$$\lambda_{\text{test}} = \frac{\phi_{\text{red, low z}} - \phi_{\text{red, high z}}}{[\phi_{\text{SF, high z}} + (\phi_{\text{red, low z}} - \phi_{\text{red, high z}})]\,\Delta t}. \tag{2.4}$$

This reduces our quenched fraction values by $\sim$ 15 percent. However, this correction should represent the maximum amplitude of the effect, since the timescale available for quenching these newly added star-forming galaxies will be shorter than the time interval Δt.

2.4.3 Photometric Redshift Errors

A potential concern with our environmental measures is that photometric redshift errors become larger at high redshift, and may dilute measures of environment relative to those at lower redshift. This could artificially enhance the growth in the passive population at the highest densities when two adjacent redshift bins are compared, since the lower redshift measurements are more precise. To investigate this effect, we broaden the photometric redshifts in a given redshift bin to match the uncertainties at the next highest epoch, e.g. redshifts in the range $0.5 < z < 1$ are decreased in quality (adding additional Gaussian spread) to match the dispersion at $z = 1.25$. We then redefine our high-, mid- and low-density bins using the ρ_{250} values produced from these new redshift measurements. Running the growth analysis again, we find that redshift errors between epochs produce only a $\sim$ 5 percent increase in our quenched fraction results (Figure 2.6). The trends we see with redshift, mass and density in the original data remain essentially unchanged. The fraction of star-forming galaxies quenched per Gyr remains significantly higher in the densest environments.

2.4.4 The Effect of Including PSBs in the Passive Sample

Since PSBs are recently quenched galaxies, we have included them in our quiescent galaxy sample for the analysis of quenching rates. To quantify the impact of leaving PSBs out of our passive sample, and using purely galaxies classified as older quiescent galaxies by the SC method (see Section 2.2.2), we repeat our analysis while excluding PSBs. As expected, removing PSBs reduces the measured fraction of quenched galaxies, particularly at high stellar mass and high redshift ($z > 2$), but the influence on the

growth rate in the passive population (Figure 2.5) is relatively minor. Consequently, the estimated quenching rate for SF galaxies (Figure 2.6) is also largely unchanged, as is the relative impact of environment. Repeating the analysis outlined in Section 3.4, the ratio of quenching rates in high- to low-density environments changes from 1.7 ± 0.2 to 1.9 ± 0.2 for high- mass galaxies ($M_* > 10^{10.7}$ $M_\odot$) on average, and from 1.5 ± 0.1 to 1.6 ± 0.1 when galaxies of all masses are considered.

2.4.5 The Influence of Merging Halos and Cosmic Variance

Overall, our results indicate that the rate of galaxy quenching is significantly higher for galaxies in denser environments. We note, however, that our analysis implicitly assumes that galaxies largely remain within their broad density bins as the Universe evolves, e.g. galaxies in the top third of the density field remain in the top third in the next redshift interval. This simplification ought to be largely robust to the expected impact of galaxy-galaxy mergers (see Section 2.4.1), but may be expected to break down on larger scales, e.g. due to the evolution of large scale structure over cosmic time. Thus one might expect some galaxies in low-density environments to switch to higher density environments at later epochs. Furthermore, our study implicitly assumes that we have surveyed a representative volume of the Universe within each redshift slice, but even within a ~ 1 deg^2 field, we can expect some variance due to large-scale structure, particularly for rare massive galaxies (e.g. see Moster et al., 2011). Exploring the detailed impact of such effects is beyond the scope of our current analysis.

2.5 The Post-starburst Contribution to the Growth Rate of Quiescent Galaxies

Since PSBs have been very recently and rapidly quenched, they prove to be a useful tool for examining the modes of growth for the quiescent population. Following Wild et al. (2016), we can compare the growth rate of just quiescent galaxies (Section 2.3.3) to the rate PSBs pass through a given redshift bin to estimate the fraction of quiescent galaxies that pass through a PSB phase. We adopt a typical PSB visibility timescale of $\sim$ 250 – 500 Myr found by Wild et al. (2020) when examining the star formation histories of

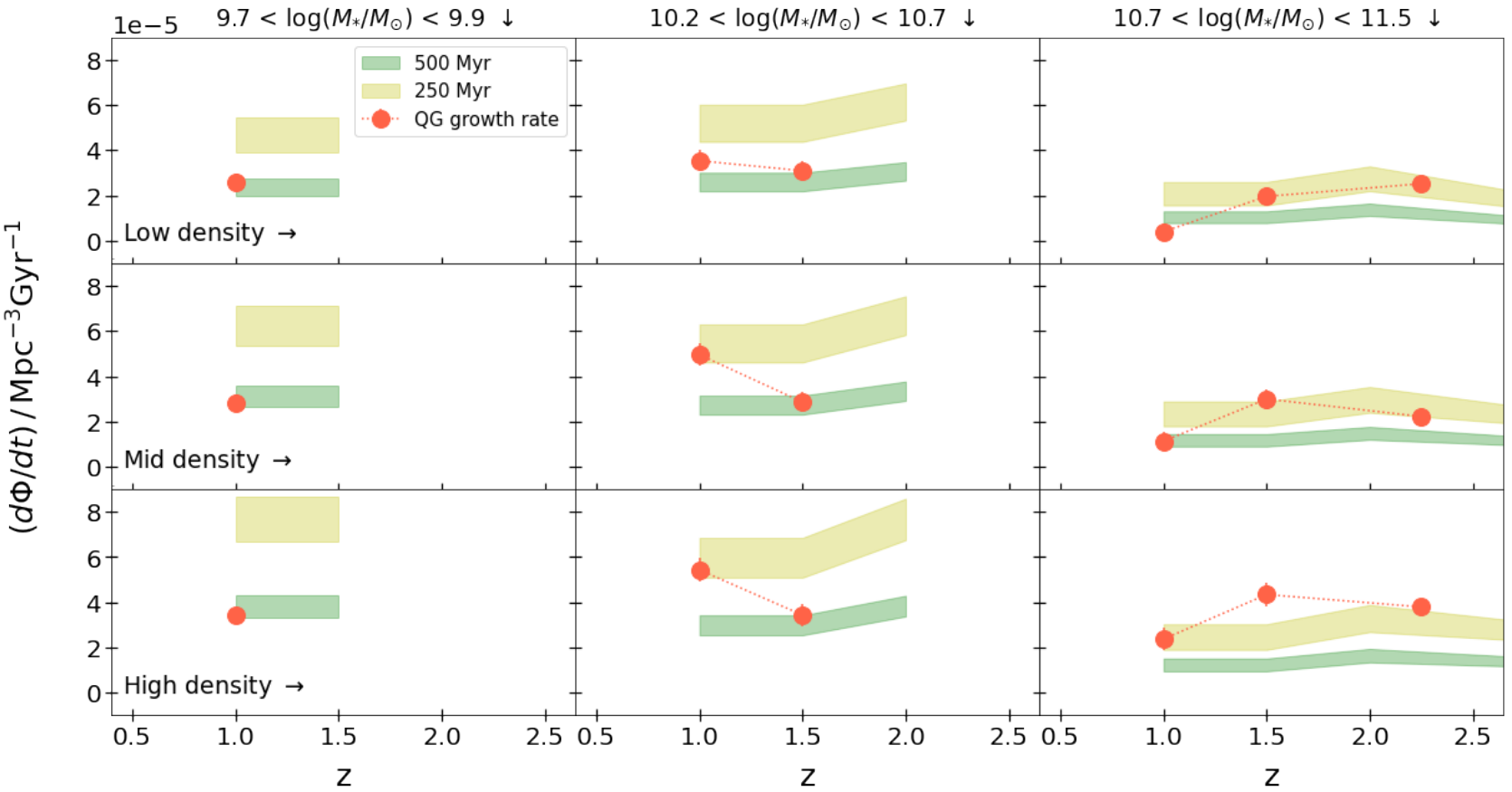

Figure 2.8: The number density growth rate of quiescent galaxies as a function of redshift (red points), in three bins of mass and environment, compared to the predicted PSB contribution assuming a 250 - 500 Myr lifetime. The yellow band shows the PSB contribution assuming a 250 Myr lifetime, with the width showing the 1σ uncertainty, while the green band show the corresponding contribution assuming a 500 Myr lifetime. Mass and density bins are shown in columns and rows respectively. Errors are propagated from the Poisson error.

PSBs, based on fits to spectra and multi-wavelength SEDs. We stress that the visibility timescale is the length of time a galaxy is observed in a PSB phase using the supercolour method, and this timescale may vary in different environments and for different stellar masses depending on burst mass fractions and quenching timescales.

Figure 2.8 shows the predicted contribution of PSBs to the quiescent galaxy growth rate assuming a 250 - 500 Myr visibility timescale. At high stellar mass ($M_* > 10^{10.7}$ $M_\odot$) we find that PSBs reproduce roughly half the number density growth rate of quiescent galaxies if the visibility timescale is $\sim$ 500 Myr, or potentially most of the growth with a shorter visibility time. These results are in good agreement with Wild et al. (2016), which was based on an earlier version of our UDS catalogue, and broadly in agreement with Belli et al. (2019), who found that high-mass PSBs contribute roughly 50% at $z \sim 2$, falling to roughly 20% at $z \sim 1.4$. At intermediate masses we find that PSBs can explain all quiescent galaxy growth, rising to potentially overproducing the red sequence at the lowest stellar masses ($M_* < 10^{10.7}$ $M_\odot$) if the visibility timescales are short. The potential overproduction at low stellar mass may in part be explained if some of the PSBs arise from rejuvenated systems that were previously quenched (e.g Rowlands et al., 2018).

Interestingly, while the quenching rates are higher in dense environments (see also Figure 2.6), this appears to be matched by the increased contribution from PSBs, at least for the range of stellar masses probed in this analysis ($M_* > 10^{9.7}$ $M_\odot$). Therefore, while quenching is more prevalent in dense environments, the fraction of those galaxies that were *rapidly* quenched (according to this simple analysis) does not appear to depend strongly on the density field. At face value this finding appears difficult to reconcile with different quenching mechanisms operating in different environments, unless essentially all quenching mechanisms lead to a PSB phase at these redshifts and stellar masses. It may be that larger samples are required to identify environmental differences in the relative importance of "slow" versus "fast" quenching routes, or perhaps they only become apparent at lower stellar mass. It is notable that the excess of passive galaxies and PSBs in dense environments becomes particularly strong at low stellar mass (Figure 2.3), largely below the limit for our evolutionary analysis ($M_* = 10^{9.7}$ $M_\odot$). Future studies with larger and deeper samples may allow a more detailed investigation of the relative importance of different quenching routes in different environments.

2.6 Conclusions

In this chapter, we present an analysis of the build up of the quenched galaxy population in the UKIDSS UDS from $z = 3$ to $z = 0.5$. We use a PCA analysis, first established by Wild et al. (2014), to identify star-forming, quiescent and post-starburst galaxies in the sample. To investigate the influence of environments we use projected galaxy densities to split the catalogue into three environmental bins within broad redshift intervals. The density field and boundaries are defined using galaxies above the same stellar mass at all redshifts, split by projected galaxy density into equal thirds. The key findings are as follows:

i A higher fraction of passive galaxies are found in dense environments at all stellar masses ($10^{9.7} < M_* < 10^{11.5}$ $M_\odot$) in the redshift range $0.5 < z < 2.0$, as seen from a comparison of stellar mass functions. We also see a sharp up-turn in the relative abundance of low-mass ($10^{9.7} < M_* < 10^{10}$ $M_\odot$) passive galaxies and PSBs in dense environments at $z < 1.5$, which we attribute to the environmental quenching of satellite galaxies entering high-mass halos.

ii The growth rate in the number density of passive galaxies is steepest in the highest density environments at all masses and redshifts (see Figure 2.5). This difference indicates that star-forming galaxies are quenched more efficiently in these environments.

iii The growth in the passive population can be used to estimate the fraction of star-forming galaxies quenched per Gyr at different stellar masses, redshifts and environments (see Figure 2.6). We find that the quenching probability increases with both stellar mass and environment. For the most massive galaxies ($M_* > 10^{10.7}$ $M_\odot$) the quenching probability also increases with redshift, broadly consistent with the quenching probability being proportional to star formation rate.

iv Averaging over all redshifts and stellar masses, we find that star-forming galaxies are 1.5 ± 0.1 times more likely to quench in the densest third of environments compared to the lowest density third. For the most massive galaxies ($M_* > 10^{10.7}$ $M_\odot$) the enhancement factor is 1.7 ± 0.2. Given the dilution effects of projection in our ability to determine environments, these factors are almost certainly lower limits.

v At high stellar mass PSBs can account for roughly half of the build-up in the quiescent mass function, assuming a visibility time of 500 Myr, in agreement with previous studies (Wild et al., 2016; Belli et al., 2019). At low stellar masses the PSB route appears to account for a larger fraction of quiescent galaxies, potentially overproducing the growth rate if the visibility time is significantly shorter than 500 Myr (Figure 2.8).

This study is a first attempt to separate out the influence of environment on the build-up of the passive and PSB stellar mass functions at high redshift ($z > 1$). We find strong evidence that galaxies quench more rapidly in dense environments at a given stellar mass and redshift. Our work is based on photometric redshifts, however, and therefore quantifying the precise dependence on environment is challenging. The next generation of multi-object NIR spectrographs (e.g VLT MOONS, Subaru PFS) should produce the next breakthrough in this field, for the first time providing rest-frame optical spectra for thousands of quenched galaxies at high redshifts. Surveys with these instruments should allow a more precise characterisation of the density field, while also allowing a comparison of the detailed astrophysical properties of galaxies in different environments. By comparing star-formation histories, quenching timescales, metallicities, and AGN contributions, it may be possible to separate the detailed influence of environment and distinguish between quenching mechanisms.

Chapter 3

High-velocity Outflows Seen in Old $z > 1$ Recently Quenched Galaxies With No AGN Signatures

The work presented in this chapter is to be published in Taylor et al. (submitted). In this chapter, all statistical analyses are my own work, however measurements of stellar mass, burst ages and any relevant galaxy classifications are drawn from the principal component analysis published in Wilkinson et al. (2021). Data reduction of the spectra was undertaken by the survey teams, as well as any spectroscopic redshifts used (McLure et al., 2013; Bradshaw et al., 2013; Maltby et al., 2016; McLure et al., 2018).

3.1 Introduction

An important mechanism used in models and simulations of quenching is feedback, both from stellar activity and active galactic nuclei (AGN; see Heckman & Best, 2014; Veilleux et al., 2020, and references therein, and Section 1.3.1.1). Feedback can generate outflowing galactic-scale winds detectable out to the virial radii of a galaxy (e.g. Murray et al., 2011; Borthakur et al., 2013). High-velocity outflows are ubiquitous in star-forming galaxies at cosmic noon, both with and without AGN (e.g. Hainline et al., 2011; Bradshaw et al., 2013; Cimatti et al., 2013; Bordoloi et al., 2014; Talia et al., 2017), but

are uncommon in old quiescent galaxies at the same epoch (e.g. Maltby et al., 2019).

Feedback from both AGN and star formation has been inferred in many post-starburst galaxies through the presence of outflows (see Section 1.4.1). Outflows have been detected in $z \sim 0.1$ PSBs hosting AGN by Baron et al. (2017, 2018, 2020), and at $z \sim 0.6$, with ~ 1000 kms^{-1} outflows observed (Coil et al., 2011; Diamond-Stanic et al., 2012; Sell et al., 2014; Perrotta et al., 2021). At high redshift, studies have found high-velocity (~ 1500 kms^{-1}) outflows in samples of PSBs with signs of AGN (Man et al., 2021; Davies et al., 2024), and without (Maltby et al., 2019). Recently, some work has been done to investigate how outflows evolve alongside host galaxy properties, such as SFR, in the local Universe (Sun et al., 2024). The authors found evidence that outflow velocities diminish with time since quenching. Until now, no such study has been undertaken at high redshift.

In this chapter, we investigate high redshift ($z \geq 1$) PSBs and recently quenched galaxies within the Ultra Deep Survey (UDS; PI: Almaini) field, along with highly star-forming and passive galaxies. We stack optical spectra of recently quenched galaxies to explore whether outflow properties vary with time since a starburst. We expand on the work of Maltby et al. (2019), exploring galactic scale winds as a function of evolutionary stage.

The structure of this chapter is as follows: In Section 3.2 we present our data, sample selection and the stacking procedure. In Section 3.3 we outline our methods and results, and discuss these further in Section 3.4. We end with our conclusions and a brief summary in Section 3.5.

3.2 Data

The UDS photometric imaging used in this chapter is as described in Section 2.2.1.

3.2.1 Galaxy Properties and Classification

To separate star-forming galaxies, passive galaxies, and PSBs, we use the principal component analysis (PCA) technique established by Wild et al. (2014, 2016), as described in Section 2.2.2. In this work, we use the photometric SC galaxy classifications to split

our sample. For post-starburst galaxies, photometric classification is arguably more reliable than spectroscopy alone (see Wild et al., 2020), since it samples a much wider portion of the SED. Galaxy properties used in this work (e.g. stellar mass, burst mass fraction, time since burst) are derived from the fitting of several 10,000's of Bruzual & Charlot (2003) stellar population models to the first three supercolours, with the precise number of models depending on the redshift of the galaxy. These "stochastic burst" models are the same as those used in Kauffmann et al. (2003), and are formed from exponentially declining SFRs with random δ-function bursts with varying strengths and ages superposed. They have a range of formation times, exponential decay times, metallicity and dust contents. Galaxy properties are then estimated from the median of the posterior probability distribution in the usual way. For full details of the method, see Kauffmann et al. (2003). Of particular importance in this work are the burst mass fraction (f_{burst}) and time since burst (t_{burst}) properties. Burst mass fractions are calculated as the fraction of stellar mass formed in bursts in the past Gyr compared to the total stellar mass. The t_{burst} values provide the lookback time to the last burst in the galaxy star-formation history. The supercolour technique was originally established using the UDS DR8 catalogue (Wild et al., 2014), and in this work we use the analysis applied to the full DR11 catalogue (see Wilkinson et al., 2021).

3.2.2 Spectroscopy

The UDS contains ~ 8000 sources with deep optical spectroscopy – assembled from several programmes which target a large range of galaxy types – from star-forming to passive. The UDSz is the spectroscopic component of the UDS, where spectra were obtained for over 3000 K-band selected galaxies using both the VIMOS and FORS2 instruments on the ESO VLT, as part of the UDSz ESO Large Programme (180.A-0776, PI: Almaini)[1]. UDSz-FORS2 (McLure et al., 2013) and UDSz-VIMOS (Bradshaw et al., 2013) have spectral resolutions of R ~ 660 and 200, and exposure times of 5.5 and 2.6 - 4.5 hours, respectively. The VIMOS instrument was used by Maltby et al. (2016) for spectroscopic follow-up of an additional ~ 100 photometrically selected post-starburst galaxies identified in Wild et al. (2014) (UDSz-VIMOS+, 094.A.0410, PI: Almaini), to confirm the validity of their principal component analysis. For the ancillary UDSz-VIMOS+, the observations have R ~ 580 and an exposure time of 4 hours. The UDS

[1] https://pleiades.nottingham.ac.uk/ppadm1/UDSz

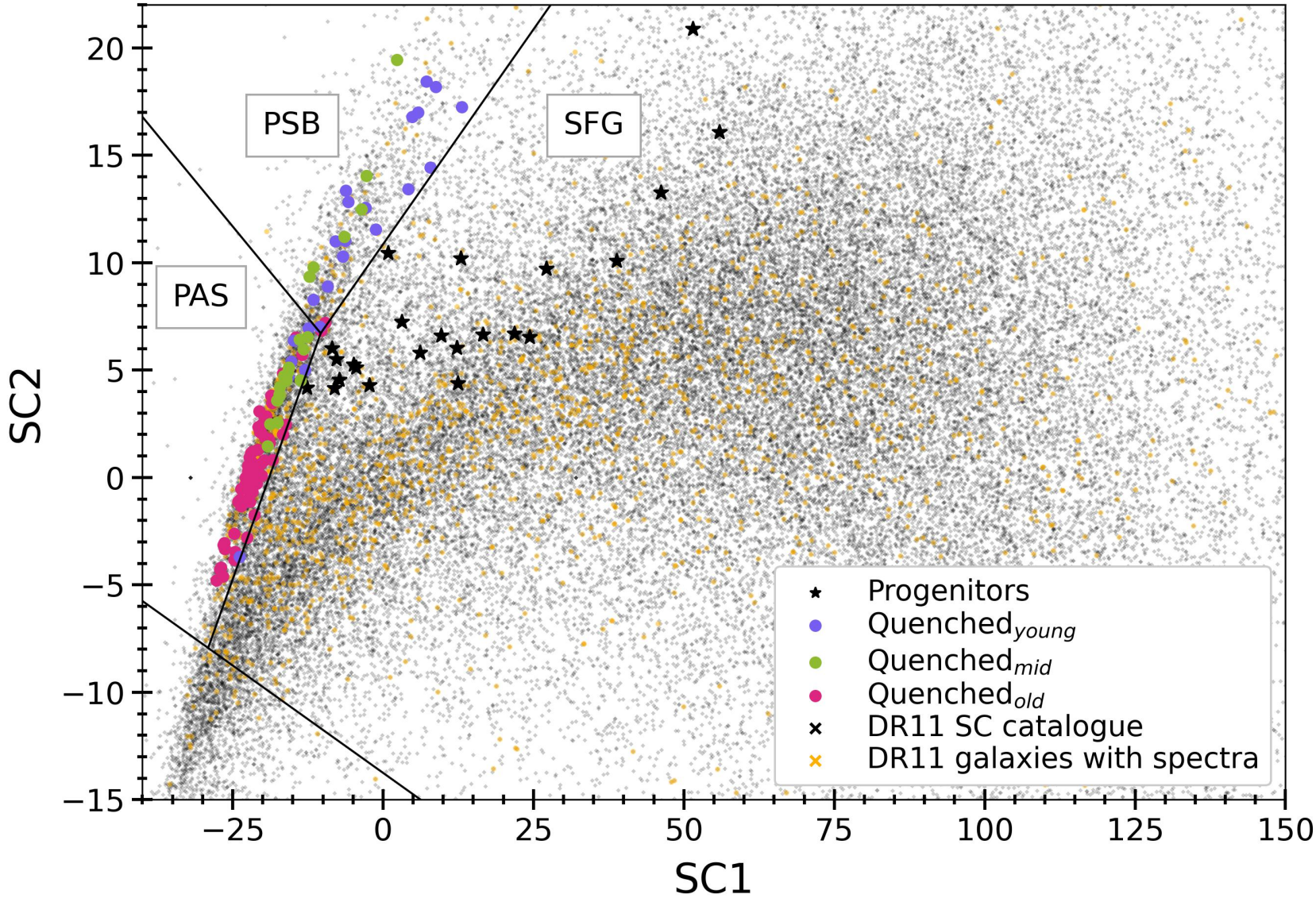

Figure 3.1: SC1-SC2 diagram showing the locations of the different groups within our sample. The four groups (Progenitors, Quenched$_{young}$, Quenched$_{mid}$, and Quenched$_{old}$) represent a time sequence since the last starburst. SC1 and SC2 correlate with mean stellar age and stellar mass build-up within the last Gyr, respectively.

Table 3.1: Final sample numbers and properties of our galaxy groups. The four groups represent a time sequence since the last starburst. For our quenched (Quenched$_x$) groups, the numbers shown in brackets are those for passive galaxies and PSBs respectively. The last section of the table shows median values for each property.

	Progenitors	Quenched$_{\rm young}$	Quenched$_{\rm mid}$	Quenched$_{\rm old}$
Time since burst (Gyr)	–	≤ 0.6	0.6 - 1	≥ 1
Classification	SFGs	PAS/PSB	PAS/PSB	PAS/PSB
Other criteria	Location in SC space	$f_{\rm burst} \geq 0.1$		–
$N_{\rm spectra}$	23	23 (6, 17)	22 (16, 6)	60 (58, 2)
- UDSz-FORS2	11	4 (0, 4)	6 (3, 3)	20 (21, 1)
- UDSz-VIMOS	4	2 (0, 2)	1 (1, 0)	1 (1, 0)
- UDSz-VIMOS+	2	5 (1, 4)	1 (1, 0)	5 (4, 1)
- VANDELS	6	12 (5, 7)	14 (11, 3)	34 (36, 0)
Median values				
$\log_{10}(M_*/M_\odot)$	10.20	10.77	10.82	11.02
$z_{\rm spec}$	1.41	1.27	1.30	1.26
$t_{\rm burst}$ (Gyr)	–	0.58	0.75	1.19
$K_{\rm AB}$	21.98	20.69	20.94	20.47
r_e (kpc; $K_{\rm band}$)	1.76	1.01	1.21	2.45
n ($K_{\rm band}$)	1.84	3.13	2.98	3.26

field is also targeted by the VANDELS spectroscopic survey (ESO programme 194.A-2003, McLure et al., 2018; Garilli et al., 2021), which provides spectra with exposure times of 20 or 40 hours, and a resolution of R ∼ 580. Spectroscopic redshifts ($z_{\rm spec}$) are determined from these data sets using a cross-correlation of spectral templates via the EZ package (Garilli et al., 2010). In this work, we use spectra with secure redshifts for $z_{\rm spec} \geq 1$, which results in a parent sample of 1522 objects (769 star-forming [SFG], 206 quiescent [PAS] and 45 post-starburst [PSB]).

3.2.3 Sample Selection

In this work, we analyse the structure of the Mg II (λλ2796, 2803Å) absorption profile, which is a sensitive tracer of the low ionisation interstellar medium (ISM). Blue-shifted components in this profile are indicative of ISM outflows. To investigate the evolution of the Mg II absorption feature we select galaxies from our parent sample using the following criteria:

1. Full wavelength coverage of the Mg II and [O II] features ($2700 \leq \lambda \leq 3800$Å) for SFGs, plus additional coverage of the Ca II H & K lines for PAS and PSB ($2700 \leq \lambda \leq 4000$Å). This is to ensure that $z_{\rm spec}$ for the input galaxies is determined using a spectral feature *other* than Mg II.

2. A signal-to-noise per resolution element over the Mg II feature (2700-2900Å) of $S/N_{\rm Mg\,II} > 1$. This removes the influence of poor quality spectra on our stacks.

After checking to ensure redshifts were determined from stellar absorption features and/or bright emission lines via visual inspection, we find 400 objects matching these criteria (269 SFG, 106 PAS and 25 PSB). We then further split our sample into four groups, to represent a likely evolutionary sequence for rapidly quenched galaxies. For our first group, we select star-forming galaxies we consider 'progenitors', using the boundaries SC2 > 4 and SC2 ≥ 0.25 × SC1. We choose these boundaries based on the evolutionary tracks from Wild et al. (2016); we expect most galaxies in this region are likely progenitors for galaxies that will soon quench after forming a large fraction of their mass recently. This is further confirmed using statistical modelling based on simulated galaxy properties obtained using semi-analytical models (Harrold et al., in prep). Our

final three groups contain passive galaxies and PSBs split by time since their most recent starburst, t_{burst} – hereafter $Quenched_{young}$ (t_{burst} < 0.6 Gyr), $Quenched_{mid}$ (0.6 < t_{burst} < 1 Gyr) and $Quenched_{old}$ (t_{burst} > 1 Gyr). The t_{burst} values are based on stochastic burst models, as described in Section 3.2.1, although we note that timescales determined from alternative methods do not appear to affect our conclusions (see Section 3.4.2 for further discussion). For our $Quenched_{young}$ and $Quenched_{mid}$ samples, we also apply a minimum burst mass fraction (f_{burst}) of 10%. The locations of the members of each group within the SC1-SC2 diagram are shown in Figure 3.1. Final sample numbers and median values for the properties of each group are shown in Table 3.1.

3.2.4 Stacking Procedure

To effectively identify any outflow signatures, we undertake a stacking analysis to increase the effective S/N across the Mg II absorption feature. We note that our progenitor sample of star-forming galaxies contains 4 low-resolution (R ~ 200) VIMOS spectra, ~ 17% of the total sample. We therefore artificially broaden the higher-resolution spectra in the sample to match the lower-resolution sample[2]. We shift all individual input spectra to their rest-frame wavelengths using their spectroscopic redshifts. The spectra are resampled onto the same wavelength axis ($\Delta\lambda$ = 0.25Å), preserving the integrated flux, and the entire spectrum is normalised for the total flux over $2700 \leq \lambda \leq 2900$Å with the Mg II profile masked out. The spectra are combined to create a median stack, after which we perform a 3σ clip to minimise the effect of noise: we remove any input spectra where more than 10% of flux points over $2700 \leq \lambda \leq 2900$Å, without masking the Mg II lines, lie 3σ or more away from the median stack. All remaining spectra are then combined to generate a single, final median stack. The effective spectral resolutions of the stacks are $\Delta\lambda_{FWHM}$ ~ 5.4 and ~ 5.6Å for our progenitors and $Quenched_x$ samples respectively. Uncertainties in the stack are the mean of the standard error from 100 bootstrapped simulated stacks. The resulting composite spectra are shown in Figure 3.2. The stacks have been smoothed using a Gaussian filter with σ = 1.5Å for display purposes only – this σ value was chosen as it is below the effective resolution of our stacks (σ_{stack} ~ 2.4Å). Equivalent width measurements for the Mg II, [O II] and Hδ features, and the D4000 index for each group are shown in Table 3.2; the median values for each sample and the values as measured from the stacks are included, and show the

[2]We note that we obtain entirely consistent results if we do not broaden the high resolution spectra.

Table 3.2: Equivalent width measurements of key spectral features for each group, calculated using integration. Columns (2-4) show the wavelength ranges used to calculate the equivalent widths. The 'median' column for each group is the median value of measurements from the individual input spectra. The 'stack' column for each group is the value as measured from the stack (shown in Figure 3.2).

	Blue continuum (Å)	Line (Å)	Red continuum (Å)
$W_{Mg\,II}$ (Å)	2762 - 2782	2784 - 2814	2818 - 2838
$W_{[O\,II]}$ (Å)	3653 – 3713	3713 - 3741	3741 – 3801
D4000	3750 - 3950	–	4050 - 4250
$W_{H\delta}$ (Å)	4030 – 4082	4082 - 4122	4122 - 4170

	Progenitors		$Quenched_{young}$		$Quenched_{mid}$		$Quenched_{old}$	
	Median	Stack	Median	Stack	Median	Stack	Median	Stack
$W_{Mg\,II}$ (Å)	7.4	7.6 ± 1.2	11.9	12.3 ± 0.8	14.3	13.5 ± 1.3	12.3	13.2 ± 0.7
$W_{[O\,II]}$ (Å)	-26.8	-21.0 ± 3.3	-2.5	-2.6 ± 1.1	-0.9	-1.4 ± 0.7	-3.5	- 4.4 ± 1.0
D4000	1.49	1.5 ± 0.08	1.54	1.6 ± 0.08	1.72	1.7 ± 0.06	1.77	1.8 ± 0.05
$W_{H\delta}$ (Å)	3.6	4.9 ± 2.9	5.3	5.8 ± 1.2	4.2	4.3 ± 0.9	1.7	2.1 ± 0.5

expected behaviour with time since burst. The equivalent width values are measured using integration, using the wavelength ranges in Table 3.2.

3.3 Analysis

A visual inspection of our four Mg II profiles shows clear asymmetry in all but the Quenched$_{old}$ sample (t_{burst} > 1 Gyr). The ratio of the sum of the fluxes either side of the Mg II centroid reveals a significant excess of blue shifted absorption ($\sim$ 14%) in our first three groups, implying these galaxies harbour galactic-scale outflows. In Quenched$_{old}$, this excess is only $\sim$ 5%.

In this section, we outline two methods of measuring the outflow velocity, v_{out}, in each sample. We start with a simple double Gaussian model (Section 3.3.1), decomposing the Mg II absorption feature into separate systemic and outflowing ISM absorption components. In the second method, we also include an inital subtraction of the stellar continuum via spectral fitting (Section 3.3.2). The significance of the outflowing component for each method is evaluated using an F-test, which produces a p-value – the necessity of an outflowing component is rejected if $p > 0.05$. The p-values and velocity values for each method are presented in Table 3.3. The uncertainties for all methods are determined by repeating the relevant procedure on 100 simulated spectra generated via a bootstrap analysis. The resulting fits to our absorption profiles presented here are smoothed as described in Section 3.2.4, for display purposes only. All analysis is performed on the non-smoothed stacks. We compare the benefits and drawbacks of each model in Section 3.4.1.

3.3.1 Double Gaussian Model

In order to determine the significance of the asymmetry of our Mg II profiles, and to isolate any outflowing gas, we first use a double Gaussian decomposition model. Following the approach of Maltby et al. (2019), the model is fit using the following procedure:

1. The continuum flux either side of the Mg II profile ($2750 \leq \lambda \leq 2850$Å) is

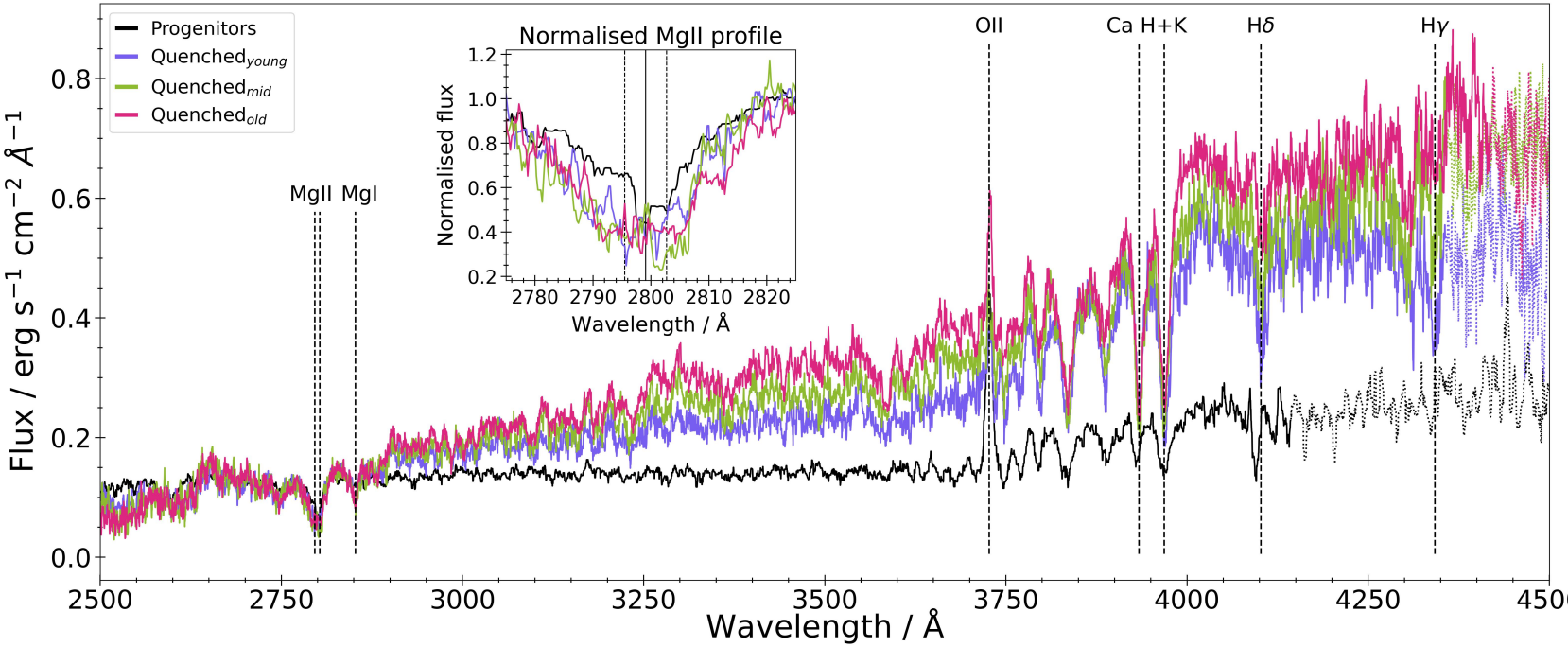

Figure 3.2: Median stacks for each group in our sample. Key spectral features are labeled. The stacks have been smoothed using a Gaussian filter with width σ = 1.5Å for display purposes only. The dotted portion of each stack represents the wavelengths at which less than 50% of input spectra have coverage. The Mg II absorption feature is shown in more detail in the sub-panel, and has been continuum normalised to allow for comparison between stacks. The dashed vertical lines in the inset denote the Mg II λλ2796, 2803Å lines. The solid vertical line denotes the Mg II centroid at 2799.1Å.

normalised, using a smoothing spline fit.

2. Due to the lower resolution of our input spectra, the Mg II doublet ($\lambda\lambda$2796, 2803Å) is unresolved in our stacks, so we first need to estimate the spectral broadening of the absorption feature. To do this, a single Gaussian doublet ($G_{initial}$) is fit to the Mg II profile, with the centroids fixed at the rest-frame wavelengths for systemic absorption. The doublet intensity ratio is set as 1.2:1, as seen for high-z galaxies in Weiner et al. (2009). To avoid any potential contamination of the broadening estimate by outflowing gas, we fit $G_{initial}$ to the red side of the absorption feature only ($\lambda \geq 2803$Å).

3. We then fit the Mg II profile with a two component model, using two Gaussian doublets. The first component (G_{sys}) models the systemic absorption (stellar + ISM) and the second component (G_{out}) models the outflow. The centroid of G_{sys} is fixed at the rest-frame wavelength, while the amplitude is allowed to vary. The centroid and amplitude of G_{out} are left free. The width of both doublets is fixed at the value determined by $G_{initial}$. Comparison of the centroids of the two components provides a wavelength offset, $\Delta\lambda$, which can be used to estimate the velocity offset of the outflowing gas, Δv.

For each group, 100 simulated median stacks are generated via a bootstrap analysis, and the fitting routine is repeated on each stack. The uncertainty in $\Delta\lambda$ is the 1σ error of the resulting 100 velocity measurements.

We then perform a calibration of our velocity offsets (Δv) to estimate the typical outflow velocity, v_{out} of each of our samples. To do this, we follow the procedure presented in Maltby et al. (2019)[3]. We simulate 2000 Mg II profiles exhibiting a range of outflow velocities, with random noise generated to match the typical S/N of our real galaxy spectra. We then generate a median stack of these profiles, and fit the double Gaussian model as described above. We find our model fits recover velocity offsets, Δv, that are systematically ~ 340 kms^{-1} higher than the known median outflow velocity from the simulations, and apply this correction to our Δv values. This is consistent with the findings of Maltby et al. (2019).

The best-fitting Gaussians for each of our groups are shown in Figure 3.3: the top panels show the fit to the full Mg II profile, while the bottom panels show the outflow component

[3]We direct the reader to Appendix A of Maltby et al. (2019) for more detail.

and residual flux after removal of the systemic fit. We find clear evidence for a strongly blue-shifted component within the Mg II feature for our first three samples – progenitors, $\text{Quenched}_{\text{young}}$ and $\text{Quenched}_{\text{mid}}$. The significance of the outflow components for all three groups is $\gg 3\sigma$, as determined from an F-test ($p \ll 0.05$). We find no evidence for any significant asymmetry within the absorption profile of our $\text{Quenched}_{\text{old}}$ galaxies with $t_{\text{burst}} > 1$ Gyr, and the profile is best fit with a single Gaussian doublet, fixed at the rest-frame wavelength ($p > 0.05$). The velocity offsets and corresponding v_{out} values are presented in Table 3.3.

Interestingly, we find that galaxies with a burst over 600 Myr ago ($\text{Quenched}_{\text{mid}}$, $v_{\text{out}} \sim 1500$ kms^{-1}) have similarly high-velocity outflows to those with more recent bursts ($\text{Quenched}_{\text{young}}$, $v_{\text{out}} \sim 1300$ kms^{-1}), in contrast to the findings for local galaxies (e.g. Sun et al., 2024). If these outflows originate from star-formation, we would not expect them to persist at high-velocities so long after the burst, and we discuss this further in Section 3.4.4.

Outflow velocities from the above method relies on the correct modelling of the systemic component. To explore a model independent velocity measurement, we use a boxcar method (e.g. Rubin et al., 2010; Bordoloi et al., 2014; Maltby et al., 2019), which is useful in the case of low S/N stacks. An estimate of the mean outflow velocity, $\langle v_{\text{out}} \rangle$, can be found using

$$\langle v_{\text{out}} \rangle = \frac{W_{\text{tot}}}{W_{\text{out}}} \langle v_{\text{tot}} \rangle, \tag{3.1}$$

where the equivalent width of the outflow component, W_{out}, is

$$W_{\text{out}} = 2(W_{\text{blue}} - W_{\text{red}}). \tag{3.2}$$

Here, W_{red} and W_{blue} are the equivalent widths of the blue side ($2775 \leq \lambda \leq 2796$Å) and red side ($2803 \leq \lambda \leq 2820$Å) of the Mg II feature, W_{tot} is the equivalent width of the full profile, and $\langle v_{\text{tot}} \rangle$ is the mean absorption weighted velocity of the observed absorption line (see Rubin et al., 2010; Bordoloi et al., 2014, for full details). We determine $\langle v_{\text{out}} \rangle$ values of 771 ± 132, 676 ± 62 and 770 ± 62 kms^{-1} for our progenitors, $\text{Quenched}_{\text{young}}$ and $\text{Quenched}_{\text{mid}}$ samples, respectively (see Table 3.3). Our $\langle v_{\text{out}} \rangle$ estimates are lower than those determined from the double Gaussian method, but they nevertheless show

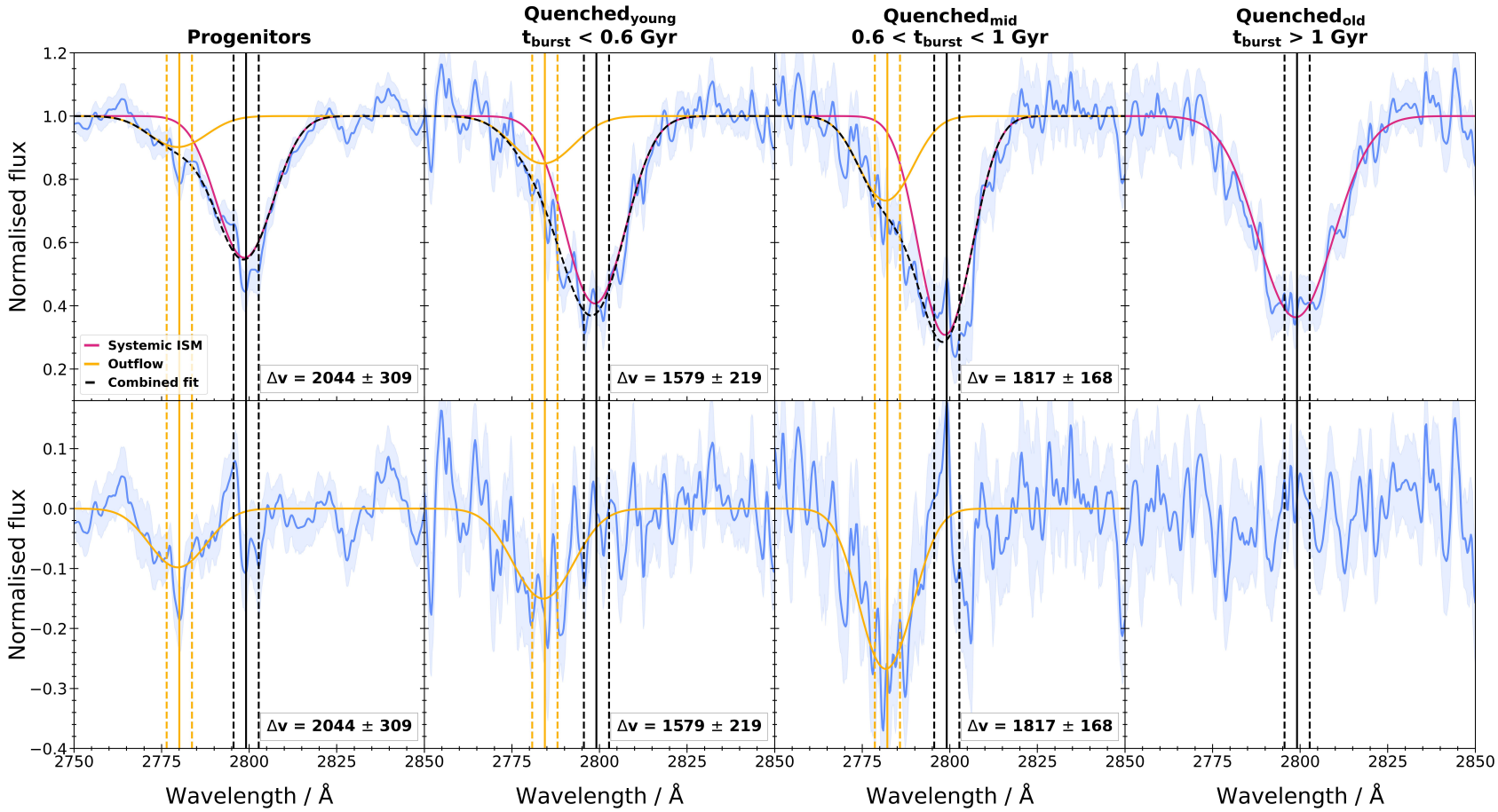

Figure 3.3: Double Gaussian model fits to the Mg II absorption feature for stacked galaxies in each of our four age samples. The spectra have been normalised and smoothed using a Gaussian filter with width σ = 1.5Å for display purposes only. Errors in the stack (light blue shaded area) and velocity measurements are determined using 100 simulated spectra generated through a bootstrap analysis. *Top panels*: the best-fitting model to the absorption feature. The full model (black, dashed) consists of two Gaussian doublets: one fixed to the Mg II rest-frame wavelengths (λλ2796, 2803Å, magenta), and one to model the outflowing gas component (yellow). Black and yellow vertical lines denote the rest-frame and outflow wavelengths respectively. *Bottom panels*: the residual flux with the fitted outflow (yellow) after removal of the systemic ISM fit (magenta, top panels). We find evidence for high-velocity outflows in our progenitors ($\Delta v \sim 2000 \pm 300$ kms^{-1}) and for our Quenched$_{young}$ and Quenched$_{mid}$ ($\Delta v \sim 1500 \pm 200$ and $\sim 1800 \pm 170$ kms^{-1} respectively). We find no evidence to suggest the outflow velocity decreases with t_{burst}, and no significant evidence for outflows in our Quenched$_{old}$ sample.

the outflows persisting through the PSB phase.

3.3.2 Double Gaussian + Stellar Component

In our initial simple fit, we have modelled the systemic stellar and ISM contributions to the Mg II absorption feature as a single component. To determine the impact of this assumption on our results, we use full spectral fitting using synthetic stellar libraries to estimate the contribution of the stellar component to Mg II.

We fit our stacks using the E-MILES stellar population synthesis models (Vazdekis et al., 2016) via the Penalized PiXel-Fitting (`pPXF`, Cappellari & Emsellem, 2004; Cappellari, 2017, 2023) software. The E-MILES library is a theoretical set of models, covering the wavelength range $\lambda\lambda 1680 - 50{,}000$Å and a wide range of metallicities and temperatures. We restrict the library to models with solar metallicity, as expected for high-z galaxies (Sommariva et al., 2012). During the fitting process, we mask the entire Mg II feature to avoid the fit accounting for all the systemic absorption within the stellar component. The fits are performed over the wavelength range 2550 – 4250Å, and then subtracted from the stacks to determine the ISM contribution to Mg II. We then fit the residual flux with a double Gaussian model as described in Section 3.3.1[4], using the offset of the outflowing component centroid to determine Δv. We apply a correction to Δv, as outlined in Section 3.3.1, to determine v_{out} for each sample. We acknowledge that the E-MILES library models lack the youngest stellar populations (age < 30 Myr). This has no implications for our quenched galaxy populations, since these stars will no longer be present. However, the same is not true for our progenitor populations, where such stars are likely to dominate the flux output. Therefore, we repeat our fits using two additional suites of models which include such stars: GALAXEV (Bruzual & Charlot, 2003), and FSPS (Conroy et al., 2009). Reassuringly, we find our results are entirely consistent, regardless of the stellar library used. The best-fitting models for each of our groups are shown in Figure 3.4: the top panels show the stellar component fit using `pPXF`, while the bottom panels show the systemic and outflowing ISM components after removal of the `pPXF` fit.

We find similar velocities to our double Gaussian model using this method, and all

[4]Here we omit step (i) from the model fitting, as removing the stellar component normalises the absorption feature.

are consistent within the errors (see Table 3.3). As we found when using our double Gaussian model, the significance of the outflowing components for our progenitor, $\text{Quenched}_{\text{young}}$ and $\text{Quenched}_{\text{old}}$ samples are much greater than 3σ, and no significant outflow component is needed to account for the profile of the $\text{Quenched}_{\text{old}}$ sample (see Table 3.3 for F-test p-values). Once again, we see the striking trend of high-velocity outflows persisting well into the post-starburst phase.

3.4 Discussion

3.4.1 Comparison of Models

In our analysis, we use two different models to determine an estimate of v_{out} in each of our samples. Our approach in Section 3.3.1 was to simply fit a double Gaussian model to the overall absorption profile, which has the benefit of simplicity, and allows us to determine the significance of the outflowing component. This model could potentially be incorrect, however, if the continuum levels estimated by the spline fit are wrong. In correctly modelling the stellar component in Section 3.3.2, the second method ought to be give a more robust results in principle, but the method is somewhat model dependent, and assumes that we fully understand and trust the stellar libraries.

Overall, our results suggest that a significant high velocity component is present in some fraction of both recently and intermediate quenched galaxies, and this seems to be robust to the method chosen. These high velocities are not necessarily the *characteristic* velocities for our samples, but the presence of such a high-velocity component is clearly important, as it will exceed the typical escape velocity of the galaxy (~ 1000 kms^{-1}), and could be related to the quenching mechanism.

3.4.2 Burst Ages

The super colour t_{burst} ('time since burst') values used in our analysis are calculated by fitting stochastic burst models to the galaxy SEDs from the PCA analysis. To test the robustness of the burst age estimations, we also used the `BAGPIPES` code (Carnall et al., 2018, 2019) to fit the photometry and spectroscopy of our samples simultaneously,

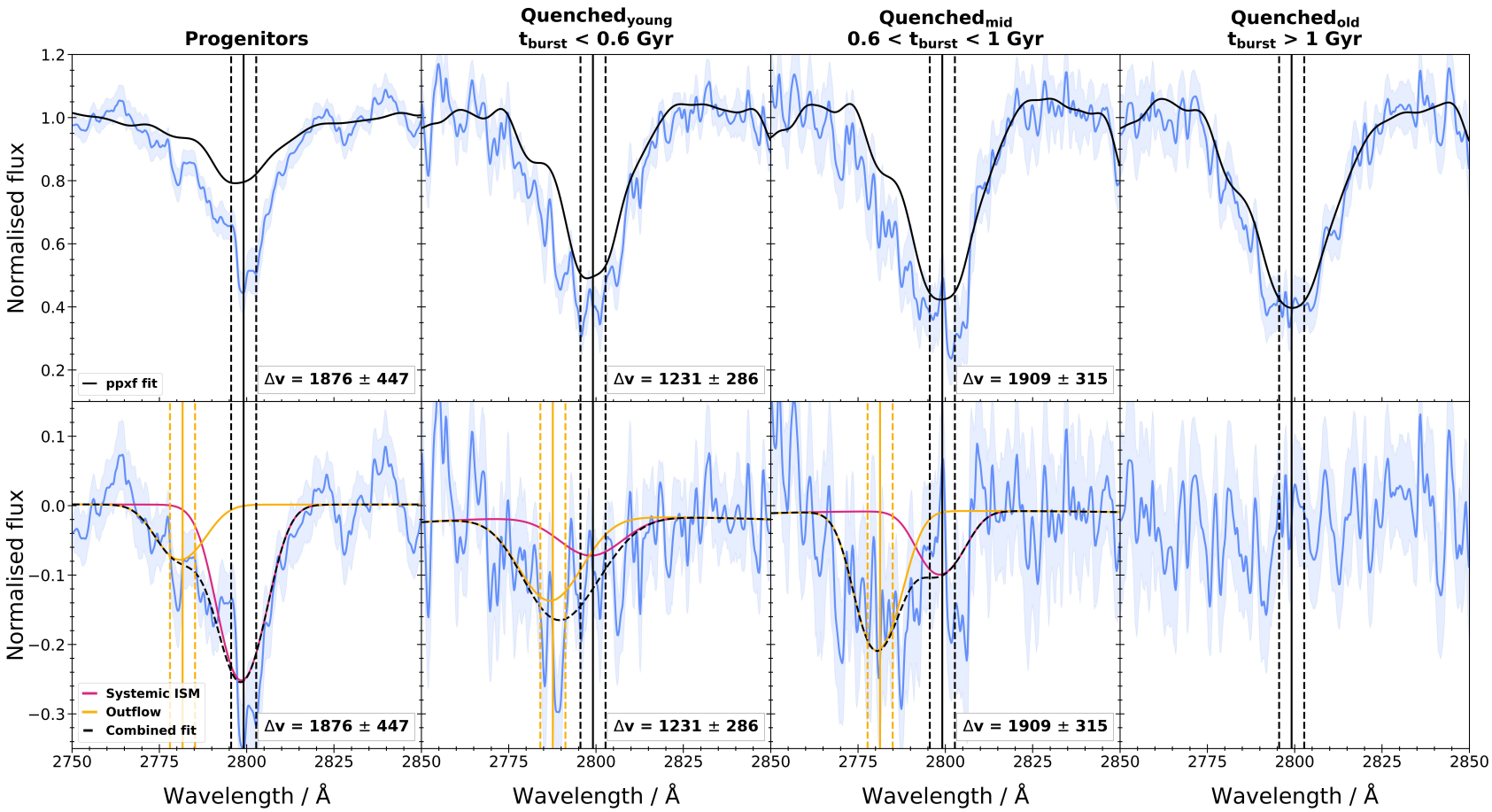

Figure 3.4: Double Gaussian + stellar model fits to the Mg II absorption feature for stacked galaxies in each of our four age samples. The spectra have been normalised and smoothed using a Gaussian filter with width σ = 1.5Å for display purposes only. Errors in the stack (light blue shaded area) and velocity measurements are determined using 100 simulated spectra generated through a bootstrap analysis. *Top panels*: the best-fitting `pPXF` model to the absorption feature, representing the stellar component. *Bottom panels*: the best-fitting model to the spectra once the stellar component (black, top panels) has been removed. The model consists of two Gaussian doublets: one fixed to the Mg II rest-frame wavelengths ($\lambda\lambda$2796, 2803Å, magenta), and one to model the outflowing gas component (yellow). Black and yellow vertical lines denote the rest-frame and outflow wavelengths respectively. We find evidence for high-velocity outflows in our progenitors ($\Delta v \sim 1800 \pm 450$ kms^{-1}) and for our Quenched$_{young}$ and Quenched$_{mid}$ ($\Delta v \sim 1200 \pm 290$ and $\sim 1900 \pm 320$ kms^{-1} respectively). We find no evidence to suggest the outflow velocity decreases with t_{burst}, and no significant evidence for outflows in our Quenched$_{old}$ sample.

Table 3.3: F-test p-values and velocity measurements for each method, where Δv is the velocity offset measured from our fits, and v_{out} is the calibrated outflow velocity, as determined from our simulations. The significance of the outflowing component for each method is evaluated using an F-test, which produces a p-value – the necessity of an outflowing component is rejected if $p_F > 0.05$. Outflows are detected in the progenitor, Quenched$_{young}$ and Quenched$_{mid}$ samples, as seen from the p_F values. Outflows are not detected in the Quenched$_{old}$ sample, and hence we use "–" for this column.

	Progenitors	Quenched$_{young}$ $t_{burst} < 0.6$ Gyr	Quenched$_{mid}$ $0.6 < t_{burst} < 1$ Gyr	Quenched$_{old}$ $t_{burst} > 1$ Gyr
		Double Gaussian model		
F-test for outflow (p_F)	0.0087	0.012	0.0047	0.42
Δv (kms^{-1})	2040 ± 310	1600 ± 220	1800 ± 170	–
v_{out} (corrected, kms^{-1})	1700 ± 310	1300 ± 220	1500 ± 170	–
		Double Gaussian + stellar model		
F-test for outflow (p_F)	0.0011	0.013	0.0046	0.34
Δv (kms^{-1})	1900 ± 450	1200 ± 290	1900 ± 320	–
v_{out} (corrected, kms^{-1})	1500 ± 450	940 ± 290	1500 ± 300	–
		Boxcar		
$\langle v_{out} \rangle$ (kms^{-1})	770 ± 130	680 ± 62	770 ± 62	–

following the method of Wild et al. (2020). We refer the reader to Wild et al. (2020) for the details of the BAGPIPES star-formation history (SFH) modelling. We find that the t_{burst} values from BAGPIPES are strongly correlated with the ages determined from the PCA analysis, but typically $\sim 40\%$ older on average. Repeating the stacking analysis with the new ages, we find that our primary findings are unaffected. Significant, high velocity outflows are still observed in older quenched galaxies ($t_{burst} > 0.6$ Gyr). The only tentative difference is the persistence of outflows ~ 1 Gyr after the burst, which we note is consistent with the older average burst ages from BAGPIPES. Very similar results are obtained using the light-weighted ages from the PCA analysis (Wild et al., 2014), and by using alternative age estimates proposed by Belli et al. (2019), determined from position in a UVJ colour-colour diagram. We conclude that our primary findings are robust: high-velocity outflows are observed in relatively old, quenched galaxies, long after the starburst has ended.

3.4.3 Time Since Quenching

An additional test we undertake is to see if trends differ depending on whether we use 'time since burst', as provided by the SC analysis, or 'time since quenching'. To do this, we use the 'time *of* quenching' parameter, t_{quench} output from the BAGPIPES code. The quenching time is defined using the current SFR as a fraction of the time-averaged SFR over the whole SFH – or the normalised star-formation rate, nSFR, given by:

$$\mathrm{nSFR}(t) = \frac{t\,\mathrm{SFR}(t)}{\mathrm{M_{formed}}}, \tag{3.3}$$

where M_{formed} is the total mass of stars formed up to time t. A galaxy is defined as quenched by the BAGPIPES code once the nSFR value falls below 0.1, and t_{quench} is the age of the Universe at this point. We can then use the t_{quench} values from our BAGPIPES fits to determine the time *since* quenching, t_{sq}, using:

$$t_{sq} = t(z_{obs}) - t_{quench}, \tag{3.4}$$

where $t(z_{obs})$ is the age of the Universe at the redshift of observation.

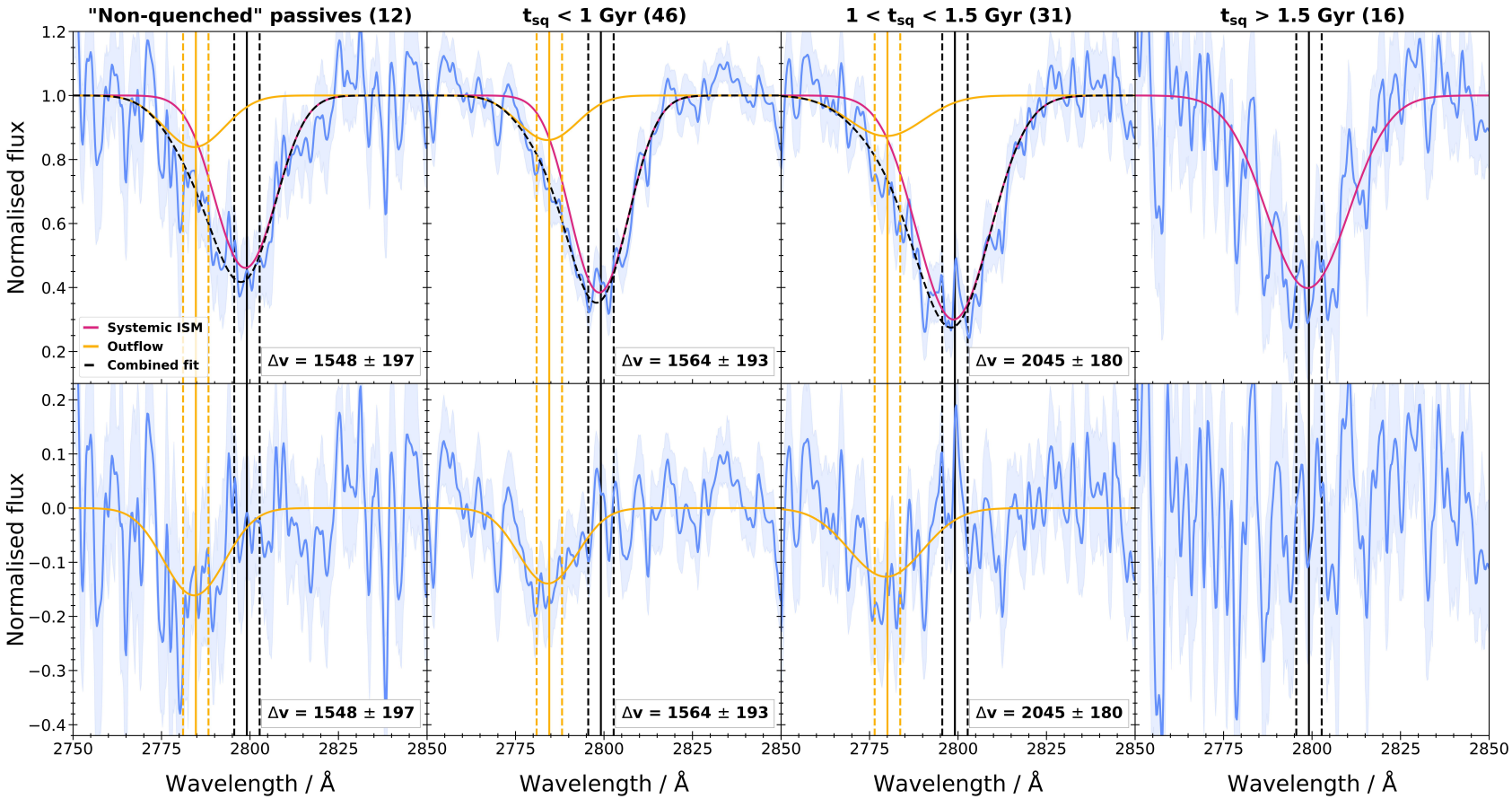

Figure 3.5: Double Gaussian fits to the Mg II absorption feature for stacked galaxies in four groups, split by the alternative time since quenching timescale (t_{sq}) (calculated from BAGPIPES, see Section 3.4.3). The galaxies used are the 105 galaxies within the previously defined quenched samples (see Figure 3.3). The first column shows the 12/105 galaxies which BAGPIPES did not class as quenched. The spectra have been normalised and smoothed using a Gaussian filter with width σ = 1.5Å for display purposes only. Errors in the stack (light blue shaded area) and velocity measurements are determined using 100 simulated spectra generated through a bootstrap analysis. *Top panels*: the best-fitting model to the absorption feature. The full model (black, dashed) consists of two Gaussian doublets: one fixed to the Mg II rest-frame wavelengths (λλ2796, 2803Å, magenta), and one to model the outflowing gas component (yellow). Black and yellow vertical lines denote the rest-frame and outflow wavelengths respectively. *Bottom panels*: the residual flux with the fitted outflow (yellow) after removal of the systemic ISM fit (magenta, top panels). We find evidence for high-velocity outflows in the 'non-quenched' galaxies ($\Delta v \sim 1500 \pm 200$ kms^{-1}) and for galaxies with t_{sq} < 1 Gyr and 1 < t_{sq} < 1.5 Gyr ($\Delta v \sim 1500 \pm 200$ and $\sim 2000 \pm 180$ kms^{-1} respectively). We find no significant evidence for outflows in galaxies with t_{sq} > 1.5 Gyr.

We separate out the 105 galaxies within our previously defined quenched samples into four groups, split by time since quenching: (i) 12 galaxies which are classed as 'non-quenched' by BAGPIPES, meaning their nSFR has not yet fallen below 0.1, (ii) 46 galaxies with $t_{sq} < 1$ Gyr, (iii) 31 galaxies with $1 < t_{sq} < 1.5$ Gyr and (iv) 16 galaxies with $t_{sq} > 1.5$ Gyr. We perform the same double Gaussian fitting routine as described in Section 3.3.1, and the results are shown in Figure 3.5.

After applying the velocity calibration, we find evidence for high-velocity outflows in the 'non-quenched' galaxies ($v_{out} \sim 1200 \pm 200$ kms^{-1}) and for galaxies with $t_{sq} < 1$ Gyr and $1 < t_{sq} < 1.5$ Gyr ($v_{out} \sim 1200 \pm 200$ and $\sim 1700 \pm 190$ kms^{-1} respectively). We find no significant evidence for outflows in galaxies with $t_{sq} > 1.5$ Gyr. These results further suggest that episodic AGN activity may be the driver of the observed outflows, as outflows are still seen in galaxies which have been quenched for 1 - 1.5 Gyr.

3.4.4 Star-formation or AGN Driven Winds?

At first glance, our results seem to support the scenario in which a highly star-forming galaxy collapses to become extremely compact and undergoes a huge starburst, followed by rapid quenching through the removal of gas. Comparing the compactness, $\Sigma_{1.5}$[5], of our samples, we find our Quenched$_{young}$ and Quenched$_{mid}$ groups ($\log_{10}(\Sigma_{1.5}) \sim 10.7$ and 10.5 $M_\odot$ kpc$^{-1.5}$ respectively) are substantially more compact than our progenitors ($\log_{10}(\Sigma_{1.5}) \sim 9.8$ $M_\odot$ kpc$^{-1.5}$). The difference in $\Sigma_{1.5}$ values indicates our progenitors are likely to undergo rapid compaction either before or during the starburst. PSBs at high redshift have been found to be highly compact (e.g. Yano et al., 2016; Almaini et al., 2017; Maltby et al., 2018). Various studies at intermediate redshifts ($z \sim 0.6$) have concluded that high-velocity outflows in quenching galaxies are likely driven by feedback associated with highly compact starbursts (e.g. Diamond-Stanic et al., 2012; Sell et al., 2014; Perrotta et al., 2021; Davis et al., 2023).

Locally, post-starbursts have been found to have decreasing wind velocity with increasing t_{burst}. Sun et al. (2024) found that outflow velocity decreases with elapsed time since an episode of bursty star-formation, for $z < 0.3$ starbursting and PSB galaxies. If the outflows we are detecting in the Quenched$_{young}$ and Quenched$_{mid}$ groups originate from

[5]From Barro et al. (2013); $\Sigma_{1.5} \equiv M_*/r_e^{1.5}$. This parameter effectively removes the slope of the galaxy mass/size relation.

their latest period of star-formation, we would not expect them to persist at high-velocities long after the burst. Our Quenched$_{young}$ and Quenched$_{mid}$ galaxies have typical effective radii of $R_e \sim$ 1-2 kpc; an outflowing wind with velocity v_{out} = 1000 kms^{-1} would travel $\sim$ 100 kpc in 100 Myr, so on timescales longer than this an outflow should have long cleared the galaxies in our sample if they are driven solely by star formation. A simple explanation for this could be that these winds are not fueled by star-formation alone, and are driven by feedback from AGN, as some authors suggest. For example, Tremonti et al. (2007) attribute the $\sim$ 1000 kms^{-1} outflows in their PSB sample to AGN feedback based on detection of [O III] in the spectra, with equivalent width values matching those of powerful AGN. Davies et al. (2024) also found evidence for AGN activity in galaxies with high-velocity neutral gas outflows in the redshift range $1.7 < z < 3.5$ (see also Park et al., 2023).

Our PSB sample shows no AGN signatures in the available optical data (Maltby et al., 2016) or X-ray imaging (Almaini et al., in prep). We may therefore be observing "fossil" AGN outflows, which are expected to persist for several times the duration of the AGN-driven phase (Zubovas & Maskeliūnas, 2023). Episodic AGN activity could persist well into the PSB phase, maintaining the outflows, but due to the short duty cycle catching the PSB in this phase is unlikely (see Luo et al., 2022; Lanz et al., 2022, for examples of low-luminosity AGN in $z < 0.2$ PSBs). In the local Universe ($z < 0.05$), French et al. (2023) found evidence of fading AGN in five PSBs within the Mapping Nearby Galaxies at Apache Point Observatory (MaNGA) survey. They estimate the AGN duty cycle during the PSB phase as $\sim 2 \times 10^5$ yr, and that an AGN spends $\sim$ 5 per cent of time in its 'luminous phase' ($\sim 1 \times 10^4$ yr). The duty cycle for more distant PSBs has not yet been estimated, although there are indications that general AGN duty cycles may be longer at higher redshifts (see Delvecchio et al., 2020).

3.5 Conclusions

In this work, we use the Mg II ($\lambda\lambda$2796, 2803Å) absorption feature at $z > 1$ to investigate how galactic-scale outflows evolve with time since the last starburst (t_{burst}). We stack deep optical spectra from the UDSz and VANDELS surveys, and find clear evidence for high-velocity outflows within our progenitors ($v_{out} \sim 1500 \pm 450$ kms^{-1}), and galaxies with $t_{burst} < 1$ Gyr - $v_{out} \sim 940 \pm 290$ and $\sim 1500 \pm 300$ kms^{-1} for galaxies with $t_{burst} <$

0.6 Gyr and 0.6 < t_{burst} < 1 Gyr, respectively. We find no evidence for outflows in our passive galaxy sample with t_{burst} > 1 Gyr. Our sample show no signs of AGN in their optical spectral features, which may indicate that any AGN in these galaxies have very short duty cycles, and were 'off' when these galaxies were observed. The presence of significant outflows in the older quenched galaxies (t_{burst} > 0.5 Gyr) is difficult to explain with starburst activity alone, and may indicate energy input from episodic AGN activity as the starburst fades.

Chapter 4

JWST EXCELS: Outflows in Post-starburst Galaxies at $z > 3$

The work presented in this chapter is preliminary. In this chapter, all statistical analyses are my own work, however the data reduction and sample selection for EXCELS was performed by the survey team, and is outlined in Carnall et al. (2024).

4.1 Introduction

The launch of JWST has revealed the abundance of recently-quenched and quiescent galaxies at redshifts of $z > 4$ (Carnall et al., 2023a; Alberts et al., 2023). The high SNR of JWST spectroscopy versus ground-based telescopes is allowing, for the first time, in-depth studies of quenching mechanisms in galaxies at cosmic noon and beyond (Belli et al., 2023; Carnall et al., 2023b; Park et al., 2023; D'Eugenio et al., 2023; Setton et al., 2024).

In Chapter 3, we found high velocity outflows in the composite spectra of recently quenched galaxies at $1 < z < 1.5$, which may idicate the presence of episodic AGN activity. In this chapter, we expand on our previous work by undertaking a preliminary analysis of the JWST NIRSpec data of 9 PSBs at redshifts z > 1.8, from the Early eXtragalactic Continuum and Emission Line Science (EXCELS) survey. We utilise these high resolution spectra to establish, for the first time, if outflows are prevalent in

post-starburst galaxies at earlier epochs than cosmic noon. We investigate the Mg II and Na D profiles of the sample, using both a stacking analysis of the whole sample, and fitting of individual objects.

The structure of this chapter is as follows: In Section 4.2, we outline the EXCELS data reduction process and our sample selection. In Section 4.3, we present outflow velocities and mass outflow rates, estimated from a stacking analysis. We then fit individual objects in Section 4.4, as well as outling some future considerations for our modelling. We end with our conclusions and a brief summary in Section 4.5.

4.2 Data

The JWST Early eXtragalactic Continuum and Emission Line Science (EXCELS) survey (Carnall et al., 2024) is a NIRSpec Cycle 2 programme. EXCELS was designed as a follow up to the JWST Public Release IMaging for Extragalactic Research (PRIMER) Cycle 1 survey (Dunlop et al., 2021), a JWST multiband NIRCam survey targeting regions of the UDS and COSMOS fields. EXCELS consists of four NIRSpec MSA pointings within the PRIMER-UDS field, observed with three combinations of gratings and filters (G140M/F100LP, G235M/F170LP and G395M/F290LP) at medium resolution (R $\sim$ 1000). The total exposure times per pointing for the G140M and G395M gratings are $\sim$ 4 hours, and $\sim$ 5.5 hours for the G235M grating.

The EXCELS sample is based on both the VANDELS UDS-HST (McLure et al., 2018) and the PRIMER-UDS (Dunlop et al., 2021, McLeod et al., in prep) photometric catalogues. The survey is built around both massive quiescent galaxies and star-forming galaxies at $z > 1$, however here we focus only on the quiescent galaxy (QG) sample. In brief, the VANDELS QG sample was selected using the following criteria: (i) $1 \leq z_{\rm phot} \leq 2.5$, (ii) $H \leq 22.5$ and $i \leq 25$ and (iii) rest-frame UVJ colour matching the Williams et al. (2009) $z > 1$ selection for passive galaxies. The PRIMER QG sample was selected by first restricting the catalogue to galaxies with coverage in all 11 HST ACS (F435W, F606W, F814W) and JWST NIRCam (F090W, F115W, F150W, F200W, F277W, F356W, F410M and F444W) bands. Galaxies with F356W $\leq$ 25 were then fit using the `BAGPIPES` spectral fitting code (Carnall et al., 2018), following the model used in Carnall et al. (2020, 2023a). Quiescent galaxies were selected using a specific

star-formation rate (sSFR) cut of sSFR < 0.2 / $t_{\rm H}(z_{\rm obs})$, where $t_{\rm H}(z_{\rm obs})$ is the age of the Universe at the redshift of observation. A further cut to the sample was performed based on the joint posterior distribution of a galaxy's redshift and sSFR, requiring 50 % of posterior samples to have both $z > 2$ and sSFR < 0.2 / $t_{\rm H}(z_{\rm obs})$. A 'robust' sub-sample was also defined, requiring 95 % of the joint posterior samples to have $z > 1.75$ and sSFR < 0.2 / $t_{\rm H}(z_{\rm obs})$. Any galaxies not meeting both these criteria were termed 'non-robust'. For full details of the survey selection process, see Carnall et al. (2024).

The full details of the data reduction process are presented in Carnall et al. (2024), however we briefly outline the key steps of the 2D spectral reduction here. EXCELS spectra were reduced by running the level 2 JWST data reduction pipeline using the default configuration, however the sky subtraction step was skipped. Remaining artefacts were then manually masked, and sky subtraction was performed on the masked 2D spectra using custom code. An example 2D spectrum is shown in Figure 4.1. We note that, upon visual inspection, some of the reduced 2D spectra show signs of systematic noise, the cause of which is currently under investigation. 1D spectra were extracted using custom code, with the extraction centroid being set based on the PRIMER F365W imaging. It should be noted that no modification to account for slit losses or imperfect spectrophotometric calibration is performed at this stage. Spectroscopic redshifts were determined manually by two different team members, using the `EZ` software (Garilli et al., 2010), and the results reconciled.

The sample selection and data reduction described above were undertaken by the EXCELS core team, and is presented fully in Carnall et al. (2024).

Many of the EXCELS objects were observed in multiple gratings, over a wide wavelength range. To combine the 1D spectra for these objects, the overlapping regions between the G235M and G395M gratings are determined, and the median flux in these regions is calculated. The G395M spectrum is then scaled to the normalisaton of the G235M spectrum, and the resolutions are matched using the `SPECTRES` code (Carnall, 2017) – here we reduce the resolution of the shorter-wavelength G235M spectrum. The flux in the overlapping regions is then averaged. We repeat the above steps for the G140M and G235M/G395M spectra, reducing the resolution of the G140M spectrum to match that of the newly combined data.

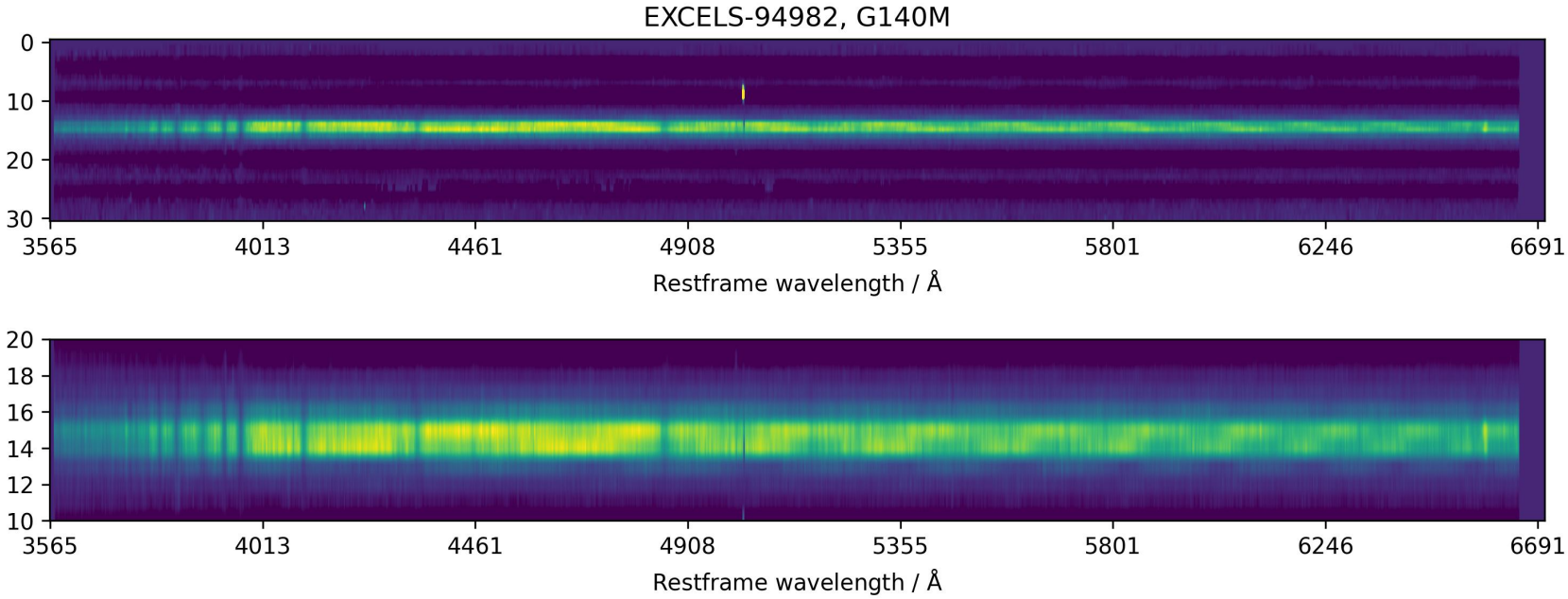

Figure 4.1: Example of a 2D spectrum from the EXCELS survey (EXCELS-94982 at $z = 1.8$), taken using the G140M grating. *Top*: the full 2D spectrum. *Bottom*: zoom in on the centre of the 2D spectrum. The data were reduced using the JWST level 1 and level 2 pipelines, with sky and artefact subtraction performed manually using custom code. The spectrum shows systematic noise, which is especially clear at rest-frame wavelengths of $\lambda > 5000$Å (see Section 4.2).

4.2.1 Sample selection

To select PSBs from the EXCELS catalogue, we require an EXCELS type of either: (i) PRIMER non-robust passive, (ii) VANDELS non-robust passive, (iii) PRIMER robust passive or (iv) VANDELS robust passive, as determined from the EXCELS observation classes (see Section 4.2). We then select our initial sample using cuts on the equivalent width of the Hδ (λ4102Å) line, $W_{H\delta}$. We follow the non-parametric method of Goto et al. (2003), by shifting the spectra to the rest-frame, and calculating $W_{H\delta}$ using:

$$W_{H\delta} = \int_{4082\,\text{Å}}^{4122\,\text{Å}} \frac{1 - F(\lambda)}{F_c(\lambda)}\, d\lambda, \tag{4.1}$$

where $F(\lambda)$ is the spectral fux, and $F_c(\lambda)$ is the continuum flux. $F_c(\lambda)$ is estimated using a linear interpolation across the line region, using continuum points determined from the wavelength intervals 4030 - 4082 and 4122 - 4170Å, as these intervals are free from significant absorption and emission lines. We select PSBs with the commonly used criteria of $W_{H\delta} > 5$Å (e.g., Balogh et al., 1999; Goto, 2007; Maltby et al., 2016) – this results in a initial sample of 20 galaxies.

We then remove a further four galaxies from the sample with no coverage of both the Mg II ($\lambda\lambda$2796, 2803Å) and Na D ($\lambda\lambda$5890, 5896Å) lines. The lack of coverage is due to the features falling partially or completely within detector gaps. To allow accurate fitting to the absorption profiles, we select PSB galaxies with mean signal-to-noise ratios per resolution element of $S/N_{Na\,D} \geq 15$, using a wavelength interval encompassing the Na D profile (5800 - 6000Å). We also determine $S/N_{Mg\,II}$, using the mean signal-to-noise ratio over the wavelength interval 2700 - 2900Å, however we do not place a cut on this value. This results in a final sample of 9 galaxies (see Table 4.1). The combined 1D spectra of our final sample of 9 post-starbursts are shown in Figures 4.2, 4.3 and 4.4. The spectra have been smoothed using a Gaussian filter with σ = 1Å for display purposes only.

In this work, we avoid placing a cut on the equivalent width of the [O II] emission line, as some post-starburst selections use (e.g., Tran et al., 2003). We choose not to use this selection criteria, as it may bias against PSBs hosting AGN (Yan et al., 2006). However, we note that using a conservative cut of $W_{[O\,II]} > -5$Å would result in 2/9 galaxies being removed from the sample (EXCELS-34495 and EXCELS-127460, both

Table 4.1: Post-starburst galaxies selected from the EXCELS catalogue. Columns are: (1) EXCELS ID, (2) spectroscopic redshift, (3) Hδ equivalent width in units of Å, (4) [O II] equivalent width in units of Å, (5) average signal-to-noise over the Mg II feature, (6) average signal-to-noise over the Na D feature and (7) object classifications from a PCA analysis (based on the method of Wild et al., 2014) of the PRIMER-UDS photometric catalogue.

EXCELS ID	$z_{\rm spec}$	$W_{H\delta_w}$ (Å)	$W_{[O\,II]}$ (Å)	$S/N_{Mg\,II}$	$S/N_{Na\,D}$	PCA Class
34495	3.80	8.9	-5.3	3.6	21.2	PSB
39063	3.70	8.8	–	4.5	22.6	PSB
50789	3.99	11.5	2.0	2.5	22.5	PSB
52467	3.24	13.4	–	2.3	20.5	PSB
57000	3.19	11.0	-3.9	1.3	17.7	PSB
65915	4.36	8.2	-0.6	–	18.3	Undefined
94982	1.83	6.3	-0.3	–	32.6	PSB
113667	3.97	8.8	0.1	3.6	20.9	Star-forming
127460	2.53	7.4	-5.3	–	30.8	PSB

with $W_{[O\,II]}$ = -5.3Å). We cross match our sample with the Chandra X-UDS survey catalogue (Kocevski et al., 2018), and find one galaxy, EXCELS-34495 in our sample is securely X-ray detected, indicating the presence of an AGN (see the top panel of Figure 4.2 for the 1D spectrum of this galaxy).

We compare our spectral classifications to classifications generated from a preliminary principal component analysis (PCA) undertaken on the PRIMER photometric catalogue (de Lisle et al., in prep)[1] – we find 7/9 of our sample are classed as PSBs, with one galaxy (EXCELS-113667) classed as star-forming, and one galaxy (EXCELS-65915) with an undefined class.

4.3 Stacking Analysis

To build on our previous work (see Chapter 3), we first undertake a stacking analysis of the Mg II ($\lambda\lambda$2796, 2803Å) profile, which is a sensitive tracer of the low ionisation interstellar medium (ISM). We then repeat this process for the Na D ($\lambda\lambda$5890, 5896Å)

[1]The PCA methodology follows that of Wild et al. (2014, 2016) and Wilkinson et al. (2021) - undertaken on the UDS DR8 and DR11 catalogues - applied to the PRIMER photometric catalogue. For more details, see Section 2.2.2.

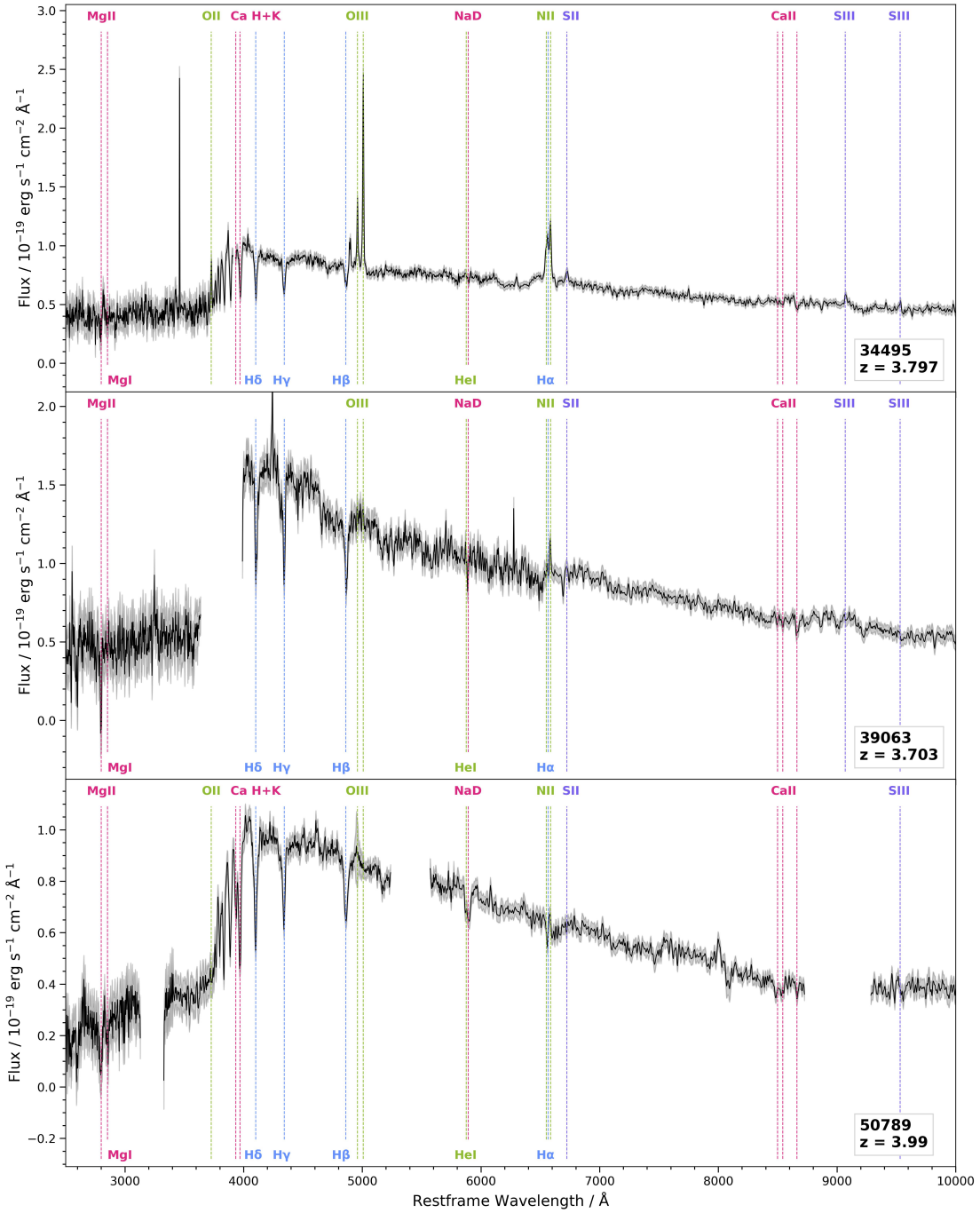

Figure 4.2: Combined 1D spectra for EXCELS-34495 (*top*), EXCELS-39063 (*middle*) and EXCELS-50789 (*bottom*). The spectra have been shifted to rest-frame wavelength using the $z_{\rm spec}$ values determined for each object. Key spectral features are denoted by vertical dashed lines. The spectra have been smoothed using a Gaussian filter with σ = 1Å for display purposes only.

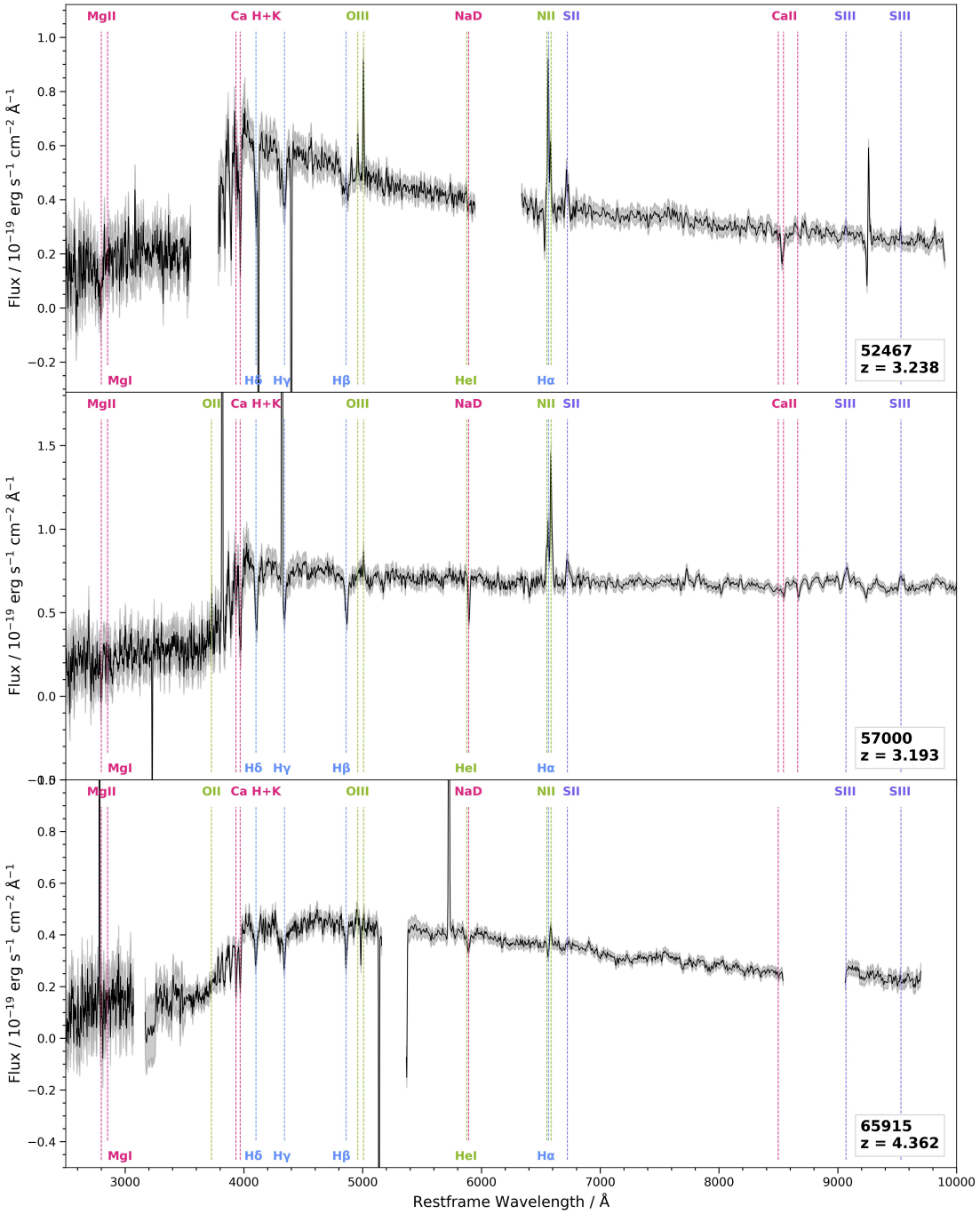

Figure 4.3: Combined 1D spectra for EXCELS-52467 (*top*), EXCELS-57000 (*middle*) and EXCELS-65915 (*bottom*). The spectra have been shifted to rest-frame wavelength using the $z_{\rm spec}$ values determined for each object. Key spectral features are denoted by vertical dashed lines. The spectra have been smoothed using a Gaussian filter with σ = 1Å for display purposes only.

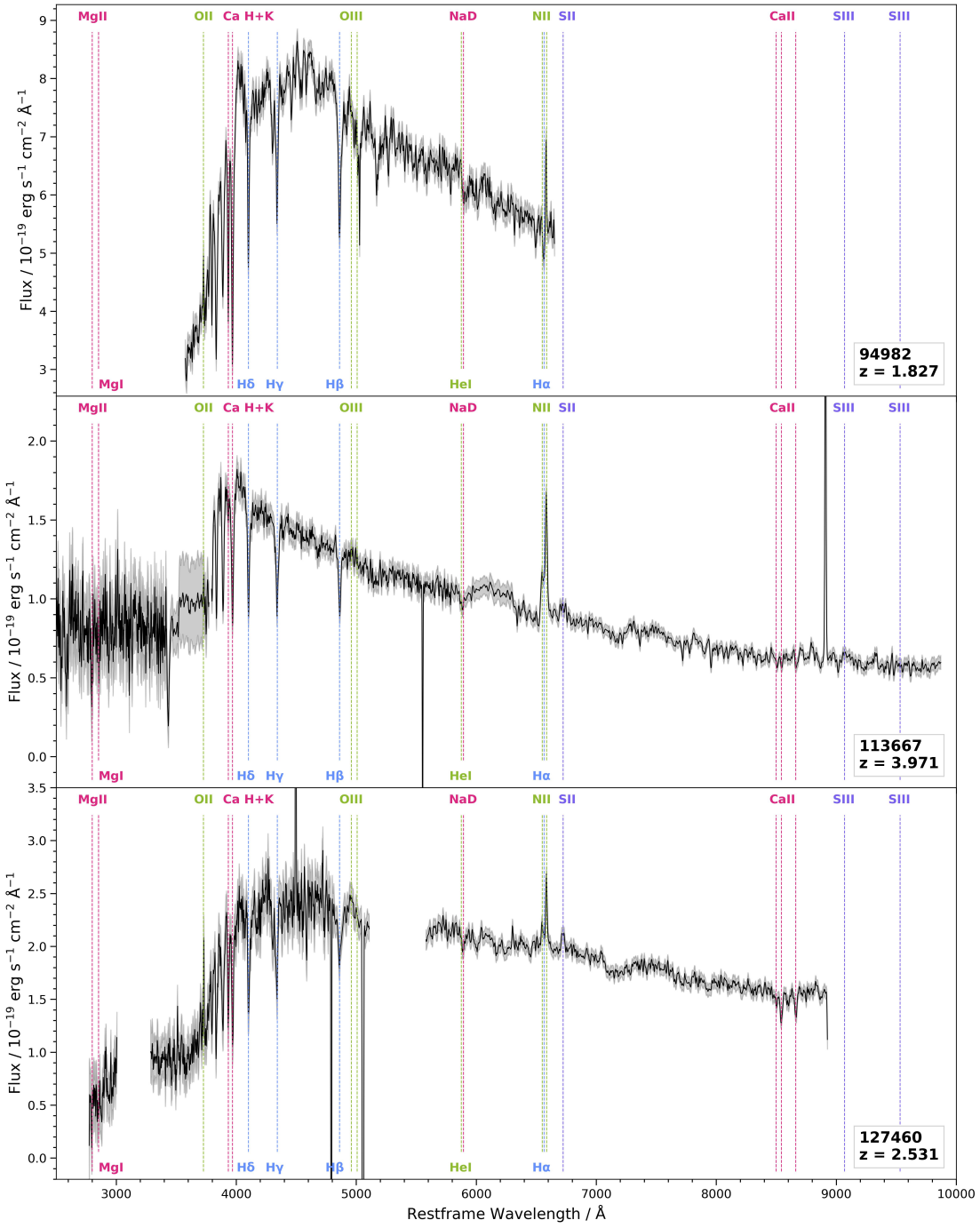

Figure 4.4: Combined 1D spectra for EXCELS-94982 (*top*), EXCELS-113667 (*middle*) and EXCELS-127460 (*bottom*). The spectra have been shifted to rest-frame wavelength using the $z_{\rm spec}$ values determined for each object. Key spectral features are denoted by vertical dashed lines. The spectra have been smoothed using a Gaussian filter with σ = 1Å for display purposes only.

feature, as these sodium lines are ideal for tracing neutral gas contained within an outflow (e.g. Veilleux et al., 2020). In this section, we outline the stacking procedure and modelling of the two absorption profiles, and compare our estimated outflow velocities.

4.3.1 Stacking Procedure

Our stacking procedure is similar to that outlined in section 3.2.4, however we undertake two slightly different procedures for the Mg II and Na D stacks.

Mg II. Seven of the galaxies within our sample have full coverage of the Mg II absorption profile, however we exclude EXCELS-65915 from Mg II analysis due to the presence of a large noise spike at λ = 2785 Å, as this would affect the accurate modelling of any significant blue-shifted absorption within this galaxy. Recall that our post-starburst sample was selected using a cut on the mean signal-to-noise ratio over the Na D profile, with no cut on the signal-to-noise of the Mg II feature. The six remaining galaxies in our Mg II sample have an average $S/N_{Mg\,II}$ of ~ 3 per pixel (1 pixel $\sim$ 1.3 Å). To create our composite spectrum, we first shift all individual input spectra to their rest-frame wavelengths using their spectroscopic redshifts. The spectra are resampled onto the same wavelength axis ($\Delta\lambda$ = 1Å), with any significant noise spikes (which do not fall in features of interest) and detector gaps masked out. Each spectrum is normalised for the total flux over $2700 \leq \lambda \leq 2900$Å with the Mg II profile masked out. The spectra are combined to create a single, median stack.

Na D. All nine galaxies in our sample have sufficient coverage for use within our composite spectrum. We again shift all individual input spectra to their rest-frame wavelengths, and resample onto the same wavelength axis ($\Delta\lambda$ = 1Å). Each spectrum is normalised for the total flux over $5450 \leq \lambda \leq 5550$Å, as this region of the continuum is free from significant absorption and emission lines (Chen et al., 2010). The spectra are combined to create a single, median stack.

Uncertainties in both stacks are the mean of the standard error from 100 bootstrapped simulated stacks.

4.3.2 Modelling the Absorption Profiles

In order to identify any outflow signatures, we fit the absorption features of each stack with a stellar component, then fit a double Gaussian decomposition model to the residual flux after the stellar model is removed.

To model the stellar contribution to each stacked spectrum, we use the Penalized PiXel-Fitting (`pPXF`, Cappellari & Emsellem, 2004; Cappellari, 2017, 2023) software, using the E-MILES stellar population synthesis models (Vazdekis et al., 2016). The E-MILES library is a theoretical set of models, covering the wavelength range λλ1680 - 50,000Å and a wide range of metallicities and temperatures. We restrict the library to models with solar metallicity, as expected for high-z galaxies (Sommariva et al., 2012). The fits are performed over the wavelength range 2500 - 7350Å. We mask several spectral lines during the fit which may affect the stellar modelling, including prominent Balmer lines, [O II] λλ3727, 3730, [O III] λλ4959, 5007, He I λ5875, [N II] λλ6548, 6584 and [S II] λλ6717, 6731, as well as the Mg II and Na D profiles. To remove the stellar component, we divide the stacked spectrum by the best-fitting model output by `pPXF`.

4.3.2.1 Mg II Gaussian Model

The double Gaussian decomposition model for the Mg II profile follows the approach used in Section 3.3.1. We estimate any spectral broadening of the absorption feature by fitting a single Gaussian doublet ($G_{initial}$) to the Mg II profile, with the centroids fixed at the rest-frame wavelengths for systemic absorption. The doublet intensity ratio is set as 1.2:1, as seen for high-z galaxies in Weiner et al. (2009). We fit $G_{initial}$ to the red side of the absorption feature only ($\lambda \geq 2803$Å). We then fit the full profile using two Gaussian doublets, modelling the systemic absorption (stellar + ISM, G_{sys}) and the outflow (G_{out}) separately. The centroid of G_{sys} is fixed at the rest-frame wavelength, while the amplitude is allowed to vary. The centroid and amplitude of G_{out} are left free. The width of both doublets is fixed at the value determined by $G_{initial}$.

4.3.2.2 Na D Gaussian Model

We model the residual Na D (λλ 5890, 5896Å) profile in a similar way to the Mg II profile. We first estimate any spectral broadening by fitting a single Gaussian doublet (G_{init}) to the red side of the absorption feature, using the form:

$$G = r_1 \exp\left(-\frac{(x-\mu_1)^2}{2\sigma^2}\right) + r_2 \exp\left(-\frac{(x-\mu_2)^2}{2\sigma^2}\right). \quad (4.2)$$

Here, $\mu_1 = 5890$Å, $\mu_2 = 5896$Å and r_2/r_1 is the ratio of the 5896:5890 lines, fixed at 2:1 – this line ratio is suitable for optically thin gas (Draine, 2011), and we find that allowing r_2/r_1 to vary does not significantly affect our results. We then fit the Na D profile with a two component model, using two Gaussian doublets. The first component (G_{ISM}) models the systemic absorption (ISM) and the second component (G_{out}) models the outflow. The centroid of G_{ISM} is fixed at the rest-frame wavelength, while the amplitude is allowed to vary. The centroid and amplitude of G_{out} are left free. The width, σ, of both doublets is fixed at the value determined by $G_{initial}$. Comparison of the centroids of the two components provides a wavelength offset, Δλ, which can be used to estimate the velocity offset of the outflowing gas, Δv. 100 simulated median stacks are generated via a bootstrap analysis, and the fitting routine is repeated on each stack. The uncertainty in Δλ is the 1σ error of the resulting 100 velocity measurements. The significance of the outflowing component for each fit is evaluated using an F-test, which produces a p-value – the necessity of an outflowing component is rejected if $p > 0.05$.

4.3.3 Results and Discussion

The best-fitting models for our Mg II and Na D stacks are shown in Figure 4.5 and Figure 4.6 respectively. The top panels show the best-fitting `pPXF` model to the stacked spectra, while the bottom left panels show a zoom in of the relevant absorption feature. The bottom centre panels show the best-fitting double Gaussian models after removal of the `pPXF` fit, and the bottom right panels show the combined stellar and double Gaussian model fit to the absorption profiles. The outflow components for both fits were deemed significant by an F-test ($p < 0.05$). We stress that our derived $v_{Na\,D}$ values below are to be interpreted with caution, due to the noise within the 2D spectra at rest-frame

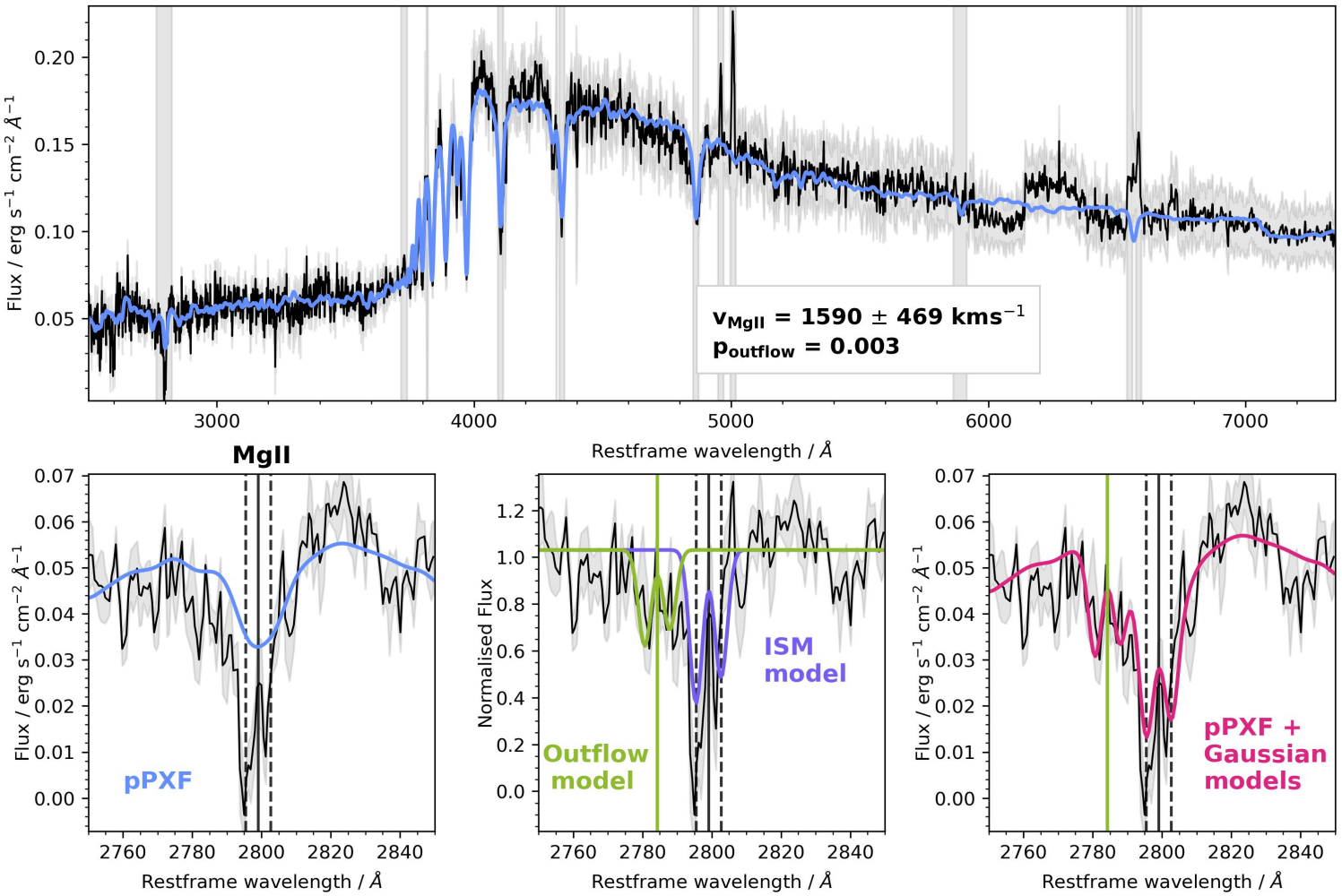

Figure 4.5: The best-fitting pPXF and double Gaussian model to the Mg II profile of our median stack (black, all panels). The stack consists of six galaxies with coverage of the Mg II absorption feature. Light grey shaded areas denote errors in the stack, calculated from a bootstrap analysis of 100 simulated median stacks. Dashed vertical lines in the bottom panels denote the Mg II λλ2795, 2803Å lines. Solid vertical lines denote the centroid of the Mg II profile. *Top*: best-fitting pPXF model (blue) of the stellar component of the spectrum. Vertical light grey shaded regions spanning the entire figure denote spectral features which are masked during the pPXF fitting process. *Bottom left*: zoom in of the Mg II profile and the best-fitting pPXF model (blue). *Bottom centre*: best-fitting double Gaussian model to the residual flux after removal of the stellar model. The full Gaussian model is comprised of a systemic ISM component (purple) and an outflowing component (green). The green vertical line denotes the centroid of the outflowing component. *Bottom right*: The full model (magenta), comprised of the double Gaussian and pPXF fits. The population shows a velocity offset $v_{Mg\,II} \sim 1600$ kms^{-1}.

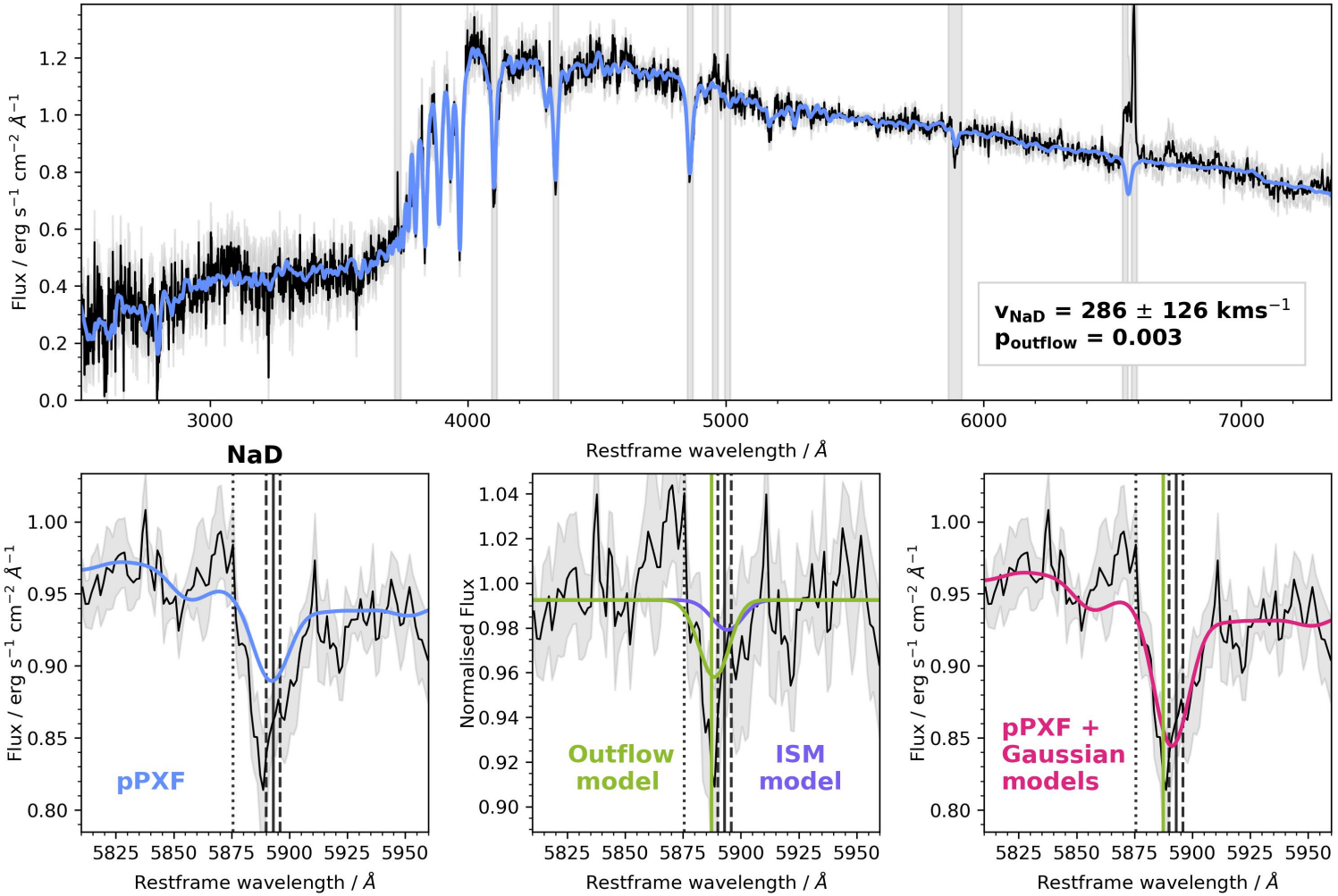

Figure 4.6: The best-fitting pPXF and double Gaussian model to the Na D profile of our median stack (black, all panels). The stack consists of all nine galaxies within the sample. Light grey shaded areas denote errors in the stack, calculated from a bootstrap analysis of 100 simulated median stacks. Dashed black vertical lines in the bottom panels denote the Na D λλ5890, 5896Å lines, solid black vertical lines denotes the centroid of the Na D profile, and dotted black vertical lines denote the He I λ5875Å line. Colours are as presented in Figure 4.5. *Bottom panels*: zoom in of the Na D profile and relevant fits. The population shows a velocity offset of $v_{Na\,D} \sim 290$ kms^{-1}.

wavelengths of $\lambda > 5000$Å, and will become more well constrained following a more robust re-reduction of the data.

We find clear evidence for a strongly blue-shifted component within the Mg II feature, with a corresponding velocity offset of $v_{\mathrm{Mg\,II}} \sim 1600 \pm 470$ kms^{-1}. This is in agreement with larger population studies at $1 \leq z \leq 2$ (see, e.g., Chapter 3, Maltby et al., 2019), where composite spectra of PSBs are found to have $\Delta v \sim 1000$ kms^{-1}. At higher redshifts ($z \sim 3$), Man et al. (2021) detected ~ 1500 kms^{-1} outflows in two gravitationally lensed recently-quenched galaxies – this is in good agreement with the Δv value found in this work, indicating that high-velocity outflows may be common in PSBs from redshifts as high as $z \sim 4$, to present day.

The best-fitting model to our Na D feature results in a velocity offset of $v_{\mathrm{Na\,D}} \sim 290 \pm 130$ kms^{-1}. The absorption profile is reasonably well explained by the `pPXF` stellar model, with only a small amount of residual flux remaining. Similar outflow velocities derived from Na D absorption features, at similar redshifts to our sample, have also been reported in the works of Belli et al. (2023) and Baron et al. (2022). At $z \sim 2.5$, Belli et al. (2023) found a velocity offset of ~ 200 kms^{-1} in a massive galaxy experiencing rapid quenching, which they attribute to an AGN based on the presence of ionised emission lines in the galaxy spectrum. In a study of 144 PSBs at $0 < z < 3$, Baron et al. (2022) found 40% of their sample had detectable outflows, with a median velocity offset of $\Delta v \sim 660$ kms^{-1}. This is higher than our derived velocity value, however, their sample of PSBs was specifically selected to host AGN, which are likely to cause higher velocity outflows than the winds resulting from star formation alone. Locally, Sun et al. (2024) studied the individual Na D profiles of ~ 500 local PSBs, at $z < 0.325$. The authors found ~ 65% of their PSB sample had detectable outflows, with a mean outflow velocity value of $\Delta v \sim 70$ kms^{-1}. This is marginally lower than our derived $v_{\mathrm{Na\,D}}$ value from the stack, however the Sun et al. work selected against PSBs hosting AGN in their sample, while our sample has not. Therefore, our $v_{\mathrm{Na\,D}}$ value is likely a good representation of a mixed population of PSBs at high redshift.

To allow a fair comparison of our $v_{\mathrm{Mg\,II}}$ and $v_{\mathrm{Na\,D}}$ values, we perform the same Na D stacking analysis using only the six galaxies in our Mg II sample, and find the same $v_{\mathrm{Na\,D}}$ velocity offset of ~ 290 kms^{-1}. Whilst Na D and Mg II are both used as tracers of the ISM, they may trace slightly different phases of the ISM. The lower ionisation potential of Na D (5.1eV) compared to Mg II (15.0eV), means the sodium absorption profile may

exhibit lower outflow velocities, as sodium will primarily trace cooler (~ 100 - 1000 K), neutral gas, whilst magnesium primarily traces warmer (~ 10^4 K), low-ionisation gas (Veilleux et al., 2020; Davis et al., 2023). Martin & Bouché (2009) found higher velocity gas sometimes escapes detection in Na D, where a decrease in covering fraction with increasing velocity suppresses the absorption features of the highest speed winds. Part of the discrepancy between our $v_{\mathrm{Mg\,II}}$ and $v_{\mathrm{Na\,D}}$ values may well be due to the continuum flux uncertainties at $\lambda > 5000$Å, as mentioned previously, however this is unlikely to explain the order of magnitude difference.

4.3.3.1 Mass Outflow Rates

From our best-fitting line profiles, we can roughly estimate the median mass outflow rate of the population. To do this, we first estimate the column densities of Mg II and Na D. We use the fit to the Na D stack containing only the six galaxies in our Mg II sample, for a fair comparison. Following Draine (2011) and Zhu et al. (2014), a lower limit on the column density of a metal, N(X), can be derived from the equivalent width of the fitted outflow profile, W_X, using:

$$N(X) = 1.13 \times 10^{20} \left(\frac{W_X}{f_{\mathrm{osc}}\, \lambda^2_{\mathrm{rest}}} \right) \ \mathrm{cm}^{-2}. \tag{4.3}$$

Here, f_{osc} and λ_{rest} are the oscillator strength and the rest-frame wavelength of the transition, respectively. Equation 4.3 assumes that the absorbing gas is optically thin; it is important to note that, during our fitting of the sodium profile (Section 4.3.2.2), we have already made the assumption of an optically thin gas by using a line ratio of 1:2. Thus, the sodium column density N(Na D) is likely to be higher, resulting in a underestimate for any mass outflow rates estimated. During our magnesium fitting routine (Section 4.3.2.1), we assume the lines are close to saturation, following Weiner et al. (2009), which will also lead to an underestimate in the N(Mg II) derived using Equation 4.3. For magnesium, we adopt $f_{\mathrm{MgII}} = 0.306$ and $\lambda_{\mathrm{MgII}} = 2803$Å, and for sodium we adopt $f_{\mathrm{NaD}} = 0.318$ and $\lambda_{\mathrm{NaD}} = 5897$Å (Draine, 2011). Using our best-fitting outflow profiles, we find column densities of N(Mg II) ~ 8.6×10^{13} cm^{-2} and N(Na D) ~ 3.9×10^{12} cm^{-2}.

The column density of hydrogen, N(H), can then be estimated from N(X), using:

$$\mathrm{N(H)} = \frac{\mathrm{N(X)}}{\chi(\mathrm{X})\, 10^{\log(\mathrm{X/H})}\, 10^{d(\mathrm{X})}} \ \mathrm{cm}^{-2}, \tag{4.4}$$

where χ(X) is the metal ionisation fraction, log(X/H) is the metal abundance relative to H, and d(X) is the level of dust depletion (Rupke et al., 2005a,b; Veilleux et al., 2020). For magnesium, we adopt the values used in Perrotta et al. (2023), of χ(Mg II) = 0.7, log(Mg II/H) = -4.45 and d(Mg II) = -0.5. For sodium, we adopt the values used in Belli et al. (2023), of χ(Na D) = 0.1, log(Na D) = -5.69 and d(Na D) = -0.95. Our hydrogen column densities are then $\mathrm{N(H)_{MgII}} \sim 1.1 \times 10^{19}$ cm^{-2} and $\mathrm{N(H)_{NaD}} \sim 1.6 \times 10^{20}$ cm^{-2}.

The mass outflow rate for a shell geometry can be written as:

$$\dot{M}_{\mathrm{out}} = 1.4\, m_p\, \Omega\, \mathrm{N(H)}\, \mathrm{R_{out}}\, \mathrm{v_{out}} \ \ \mathrm{M_\odot\, yr^{-1}}, \tag{4.5}$$

where m_p is the proton mass, Ω is the solid angle subtended by the outflow, $\mathrm{R_{out}}$ is the outflow radius, and $\mathrm{v_{out}}$ is the outflow velocity. Following Belli et al. (2023), we adopt $\Omega/4\pi$ = 0.4, assuming an opening angle of 40% of the solid sphere. The spatial extent of the Mg II and Na D outflows are unknown, however previous studies have found Mg II outflows to extend to a maximum of ~ a few kpc (see Veilleux et al., 2020). Na D outflows have been found to originate on spatial scales of $\lesssim$ 10 kpc (e.g. Roberts-Borsani et al., 2020; Baron et al., 2022), and recent spatially resolved work at cosmic noon has found sodium outflows at $\lesssim$ 1 kpc (Veilleux et al., 2023) and ~ 2.7 kpc (D'Eugenio et al., 2023). Studies of galaxy sizes at cosmic noon have found post-starbursts to be extremely compact, with effective radii $\mathrm{R_e} \sim 1$ kpc (e.g. Almaini et al., 2017). Therefore, we adopt an outflow radius of $\mathrm{R_{out}}$ = 1 kpc. Taking $\mathrm{v_{out}}$ as the estimated velocity values from our fits, we find $\dot{M}_{\mathrm{out,\,MgII}} \sim 1\ \mathrm{M_\odot yr^{-1}}$ and $\dot{M}_{\mathrm{out,\,NaD}} \sim 3\ \mathrm{M_\odot yr^{-1}}$. We stress again that the derived mass outflow rates are very uncertain due to spectral uncertainties.

The mass outflow rate of the cool, neutral gas, estimated from the sodium profile, is ~ 3 times larger than that of the warm, low-ionisation gas, estimated from magnesium. This has been seen in simulations, where the majority of outflowing mass is predicted to be in the neutral and molecular gas phases (e.g. Kim et al., 2020). In their study of a post-starburst galaxy at $z \sim 3$, D'Eugenio et al. (2023) found neutral mass outflow rates

$\sim 10-100$ times greater than those derived from ionised gas, traced by [O III] emission. It should be noted, however, that [O III] traces much higher ionisation gas than Mg II, and therefore it is not trivial to compare the two. Since the Mg II gas in our stack is very likely saturated, our $\dot{M}_{\mathrm{out,\,MgII}}$ estimate is a lower limit – the two mass outflow rates are likely closer in value.

The EXCELS galaxy spectra, along with the corresponding PRIMER photometry, have undergone preliminary analysis with the `BAGPIPES` spectral fitting code[2] (Carnall et al., 2018, 2019), which allowed estimation of star formation rates. We note that the `BAGPIPES` fits, and any parameters resulting from these fits, are subject to the uncertainty in the 2D spectra, as mentioned previously, so should be interpreted with caution. The average SFR of the six galaxies in our stack is ~ 0.01 $\mathrm{M_{\odot}yr^{-1}}$ – this is $\sim$ 100 times lower than our estimated $\dot{M}_{\mathrm{out,\,MgII}}$, and ~ 300 times lower than our estimated $\dot{M}_{\mathrm{out,\,NaD}}$. The much larger mass outflow rates indicate that the outflows have played, and are possibly still playing, a key role in the quenching of our galaxy sample, via the expulsion of star-forming fuel.

4.4 Individual Objects

The high resolution of JWST allows us, for the first time, to investigate galactic scale winds for individual objects at $z \sim 3$. To do this, we fit the individual absorption profiles using the `LMFIT PYTHON` package, following the method as outlined in Section 4.3.2, using a stellar component modelled by `pPXF` and a Gaussian decomposition model. Errors in the derived velocities are the standard error of the fitted velocity offset, output from `LMFIT`. We intend to undertake a more robust error analysis at a later stage. We stress that the velocity values should be interpreted with caution, due to the need for a re-reduction of the 2D spectra, and the low S/N over the Mg II features. Best-fitting velocity offset values for seven of our nine galaxies are presented in Table 4.2; we exclude EXCELS-94982 and EXCELS-127460 as they have no coverage of the Mg II feature, and we find, on inspection, that the `pPXF` stellar model is poorly fit to the continuum surrounding the Na D feature. Blueshifted and redshifted offsets are defined with positive and negative velocity values, respectively. We discuss the possible causes for this below. The significance of the outflowing component for each fit is again

[2]We refer the reader to Carnall et al. (2024) for details of the fits.

evaluated using an F-test. The p-values for our fits can be found in Table 4.2. We note that we do not attempt to derive mass outflow rates on an individual basis, due to the large uncertainties arising from the fits. Mass outflow rates will be estimated in future work, following a re-reduction of the data.

EXCELS-34495 has best-fitting velocity values of $v_{Mg\,II}$ = 781 ± 38 kms^{-1} and $v_{Na\,D}$ = -128 ± 144 kms^{-1} (Figure 4.7). This object is securely detected in Chandra X-ray observations, and the EXCELS spectrum shows strong [O III] and broad [N II]/Hα lines (Figure 4.2, top panel), all indicative of a galaxy hosting an AGN. The best-fitting $v_{Na\,D}$ value is consistent with zero within the errors, and rejected by an F-test. However, visual inspection indicates that a P-Cygni profile would be a better suited model to both absorption features. P-Cygni profiles show both blueshifted absorption and redshifted emission, caused by re-emission of absorbed photons along the line of sight (Prochaska et al., 2011). The Na D feature may also be affected by emission line infilling from He I λ5875Å. The more complex modelling of P-Cygni profiles, along with the contribution of He I, will be undertaken in future work.

EXCELS-39063 has best-fitting velocity values of $v_{Mg\,II}$ = 156 ± 58 kms^{-1} and $v_{Na\,D}$ = 402 ± 47 kms^{-1} (Figure 4.8).

EXCELS-50789 has a best-fitting velocity value of $v_{Mg\,II}$ = 675 ± 169 kms^{-1} (Figure 4.9, top row). The Mg II feature shows signs of a P-Cygni profile, however the possible redshifted emission seems well modelled by the `pPXF` stellar component. This object also shows incredibly broad Na D absorption (Figure 4.9, bottom row). A preliminary extraction of 1D spectra from different positions along the slit, as well as visual inspection of the Balmer and Ca II lines rules out any rotation as the underlying cause. Thus, we choose to model an additional *inflowing* component (denoted in yellow in Figure 4.9), using the same Gaussian form as in Equation 4.2, with a free centroid. This results in an outflow velocity of $v_{Na\,D,\,out}$ = 1196 ± 62 kms^{-1} and an inflow velocity of $v_{Na\,D,\,in}$ = -575 ± 95 kms^{-1}. Since we don't observe a P-Cygni profile, it is possible that the outflow and inflow are occurring along separate planes of the galaxy. JWST NIRCam PRIMER imaging of this galaxy shows a very close companion object, and future study of structural parameters could quantify if this galaxy is undergoing, or has recently undergone, a merger or close interaction.

EXCELS-52467 has a best-fitting velocity value of $v_{Mg\,II}$ = 1501 ± 73 kms^{-1} (Figure

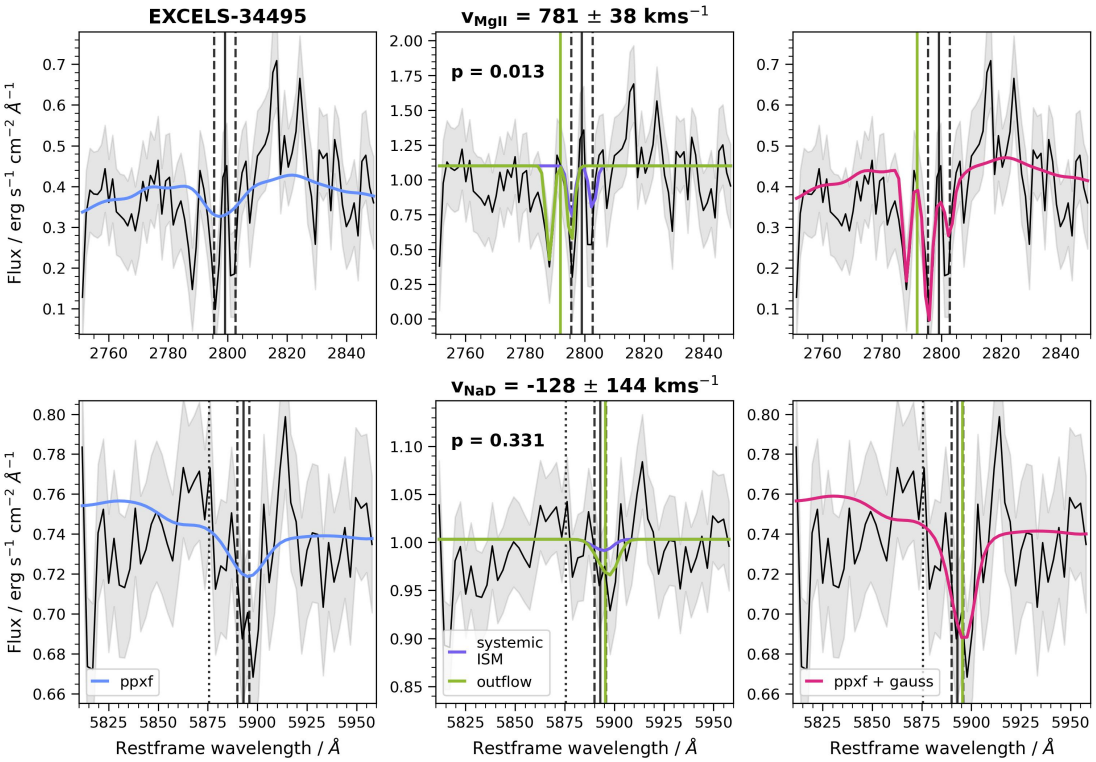

Figure 4.7: Preliminary fits to the Mg II (*top*) and Na D (*bottom*) profiles of EXCELS-34495. Grey shaded areas denote the errors in the spectral flux, as determined from the JWST pipeline. Solid and dashed vertical black lines denote the rest-frame wavelengths of the centroid and individual lines of the profiles, respectively. An additional dotted black vertical line in the bottom row denotes the rest-frame wavelength of the He I line. The left panels show the `pPXF` stellar model (blue) to the profiles. Centre panels show the Guassian decomposition fits to the residual flux, consisting of an ISM component at rest-frame wavelength (purple) and an outflowing component (green). Solid green vertical lines denote the centroid of the outflowing component. The right panels show the combined ppxf and Gaussian model (magenta). The best-fitting velocity offsets are $v_{Mg\,II} \sim 780$ and $v_{Na\,D} \sim -130$ kms^{-1} for Mg II and Na D, respectively, however the Na D outflowing component is rejected by an F-test. Both profiles in this galaxy show some evidence for a P-Cygni profile, which will be modelled in future work.

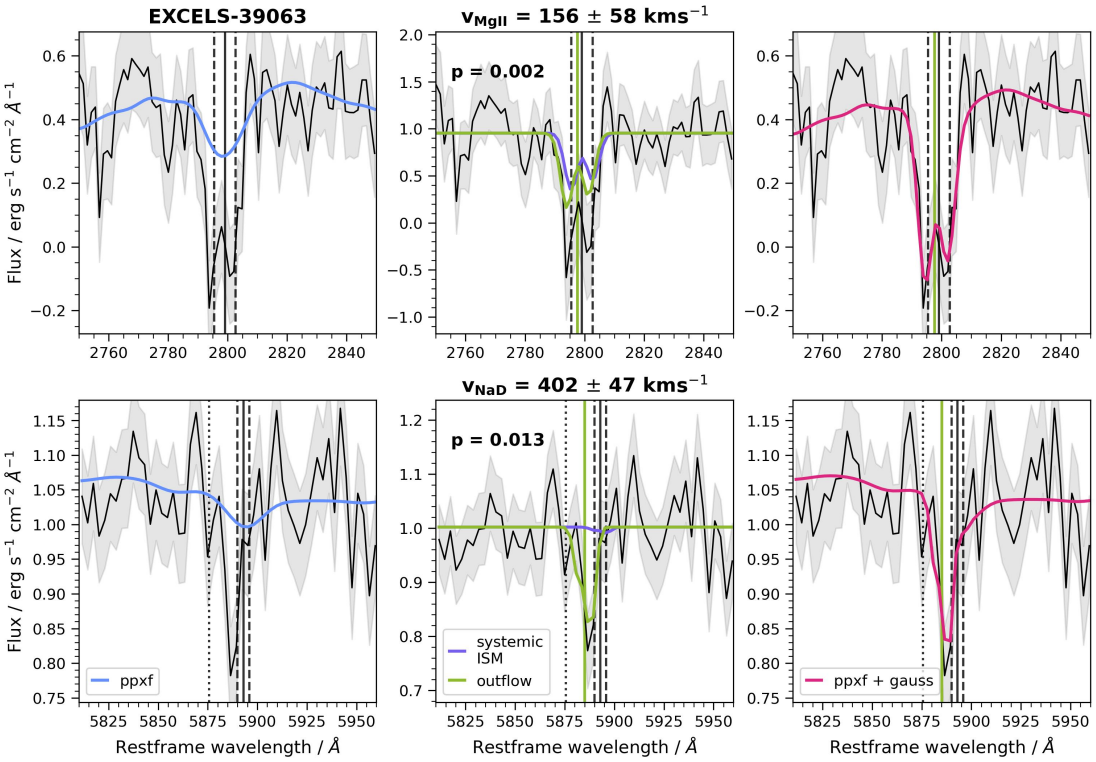

Figure 4.8: Preliminary fits to the Mg II (*top*) and Na D (*bottom*) profiles of EXCELS-39063. Panels and colours are as presented in Figure 4.8. The best-fitting velocity offsets are $v_{\mathrm{Mg\,II}} \sim 160$ and $v_{\mathrm{Na\,D}} \sim 400$ kms^{-1} for Mg II and Na D, respectively.

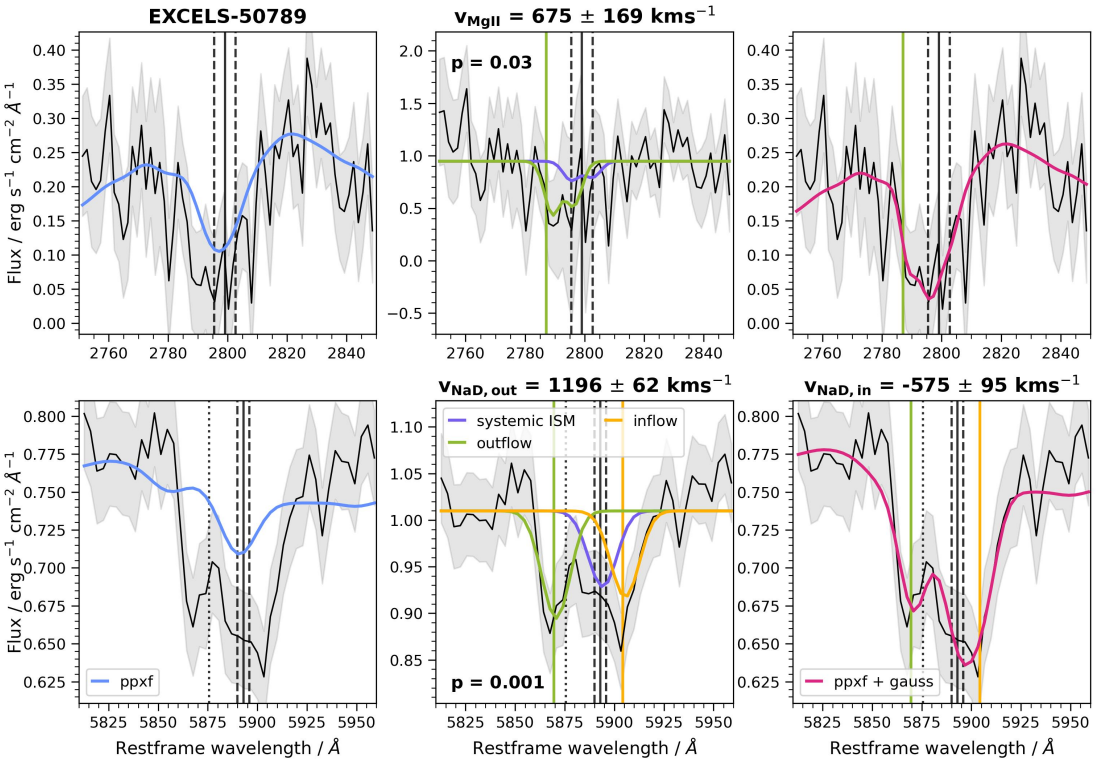

Figure 4.9: Preliminary fits to the Mg II (*top*) and Na D (*bottom*) profiles of EXCELS-50789. Panels and colours are as presented in Figure 4.8. We also model an additional, inflowing component for the Na D profile, shown in yellow, with the centroid wavelength denoted by the vertical yellow line. The best-fitting velocity offsets are $v_{Mg\,II} \sim 680$ kms^{-1} for the Mg II profile, and $v_{Na\,D,out} \sim 1200$ and $v_{Na\,D,in} \sim$ -580 kms^{-1} for the outflowing and inflowing components of the Na D model, respectively.

Table 4.2: Preliminary velocity offset values derived from fits to individual galaxy spectra within the sample. The significance of the outflowing component for each fit is evaluated using an F-test, which produces a p_F-value – the necessity of an outflowing component is rejected if $p_F > 0.05$. The 'Notes' column provides brief additional details for specific objects, if relevant. We exclude EXCELS-94982 and EXCELS-127460 as they have no coverage of the Mg II feature, and the `pPXF` stellar model is poorly fit to the continuum surrounding the Na D feature.

EXCELS ID	z_{spec}	Mg II		Na D		Notes
		$v_{Mg\,II}$ (kms^{-1})	p_F	$v_{Na\,D}$ (kms^{-1})	p_F	
34495	3.80	781 ± 38	0.013	-128 ± 144	0.331	Na D outflowing component rejected by F-test
39063	3.70	156 ± 58	0.002	402 ± 47	0.013	–
50789	3.99	675 ± 169	0.030	v_{out}: 1196 ± 62 v_{in}: -575 ± 95	0.001	Modelled additional inflowing component
52467	3.24	1501 ± 73	0.021	–	–	–
57000	3.19	-312 ± 313	0.177	-53 ± 27	0.001	Mg II outflowing component rejected by F-test
65915	4.36	–	–	382 ± 221	0.015	–
113667	3.97	1290 ± 70	0.087	v_1: 1386 ± 85 v_2: 520 ± 88	0.006	Modelled additional outflowing component Mg II outflowing component rejected by F-test

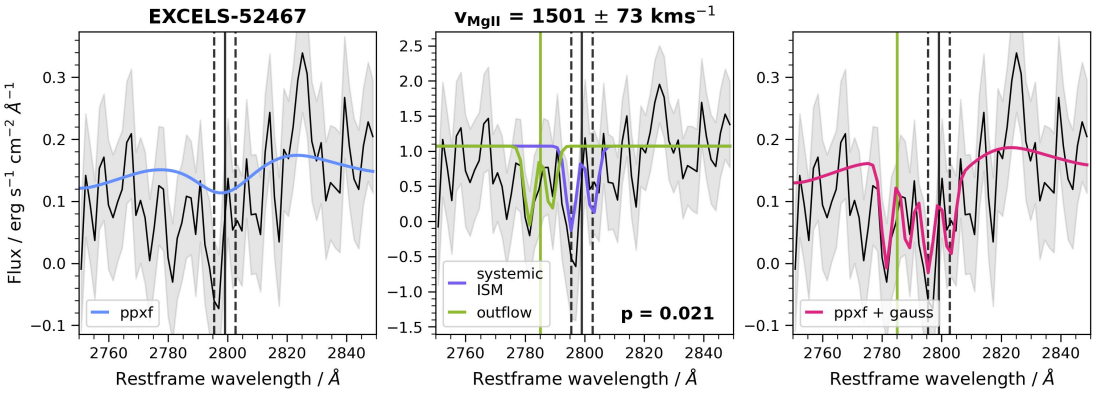

Figure 4.10: Preliminary fit to the Mg II profile of EXCELS-52467. Panels and colours are as presented in Figure 4.8. The best-fitting velocity offset is $v_{Mg\,II} \sim 1500$ kms^{-1} for Mg II. A formal fit to the Na D profile was not attempted, due to the detector gap just redward of the sodium feature

4.10). The Mg II feature shows signs of a P-Cygni profile, which we will model in future work. A fit to the Na D profile was attempted, however the stellar component from `pPXF` does not fit the continuum surrounding the feature well. This is likely due to the detector gap just redward of the sodium feature (see Figure 4.3, row 1).

EXCELS-57000 has best-fitting velocity values of $v_{Mg\,II}$ = -312 ± 313 kms^{-1} and $v_{Na\,D}$ = -53 ± 27 kms^{-1} (Figure 4.11). The absorption profiles show marginal evidence for redshifted absorption, indicative of galactic inflows, however the best-fit values are close to systemic velocity within the errors, and the Mg II outflowing component is rejected by an F-test.

EXCELS-65915 has a best-fitting velocity value of $v_{Na\,D}$ = 382 ± 221 kms^{-1} (Figure 4.12).

EXCELS-94982 does not have a formal best-fitting velocity value. The continuum surrounding the Na D profile is not well fit by `pPXF`, due to the noise effects seen in the 2D spectrum (Figure 4.1). A preliminary fit indicates in an *inflowing* galactic wind, with velocity $v_{Na\,D} \sim$ -1200 kms^{-1}. However, the sinusoidal shape of the continuum is strongest around the Na D profile, and we believe our Guassian fit is locking into a non-physical drop in flux redward of the sodium lines. Therefore, we will re-model the Na *D* profile of this galaxy post a re-reduction of the data.

EXCELS-113667 has a best-fitting velocity value of $v_{Mg\,II}$ = 1290 ± 70 kms^{-1} (Figure

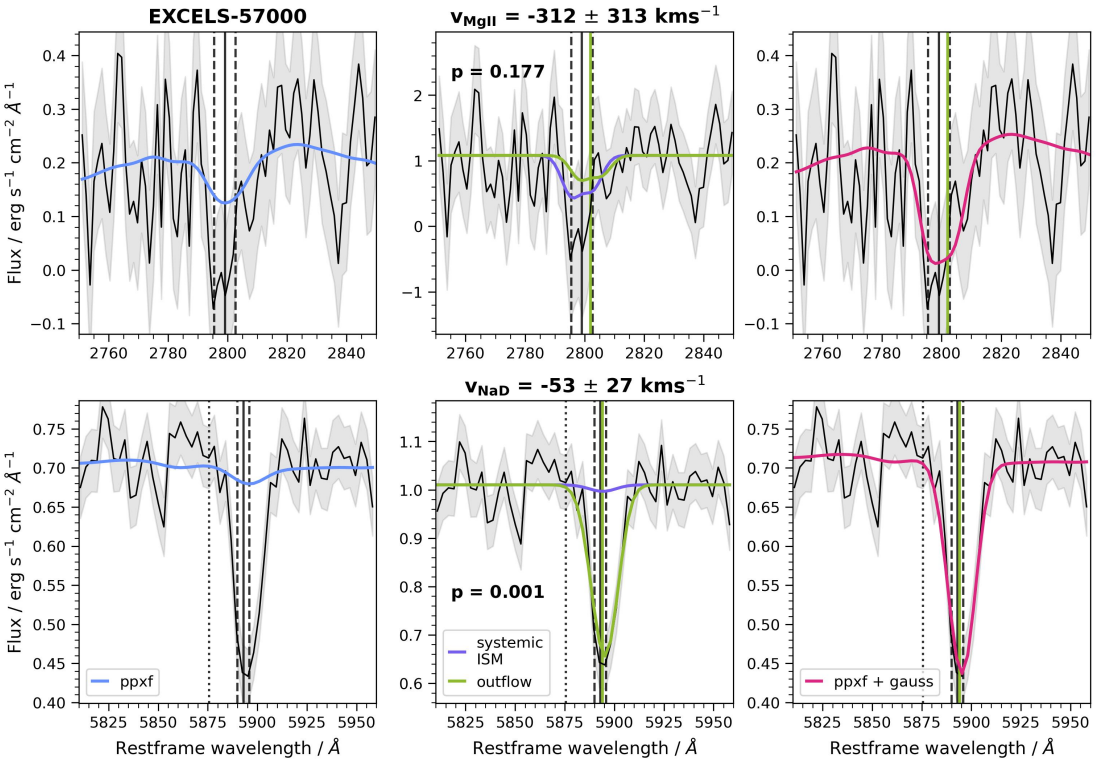

Figure 4.11: Preliminary fits to the Mg II (*top*) and Na D (*bottom*) profiles of EXCELS-57000. Panels and colours are as presented in Figure 4.8. The best-fitting velocity offsets are $v_{Mg\,II}$ ~ -310 and $v_{Na\,D}$ ~ -50 kms^{-1} for Mg II and Na D, respectively. The profiles show marginal evidence for redshifted absorption, however the Mg II outflowing component is rejected by an F-test

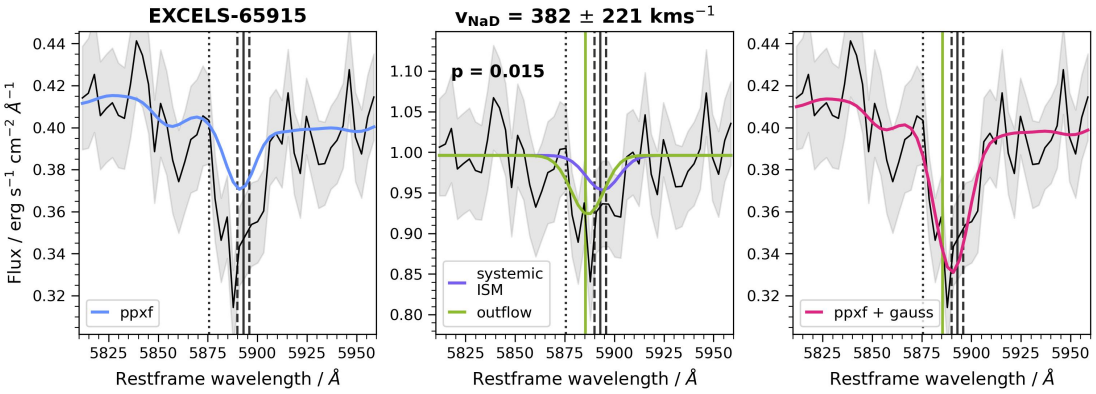

Figure 4.12: Preliminary fit to the Na D profile of EXCELS-65915. Panels and colours are as presented in Figure 4.8. The best-fitting velocity offset is $v_{Na\,D}$ ~ 380 kms^{-1} for Na D.

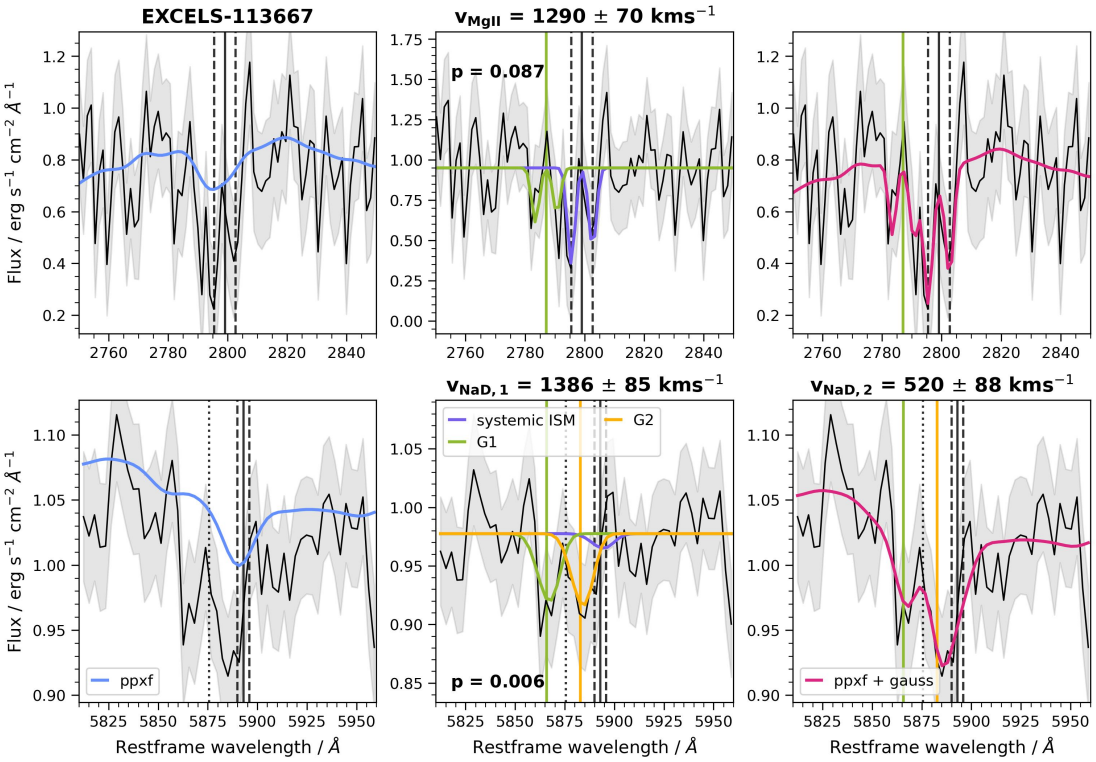

Figure 4.13: Preliminary fits to the Mg II (*top*) and Na D (*bottom*) profiles of EXCELS-113667. Panels and colours are as presented in Figure 4.8. We also model an additional outflowing component for the Na D profile, shown in yellow, with the centroid wavelength denoted by the vertical yellow line. The best-fitting velocity offset is $v_{Mg\,II} \sim 1290$ kms^{-1} for the Mg II profile, however the outflowing component is rejected by an F-test. The best-fitting velocity offsets are $v_{Na\,D,1} \sim 1390$ and $v_{Na\,D,2} \sim 520$ kms^{-1} for the two outflowing components of the Na D model.

4.13, top row), however the continuum is noisy, and the Mg II outflowing component is rejected by an F-test. As with EXCELS-50789, this object also shows broad Na D absorption (Figure 4.13, bottom row), without evidence of an inflow. Thus, we choose to model an additional outflowing component, using the same Gaussian form as in Equation 4.2. This results in two outflow velocities of $v_{Na\,D,\,1} = 1386 \pm 85$ kms^{-1} and $v_{Na\,D,\,2} = 520 \pm 88$ kms^{-1}. Very broad line widths can arise from multiple shells of cool gas travelling at different velocities (Fujita et al., 2009; Chen et al., 2010). There is also evidence for some infilling of the sodium feature from He I emission, which we will model in future work.

EXCELS-127460 does not have a formal best-fitting velocity value, due to the issues as mentioned previously, relating to EXCELS-94982.

4.4.1 Discussion

The preliminary fits indicate that, in our sample of nine galaxies, many post-starburst galaxies host galactic scale outflows, out to redshifts of $z \sim 4.4$. Our derived velocity offsets cover a wide range of values, and the absorption features show a variety of profile shapes.

Considering first the six galaxies in our sample with Mg II coverage, we find 4/6 (67%) have outflowing components deemed significant by an F-test. The best-fitting outflow velocities cover an order of magnitude ($150 \lesssim v_{\mathrm{Mg\,II}} \lesssim 1500$ kms^{-1}). Lower velocity winds ($\Delta v \sim 200$ kms^{-1}) have been detected in post-starburst samples, attributed to 'relic' outflows (e.g Coil et al., 2011, $z < 0.8$), as well as high velocity ($\Delta v \sim 1500$ kms^{-1}) winds at $z \sim 1$ (e.g. Maltby et al., 2019, Chapter 3). Interestingly, the single galaxy in our sample hosting an AGN, EXCELS-34495, is not the object with the highest velocity outflow in Mg II; with $v_{\mathrm{Mg\,II}} \sim 780$ kms^{-1}, EXCELS-34495 has a velocity offset at the sample mean. This is also the case in the work of Davis et al. (2023): the authors found $\sim 40\%$ of their PSB sample, containing some PSBs also hosting AGN, have a maximum outflow velocity of $v_{\mathrm{max}} > 1500$ kms^{-1}. However, the high velocity winds are not attributed to AGN hosting PSBs, which had v_{max} values at, or below, the full sample mean. Davis et al. conclude that the high velocities detected are likely related to compact starbursts, potentially induced by mergers.

Of our nine galaxies, six were judged to have acceptable preliminary fits to the Na D profile, with 5/6 (83%) showing outflowing or inflowing components deemed significant by an F-test. The best-fitting outflow velocities again cover a wide range of values ($380 \lesssim v_{\mathrm{Na\,D}} \lesssim 1400$ kms^{-1}), with two galaxies hosting potential inflowing gas (EXCELS-50789, $v_{\mathrm{Na\,D}} \sim -580$ kms^{-1} and EXCELS-57000, $v_{\mathrm{Na\,D}} \sim -50$ kms^{-1}). When stacking galaxies, inflows are not generally detected, however the study of individual objects has begun to reveal signs of inflowing gas, particularly in older, quiescent galaxies (Rubin, 2017). Recent work studying Na D at low redshift ($z \lesssim 0.3$), by Sun et al. (2024), found the mean velocity offset changed from outflowing to inflowing, as SFR declines ($\Delta v \sim 70$ kms^{-1} in PSBs, to $\Delta v \sim -75$ kms^{-1} in quiescent galaxies). Additionally, Sato et al. (2009) detected Na D inflows within red sequence galaxies at $0.1 < z < 0.5$, and Coil et al. (2011) identified redshifted Mg II absorption in two PSBs, with $-115 \lesssim \Delta v \lesssim -75$ kms^{-1}. The cause of the inflows has been speculated to be gas accretion due to minor mergers or unsettled dust lanes, however the origins are hard to constrain.

4.4.1.1 Future considerations

As discussed previously, the work in this chapter is preliminary, and a number of the 2D spectra show signs of systematic noise, especially at rest-frame wavelengths of $\lambda >$ 5000Å. This has been observed to affect the fits to the sodium profiles in the 1D spectra, and thus a thorough re-reduction of the data is needed.

Following the re-reduction of the EXCELS spectra, we plan to undertake a more physically motivated fitting routine, to better constrain outflow incidence, velocities and kinematics. To do this, we will follow the model outlined in Rupke et al. (2005a) (see also Veilleux et al., 2020). The intensity of an absorption line can be expressed as:

$$I(\lambda) = 1 - C_f(\lambda) + C_f(\lambda)\, e^{-\tau(\lambda)}, \tag{4.6}$$

where C_f is the covering fraction (the fraction of the continuum producing source covered by the absorbing gas), and $\tau(\lambda)$ is the optical depth. The optical depth can be written as:

$$\tau(\lambda) = \tau_0\, e^{-(\lambda-\lambda_0)^2\,/\,(\lambda_o b/c)^2}, \tag{4.7}$$

where τ_0, λ_0 and b are the central optical depth, central wavelength, and Doppler width, respectively. The Doppler width can be calculated using b = FWHM / ($2\sqrt{\ln 2}$). We will then be able to more robustly constrain the mass outflow rates, by calculating column densities as a function of τ_0 and b, and using the derived covering fractions, C_f to more accurately estimate the outflow geometry. For saturated gas (e.g. Mg II), the doublet ratio method can be used to determine τ_0 (Rupke et al., 2005a; Weiner et al., 2009).

Due to the presence of the He I λ5875Å line immediately bluewards of the Na D feature, the sodium absorption profiles may be contaminated with some emission line infilling. We also plan to include a model of the He I line to account for this, comprising of a Gaussian fit to the blue side of the He I line (λ < 5875Å). Visual inspection of the spectra has also revealed a small number of galaxies showing a P-Cygni-like profile in one, or both, of the absorption features, and this profile shape will be implemented into our fits where relevant.

Where possible, we will use the `BAGPIPES` software to fit the Wild et al. (2020) star-formation history models to our sample. This will allow us to estimate, amongst others, properties such as star-formation rates, burst ages and the time since galaxies were quenched (see Sections 3.4.2 and 3.4.3). We will investigate outflow properties in our post-starburst sample as a function of galaxy properties, to determine the role outflows play in quenching galaxies at the crucial epoch of $z > 3$.

4.5 Conclusions

In this chapter, we perform a preliminary analysis of 9 post-starburst galaxies at $z > 1.8$, within the JWST EXCELS survey. The large wavelength coverage made available by JWST allows comparison of outflow properties derived from both the Mg II ($\lambda\lambda$2796, 2803Å) and Na D ($\lambda\lambda$5890, 5896Å) absorption profiles.

In an attempt to mitigate the effects of noisy continua at $\lambda > 5000$Å (evident in both the 2D and 1D reduced data), we first perform a stacking analysis of our sample (Section 4.3). The key findings are as follows:

i Stacking the six galaxies with coverage of the Mg II lines, we find a velocity offset of $v_{\mathrm{Mg\,II}} \sim 1600 \pm 470$ kms^{-1}. This outflow velocity is in very good agreement with those found for recently quenched post-starburst galaxies from ground based composite spectra ($v_{\mathrm{out}} \sim 1500$ kms^{-1}, Chapter 3).

ii Stacking our full sample and investigating the sodium profile, we find $v_{\mathrm{Na\,D}} \sim 290 \pm 130$ kms^{-1}. This is considerably lower than our $v_{\mathrm{Mg\,II}}$ value, however this could be explained by a number of factors, such as infilling from the He I line, or suppression of the highest velocity gas.

iii We derive preliminary lower limits on the mass outflow rates of $\dot{M}_{\mathrm{out,\,MgII}} \sim 1$ M$_\odot$yr^{-1} and $\dot{M}_{\mathrm{out,\,NaD}} \sim 3$ M$_\odot$yr^{-1} (Section 4.3.3.1). These are higher than the median SFR of the sample (~ 0.01 M$_\odot$yr^{-1}), indicating outflows play a key role in the quenching of galaxies at these epochs. More physically motivated modelling of the absorption line profiles will allow us to better constrain the outflow rates, along with the effects of gas saturation.

We then investigate galactic scale winds for individual objects at $z \sim 3$ (Section 4.4). We find a wide range of outflow velocities, derived from the magnesium profile, with 4/6 of our sample have outflowing components deemed significant by an F-test. The best-fitting outflow velocities cover an order of magnitude ($150 \lesssim v_{\mathrm{Mg\,II}} \lesssim 1500\,\mathrm{kms}^{-1}$). For the Na D profile, 5/6 galaxies studied showed absorption consistent with a deviation from rest-frame wavelength – 3 galaxies show evidence for outflows, 1 galaxy shows evidence for an inflow, and the final galaxy shows evidence for both outflow and an inflow. As inflows are more commonly detected in red-sequence galaxies, the wide variety of profiles indicates our sample covers galaxies in a range of quenching stages.

It is clear that JWST will allow the study of quenching systems in unprecedented detail, enabling us to uncover the role outflows play in the build up of the red sequence at cosmic noon, and beyond.

Chapter 5

Conclusions and Outlook

One of the areas of great interest in astrophysics is how galaxies transition from being blue, highly star-forming structures to red, passive systems. Recent surveys have enabled measurements of galaxy populations out to high redshifts, allowing us to determine how the fraction of these systems evolves with time, along with the characteristics of their star-forming populations and structures. The quenching of star-formation is a topic of debate, comprising many possible physical mechanisms that could theoretically lead to a gas-rich galaxy experiencing a drop in star formation. There is still a gap in our understanding, however, as to what leads to efficient quenching, particularly at high redshift ($z > 1$).

This thesis has asked the questions: (i) *How does the environment of a galaxy affect its relative quenching probability?*, (ii) *How do galactic scale winds evolve with time since a quenching event, and can this evolution untangle the influence of starburst and AGN driven winds?*, and (ii) *Are outflows key drivers of quenching at earlier epochs than cosmic noon?*

We now summarise the key findings of Chapters 2, 3 and 4, before outlining prospective future work.

5.1 The Roles of Mass and Environment in Galaxy Quenching

In Chapter 2, we analyse the build-up of the quenched galaxy population in the UKIDSS UDS from $z = 3$ to $z = 0.5$. We use a PCA analysis to identify star-forming, quiescent and post-starburst galaxies in the sample, and investigate the influence of environments using projected galaxy densities.

We find a higher fraction of passive galaxies are found in dense environments at all stellar masses in the redshift range $0.5 < z < 2.0$, as seen from a comparison of stellar mass functions. We also see a sharp up-turn in the relative abundance of low-mass ($M_* < 10^{10}$ $M_\odot$) passive galaxies and PSBs in dense environments at $z < 1.5$, which we attribute to the environmental quenching of satellite galaxies entering high-mass halos. The growth rate in the number density of passive galaxies is steepest in the highest density environments at all masses and redshifts, indicating star-forming galaxies are quenched more efficiently in these environments.

The growth in the passive population can be used to estimate the fraction of star-forming galaxies quenched per Gyr at different stellar masses, redshifts and environments. We find that the quenching probability increases with both stellar mass and environment. For the most massive galaxies, ($M_* > 10^{10.7}$ $M_\odot$) the quenching probability also increases with redshift, broadly consistent with the quenching probability being proportional to star formation rate. Averaging over all redshifts and stellar masses, we find that star-forming galaxies are 1.5 ± 0.1 times more likely to quench in the densest third of environments compared to the lowest density third. For the most massive galaxies ($M_* > 10^{10.7}$ $M_\odot$) the enhancement factor is 1.7 ± 0.2.

This study is a first attempt to separate out the influence of environment on the build-up of the passive and PSB stellar mass functions at high redshift ($z > 1$). We find strong evidence that galaxies quench more rapidly in dense environments at a given stellar mass and redshift.

5.2 The Evolution of Outflows Post Quenching

In Chapter 3, we use the Mg II ($\lambda\lambda$2796, 2803Å) absorption feature at $z > 1$ to investigate how galactic-scale outflows evolve with time since the last starburst, t_{burst}. We select two populations of recently quenched galaxies, split by t_{burst}, as well as older quenched galaxies, and a star-forming progenitor population.

We stack deep optical spectra from the UDSz and VANDELS surveys, and fit Gaussian decomposition models to the magnesium absorption profile. We find clear evidence for high-velocity outflows within our progenitors ($v_{out} \sim 1500 \pm 450$ kms^{-1}), and galaxies with $t_{burst} < 1$ Gyr ($v_{out} \sim 940 \pm 290$ and $\sim 1500 \pm 300$ kms^{-1} for galaxies with $t_{burst} <$ 0.6 Gyr and $0.6 < t_{burst} < 1$ Gyr, respectively). We find no evidence for outflows in our passive galaxy sample with $t_{burst} > 1$ Gyr.

Our sample show no signs of AGN in their optical spectral features, which may indicate that any AGN in these galaxies have very short duty cycles, and were 'off' when these galaxies were observed. The presence of significant outflows in the older quenched galaxies ($t_{burst} > 0.5$ Gyr) is difficult to explain with starburst activity alone, and may indicate energy input from episodic AGN activity as the starburst fades.

5.3 Preliminary Results From $z > 3$ Post-Starbursts

In Chapter 4, we perform a preliminary analysis of 9 post-starburst galaxies at $z >$ 1.8, within the JWST NIRSpec EXCELS survey. The large wavelength coverage made available by JWST allows us to compare outflow properties derived from both the Mg II ($\lambda\lambda$2796, 2803Å) and Na D ($\lambda\lambda$5890, 5896Å) absorption profiles.

We first perform a stacking analysis of our sample, following a similar methodology as in Chapter 3. When stacking the six galaxies with coverage of the Mg II lines, we find a velocity offset of $v_{Mg\,II} \sim 1600 \pm 350$ kms^{-1}, in good agreement with PSBs studied at $z \sim 1$. Stacking our full sample results in a sodium velocity offset of $v_{Na\,D} \sim 270$ $\pm$ 100 kms^{-1}. This is considerably lower than our $v_{Mg\,II}$ value, however this could be caused by infilling from the He I line, or suppression of the highest velocity gas. We derive preliminary lower limits on the mass outflow rates of $\dot{M}_{out,\,MgII} \sim 1$ M$_\odot$yr^{-1} and

$\dot{M}_{\mathrm{out,\,NaD}} \sim 3\ \mathrm{M_\odot yr^{-1}}$. In particular, the $\dot{M}_{\mathrm{out,\,MgII}}$ outflow rate is highly likely to be an underestimate due to line saturation. The mass outflow rates are higher than the median SFR of the sample ($\sim 0.01\ \mathrm{M_\odot yr^{-1}}$), indicating outflows play a key role in the removal of gas, and thus potentially in the quenching of star formation at these epochs.

We then investigate galactic scale winds for individual objects at $z \sim 3$. We find a wide range of outflow velocities derived from the magnesium profile, with 4/6 of our sample have outflowing components deemed significant by an F-test. The best-fitting outflow velocities for Mg II cover an order of magnitude ($150 \lesssim \mathrm{v_{Mg\,II}} \lesssim 1500\ \mathrm{kms^{-1}}$). For the Na D profile, 5/6 galaxies studied showed absorption consistent with a deviation from rest-frame wavelength, different with combinations of outflows and inflows. As inflows are more commonly detected in red-sequence galaxies, the wide variety of profiles indicates our sample covers galaxies in a range of quenching stages.

5.4 Final Thoughts and Future Work

This thesis brings to light new questions surrounding galaxy quenching, such as *'What form does galaxy environment at $z > 2$ take, and what impact does this have on the efficiency of galaxy quenching?'* and *'To what extent are outflows related to the quenching of star-formation, or are they simply along for the ride?'*.

Feedback is a multi-phase and multi-spatial problem. Despite the detection of high-velocity winds in our post-starburst galaxies, it is difficult to say for certain whether outflows are the direct cause of quenching, or simply 'along for the ride'. As we found in Chapter 4, outflows are detected up to 1 Gyr after a starburst in quenched galaxies, indicating that these winds may be relic outflows separate from the quenching event itself, perhaps driven by episodic AGN activity long after the starburst fades. Outflow energetics in PSBs appear to be consistent with AGN feedback (e.g. Wu, 2024). Outflows in warm neutral and ionised gas alone may not be enough to quench star formation, and how well these gas phases couple with the cold molecular gas phase needs more investigation. The mass outflow rates and energetics of galactic scale winds can provide insight into the relative importance of outflows in regulating star formation in galaxies. If outflow velocities are high and exceed the estimated escape velocity of the system, then it is possible that the outflowing gas may be relocated to tens of kpc away

from the galaxy centre. The need for spatially resolved observations of galaxy samples at different quenching stages is clear – the spatial extent of outflowing winds, as well as the study of different gas phases present in different locations of outflows, will help nail down the impact of galactic winds on galaxy quenching. As discussed in Section 1.3.1.1, energy injection from galactic winds may also heat surrounding gas, and smooth the ISM on small scales, preventing further collapse to the high densities needed for star formation. The comparison of star formation rates and mass outflow rates for galaxies along an evolutionary sequence, both with and without AGN, may also provide insight into whether feedback itself is halting star formation, or simply preventing further star formation after the main quenching event takes place. Additionally, the mass loading factor, $\eta \equiv \dot{M}/\,\mathrm{SFR}$, compares the amount of gas in outflow to the amount of gas actively being converted into stars, and is a simple quantification of how an outflow may impact the future evolution of the host galaxy.

Theoretical predictions of how feedback may influence the baryon cycle are quickly becoming more advanced (e.g. Nagamine, 2021; Crain & Voort, 2023), however using simulations to interpret observations of line profiles is difficult, as models do not typically create spectra with realistic observing conditions imposed. High-resolution simulations designed to test and reconstruct specific observations and outflow models are equally important, due to the incredible variety of galaxy outflow properties, as this work highlights. Simulations such as these (e.g. the Cholla Galactic OutfLow Simulations project, Schneider & Robertson, 2018) are beginning to emerge, and will provide useful constraints on the physical nature of gas in outflows.

There is plenty of exciting science still to be undertaken, both with JWST, and upcoming multi-object NIR spectrographs, such as VLT MOONS and Subaru PFS. In terms of environments, PFS and MOONS should produce the next breakthrough in this field, for the first time providing rest-frame optical spectra for thousands of quenched galaxies at high redshifts. MOONS and PFS will both cover large areas ($\sim$ few deg^2), including the UDS field, and hence will cover a range range of environments at high z. Surveys with these instruments should allow a more precise characterisation of the density field, while also allowing a comparison of the detailed astrophysical properties of galaxies in different environments. By comparing star-formation histories, quenching timescales, metallicities, and AGN contributions, it may be possible to separate the detailed influence of environment and distinguish between quenching mechanisms.

As outlined in Section 4.4.1.1, the EXCELS PSBs will be studied in depth in the near future, using more physically motivated models, to better constrain outflow incidence, velocities and kinematics. We will use the `BAGPIPES` software to fit model star-formation histories models to our sample. This, in turn, will allow the investigation of outflow kinematics as a function of galaxy properties, to determine the role outflows play in quenching galaxies at the crucial epoch of $z > 3$. As MOONRISE is set to provide hundreds of thousands of galaxy spectra, it will be an ideal survey with which to undertake detailed studies into the ISM, kinematics, AGN features and stellar population age gradients of different galaxy populations at $z > 1$. MOONS is set to target $\sim$ 90,000 passive galaxies and $\sim$ 3000 post-starburst systems, enabling the study of the evolution of galactic-scale outflows, kinematics, and quenching timescales of galaxies over cosmic noon.

The scope for future work is huge, and the combined results from JWST, MOONS and PFS are set to transform our understanding of galaxy quenching. The next generation of astronomical surveys will provide countless exciting opportunities to deepen our knowledge of galaxy evolution, and the Universe as a whole.

Bibliography

Abell, G. O. 1965, Annual Review of Astronomy and Astrophysics, 3, 1, doi: 10.1146/annurev.aa.03.090165.000245

Alatalo, K., Blitz, L., Young, L. M., et al. 2011, The Astrophysical Journal, 735, 88, doi: 10.1088/0004-637X/735/2/88

Alatalo, K., Cales, S. L., Rich, J. A., et al. 2016, The Astrophysical Journal Supplement Series, 224, 38, doi: 10.3847/0067-0049/224/2/38

Alberts, S., Williams, C. C., Helton, J. M., et al. 2023, To high redshift and low mass: exploring the emergence of quenched galaxies and their environments at $3<z<6$ in the ultra-deep JADES MIRI F770W parallel, arXiv, doi: 10.48550/arXiv.2312.12207

Alexander, D. M., Swinbank, A. M., Smail, I., McDermid, R., & Nesvadba, N. P. H. 2010, Monthly Notices of the Royal Astronomical Society, 402, 2211, doi: 10.1111/j.1365-2966.2009.16046.x

Almaini, O., Wild, V., Maltby, D. T., et al. 2017, Monthly Notices of the Royal Astronomical Society, 472, 1401, doi: 10.1093/mnras/stx1957

Annunziatella, M., Mercurio, A., Biviano, A., et al. 2016, Astronomy & Astrophysics, 585, A160, doi: 10.1051/0004-6361/201527399

Bahé, Y. M., & McCarthy, I. G. 2015, Monthly Notices of the Royal Astronomical Society, 447, 969, doi: 10.1093/mnras/stu2293

Baldry, I. K., Balogh, M. L., Bower, R. G., et al. 2006, Monthly Notices of the Royal Astronomical Society, 373, 469, doi: 10.1111/j.1365-2966.2006.11081.x

Baldry, I. K., Glazebrook, K., Brinkmann, J., et al. 2004, The Astrophysical Journal, 600, 681, doi: 10.1086/380092

Baldry, I. K., Glazebrook, K., & Driver, S. P. 2008, Monthly Notices of the Royal Astronomical Society, 945, doi: 10.1111/j.1365-2966.2008.13348.x

Balogh, M. L., & Morris, S. L. 2000, Monthly Notices of the Royal Astronomical Society, 318, 703, doi: 10.1046/j.1365-8711.2000.03826.x

Balogh, M. L., Morris, S. L., Yee, H. K. C., Carlberg, R. G., & Ellingson, E. 1997, The Astrophysical Journal, 488, L75, doi: 10.1086/310927

—. 1999, The Astrophysical Journal, 527, 54, doi: 10.1086/308056

Balogh, M. L., McGee, S. L., Mok, A., et al. 2016, Monthly Notices of the Royal Astronomical Society, 456, 4364, doi: 10.1093/mnras/stv2949

Baron, D., Netzer, H., Davies, R. I., & Xavier Prochaska, J. 2020, Monthly Notices of the Royal Astronomical Society, 494, 5396, doi: 10.1093/mnras/staa1018

Baron, D., Netzer, H., Lutz, D., Prochaska, J. X., & Davies, R. I. 2022, Monthly Notices of the Royal Astronomical Society, 509, 4457, doi: 10.1093/mnras/stab3232

Baron, D., Netzer, H., Poznanski, D., Prochaska, J. X., & Förster Schreiber, N. M. 2017, Monthly Notices of the Royal Astronomical Society, 470, 1687, doi: 10.1093/mnras/stx1329

Baron, D., Netzer, H., Prochaska, J. X., et al. 2018, Monthly Notices of the Royal Astronomical Society, 480, 3993, doi: 10.1093/mnras/sty2113

Barro, G., Faber, S. M., Pérez-González, P. G., et al. 2013, The Astrophysical Journal, 765, 104, doi: 10.1088/0004-637X/765/2/104

Barton, E. J., Geller, M. J., & Kenyon, S. J. 2000, The Astrophysical Journal, 530, 660, doi: 10.1086/308392

Bekki, K. 1998, The Astrophysical Journal, 502, L133, doi: 10.1086/311508

Bell, E. F., McIntosh, D. H., Katz, N., & Weinberg, M. D. 2003, The Astrophysical Journal Supplement Series, 149, 289, doi: 10.1086/378847

Bell, E. F., Phleps, S., Somerville, R. S., et al. 2006, The Astrophysical Journal, 652, 270, doi: 10.1086/508408

Bell, E. F., Wolf, C., Meisenheimer, K., et al. 2004, The Astrophysical Journal, 608, 752, doi: 10.1086/420778

Belli, S., Newman, A. B., & Ellis, R. S. 2019, The Astrophysical Journal, 874, 17, doi: 10.3847/1538-4357/ab07af

Belli, S., Park, M., Davies, R. L., et al. 2023, arXiv e-prints, doi: 10.48550/arXiv.2308.05795

Benson, A. J., Bower, R. G., Frenk, C. S., et al. 2003, The Astrophysical Journal, 599, 38, doi: 10.1086/379160

Best, P. N., Kauffmann, G., Heckman, T. M., et al. 2005, Monthly Notices of the Royal Astronomical Society, 362, 25, doi: 10.1111/j.1365-2966.2005.09192.x

Bhambhani, P. C., Baldry, I. K., Brough, S., et al. 2023, Monthly Notices of the Royal Astronomical Society, 522, 4116, doi: 10.1093/mnras/stad1218

Bialas, D., Lisker, T., Olczak, C., Spurzem, R., & Kotulla, R. 2015, Astronomy & Astrophysics, 576, A103, doi: 10.1051/0004-6361/201425235

Bluck, A. F. L., Conselice, C. J., Buitrago, F., et al. 2012, The Astrophysical Journal, 747, 34, doi: 10.1088/0004-637X/747/1/34

Bohlin, R. C., Cornett, R. H., Hill, J. K., et al. 1991, The Astrophysical Journal, 368, 12, doi: 10.1086/169666

Bordoloi, R., Lilly, S. J., Hardmeier, E., et al. 2014, The Astrophysical Journal, 794, 130, doi: 10.1088/0004-637X/794/2/130

Borthakur, S., Heckman, T., Strickland, D., Wild, V., & Schiminovich, D. 2013, The Astrophysical Journal, 768, 18, doi: 10.1088/0004-637X/768/1/18

Boselli, A., Fossati, M., & Sun, M. 2022, Astronomy and Astrophysics Review, 30, 3, doi: 10.1007/s00159-022-00140-3

Bower, R. G., Benson, A. J., & Crain, R. A. 2012, Monthly Notices of the Royal Astronomical Society, 422, 2816, doi: 10.1111/j.1365-2966.2012.20516.x

Bradshaw, E. J., Almaini, O., Hartley, W. G., et al. 2013, Monthly Notices of the Royal Astronomical Society, 433, 194, doi: 10.1093/mnras/stt715

Brammer, G. B., van Dokkum, P. G., & Coppi, P. 2008, The Astrophysical Journal, 686, 1503, doi: 10.1086/591786

Brammer, G. B., Whitaker, K. E., van Dokkum, P. G., et al. 2009, The Astrophysical Journal, 706, L173, doi: 10.1088/0004-637X/706/1/L173

Bridge, C. R., Appleton, P. N., Conselice, C. J., et al. 2007, The Astrophysical Journal, 659, 931, doi: 10.1086/512029

Brinchmann, J., Charlot, S., White, S. D. M., et al. 2004, Monthly Notices of the Royal Astronomical Society, 351, 1151, doi: 10.1111/j.1365-2966.2004.07881.x

Brough, S., Hopkins, A. M., Sharp, R. G., et al. 2011, Monthly Notices of the Royal Astronomical Society, 413, 1236, doi: 10.1111/j.1365-2966.2011.18210.x

Bruzual, G., & Charlot, S. 2003, Monthly Notices of the Royal Astronomical Society, 344, 1000, doi: 10.1046/j.1365-8711.2003.06897.x

Bruzual A., G. 1983, The Astrophysical Journal, 273, 105, doi: 10.1086/161352

Cappellari, M. 2017, Monthly Notices of the Royal Astronomical Society, 466, 798, doi: 10.1093/mnras/stw3020

—. 2023, Monthly Notices of the Royal Astronomical Society, 526, 3273, doi: 10.1093/mnras/stad2597

Cappellari, M., & Emsellem, E. 2004, Publications of the Astronomical Society of the Pacific, 116, 138, doi: 10.1086/381875

Carnall, A. C. 2017, SpectRes: A Fast Spectral Resampling Tool in Python, arXiv, doi: 10.48550/arXiv.1705.05165

Carnall, A. C., McLure, R. J., Dunlop, J. S., & Davé, R. 2018, Monthly Notices of the Royal Astronomical Society, 480, 4379, doi: 10.1093/mnras/sty2169

Carnall, A. C., McLure, R. J., Dunlop, J. S., et al. 2019, Monthly Notices of the Royal Astronomical Society, 490, 417, doi: 10.1093/mnras/stz2544

Carnall, A. C., Walker, S., McLure, R. J., et al. 2020, Monthly Notices of the Royal Astronomical Society, 496, 695, doi: 10.1093/mnras/staa1535

Carnall, A. C., McLeod, D. J., McLure, R. J., et al. 2023a, Monthly Notices of the Royal Astronomical Society, 520, 3974, doi: 10.1093/mnras/stad369

Carnall, A. C., McLure, R. J., Dunlop, J. S., et al. 2023b, Nature, 619, 716, doi: 10.1038/s41586-023-06158-6

Carnall, A. C., Cullen, F., McLure, R. J., et al. 2024, The JWST EXCELS survey: Too much, too young, too fast? Ultra-massive quiescent galaxies at 3 < z < 5, doi: 10.48550/arXiv.2405.02242

Casteels, K. R. V., Conselice, C. J., Bamford, S. P., et al. 2014, Monthly Notices of the Royal Astronomical Society, 445, 1157, doi: 10.1093/mnras/stu1799

Chen, Y.-M., Tremonti, C. A., Heckman, T. M., et al. 2010, The Astronomical Journal, 140, 445, doi: 10.1088/0004-6256/140/2/445

Cicone, C., Maiolino, R., Sturm, E., et al. 2014, Astronomy and Astrophysics, 562, A21, doi: 10.1051/0004-6361/201322464

Cimatti, A., Brusa, M., Talia, M., et al. 2013, The Astrophysical Journal, 779, L13, doi: 10.1088/2041-8205/779/1/L13

Coil, A. L. 2013, in Planets, Stars and Stellar Systems: Volume 6: Extragalactic Astronomy and Cosmology, ed. T. D. Oswalt & W. C. Keel (Dordrecht: Springer Netherlands), 387–421, doi: 10.1007/978-94-007-5609-0_8

Coil, A. L., Weiner, B. J., Holz, D. E., et al. 2011, The Astrophysical Journal, 743, 46, doi: 10.1088/0004-637X/743/1/46

Cole, S., Lacey, C. G., Baugh, C. M., & Frenk, C. S. 2000, Monthly Notices of the Royal Astronomical Society, 319, 168, doi: 10.1046/j.1365-8711.2000.03879.x

Combes, F. 2017, Frontiers in Astronomy and Space Sciences, 4, doi: 10.3389/fspas.2017.00010

Conroy, C., & Gunn, J. E. 2010, The Astrophysical Journal, 712, 833, doi: 10.1088/0004-637X/712/2/833

Conroy, C., Gunn, J. E., & White, M. 2009, The Astrophysical Journal, 699, 486, doi: 10.1088/0004-637X/699/1/486

Conselice, C. J. 2014, Annual Review of Astronomy and Astrophysics, 52, 291, doi: 10.1146/annurev-astro-081913-040037

Conselice, C. J., Bershady, M. A., Dickinson, M., & Papovich, C. 2003, The Astronomical Journal, 126, 1183, doi: 10.1086/377318

Conselice, C. J., Mundy, C. J., Ferreira, L., & Duncan, K. 2022, The Astrophysical Journal, 940, 168, doi: 10.3847/1538-4357/ac9b1a

Cooper, M. C., Griffith, R. L., Newman, J. A., et al. 2012, Monthly Notices of the Royal Astronomical Society, 419, 3018, doi: 10.1111/j.1365-2966.2011.19938.x

Cortese, L., Catinella, B., & Smith, R. 2021, Publications of the Astronomical Society of Australia, 38, e035, doi: 10.1017/pasa.2021.18

Cox, T. J., Primack, J., Jonsson, P., & Somerville, R. S. 2004, The Astrophysical Journal, 607, L87, doi: 10.1086/421905

Crain, R. A., & Voort, F. v. d. 2023, Annual Review of Astronomy and Astrophysics, 61, 473, doi: 10.1146/annurev-astro-041923-043618

Croton, D. J., Farrar, G. R., Norberg, P., et al. 2005, Monthly Notices of the Royal Astronomical Society, 356, 1155, doi: 10.1111/j.1365-2966.2004.08546.x

Cucciati, O., Iovino, A., Marinoni, C., et al. 2006, Astronomy and Astrophysics, 458, 39, doi: 10.1051/0004-6361:20065161

Daddi, E., Dickinson, M., Morrison, G., et al. 2007, The Astrophysical Journal, 670, 156, doi: 10.1086/521818

Darvish, B., Mobasher, B., Sobral, D., et al. 2016, The Astrophysical Journal, 825, 113, doi: 10.3847/0004-637X/825/2/113

Davies, R. L., Belli, S., Park, M., et al. 2024, Monthly Notices of the Royal Astronomical Society, 528, 4976, doi: 10.1093/mnras/stae327

Davis, J. D., Tremonti, C. A., Swiggum, C. N., et al. 2023, The Astrophysical Journal, 951, 105, doi: 10.3847/1538-4357/accbbf

De Lucia, G., Weinmann, S., Poggianti, B., Aragon-Salamanca, A., & Zaritsky, D. 2012, Monthly Notices of the Royal Astronomical Society, 423, 1277, doi: 10.1111/j.1365-2966.2012.20983.x

Debuhr, J., Quataert, E., & Ma, C.-P. 2012, Monthly Notices of the Royal Astronomical Society, 420, 2221, doi: 10.1111/j.1365-2966.2011.20187.x

Dekel, A., & Silk, J. 1986, The Astrophysical Journal, 303, 39, doi: 10.1086/164050

Delahaye, A. G., Webb, T. M. A., Nantais, J., et al. 2017, The Astrophysical Journal, 843, 126, doi: 10.3847/1538-4357/aa756a

Delaye, L., Huertas-Company, M., Mei, S., et al. 2014, Monthly Notices of the Royal Astronomical Society, 441, 203, doi: 10.1093/mnras/stu496

Delvecchio, I., Daddi, E., Aird, J., et al. 2020, The Astrophysical Journal, 892, 17, doi: 10.3847/1538-4357/ab789c

Deruelle, N., & Uzan, J.-P. 2018, in Relativity in Modern Physics, ed. N. Deruelle, J.-P. Uzan, & P. de Forcrand-Millard (Oxford University Press), 0, doi: 10.1093/oso/9780198786399.003.0059

D'Eugenio, F., Perez-Gonzalez, P., Maiolino, R., et al. 2023, A fast-rotator post-starburst galaxy quenched by supermassive black-hole feedback at z=3, arXiv. http://arxiv.org/abs/2308.06317

Diamond-Stanic, A. M., Moustakas, J., Tremonti, C. A., et al. 2012, The Astrophysical Journal, 755, L26, doi: 10.1088/2041-8205/755/2/L26

Donovan, J. L., Serra, P., van Gorkom, J. H., et al. 2009, The Astronomical Journal, 137, 5037, doi: 10.1088/0004-6256/137/6/5037

Draine, B. T. 2011, Physics of the Interstellar and Intergalactic Medium. https://ui.adsabs.harvard.edu/abs/2011piim.book.....D

Dressler, A. 1980, The Astrophysical Journal, 236, 351, doi: 10.1086/157753

Dressler, A., & Gunn, J. E. 1983, The Astrophysical Journal, 270, 7, doi: 10.1086/161093

Dressler, A., Oemler, Jr., A., Couch, W. J., et al. 1997, The Astrophysical Journal, 490, 577, doi: 10.1086/304890

Duncan, K., Conselice, C. J., Mundy, C., et al. 2019, The Astrophysical Journal, 876, 110, doi: 10.3847/1538-4357/ab148a

Dunlop, J. S., Abraham, R. G., Ashby, M. L. N., et al. 2021, JWST Proposal. Cycle 1, 1837. https://ui.adsabs.harvard.edu/abs/2021jwst.prop.1837D

Efstathiou, G. 2000, Monthly Notices of the Royal Astronomical Society, 317, 697, doi: 10.1046/j.1365-8711.2000.03665.x

Ellison, S. L., Mendel, J. T., Patton, D. R., & Scudder, J. M. 2013, Monthly Notices of the Royal Astronomical Society, 435, 3627, doi: 10.1093/mnras/stt1562

Ellison, S. L., Patton, D. R., Simard, L., et al. 2010, Monthly Notices of the Royal Astronomical Society, 407, 1514, doi: 10.1111/j.1365-2966.2010.17076.x

Fabian, A. C. 1999, Monthly Notices of the Royal Astronomical Society, 308, L39, doi: 10.1046/j.1365-8711.1999.03017.x

—. 2012, Annual Review of Astronomy and Astrophysics, 50, 455, doi: 10.1146/annurev-astro-081811-125521

Feruglio, C., Maiolino, R., Piconcelli, E., et al. 2010, Astronomy and Astrophysics, 518, L155, doi: 10.1051/0004-6361/201015164

Fluetsch, A., Maiolino, R., Carniani, S., et al. 2019, Monthly Notices of the Royal Astronomical Society, 483, 4586, doi: 10.1093/mnras/sty3449

Franzetti, P., Scodeggio, M., Garilli, B., et al. 2007, Astronomy & Astrophysics, 465, 711, doi: 10.1051/0004-6361:20065942

French, K. D. 2021, Publications of the Astronomical Society of the Pacific, 133, 072001, doi: 10.1088/1538-3873/ac0a59

French, K. D., Earl, N., Novack, A. B., et al. 2023, The Astrophysical Journal, 950, 153, doi: 10.3847/1538-4357/acd249

French, K. D., Yang, Y., Zabludoff, A., et al. 2015, The Astrophysical Journal, 801, 1, doi: 10.1088/0004-637X/801/1/1

Fujita, A., Martin, C. L., Mac Low, M.-M., New, K. C. B., & Weaver, R. 2009, The Astrophysical Journal, 698, 693, doi: 10.1088/0004-637X/698/1/693

Furusawa, H., Kosugi, G., Akiyama, M., et al. 2008, The Astrophysical Journal Supplement Series, 176, 1, doi: 10.1086/527321

Gao, F., Wang, L., Pearson, W. J., et al. 2020, Astronomy & Astrophysics, 637, A94, doi: 10.1051/0004-6361/201937178

Garilli, B., Fumana, M., Franzetti, P., et al. 2010, Publications of the Astronomical Society of the Pacific, 122, 827, doi: 10.1086/654903

Garilli, B., McLure, R., Pentericci, L., et al. 2021, Astronomy and Astrophysics, 647, A150, doi: 10.1051/0004-6361/202040059

Geach, J. E., Hickox, R. C., Diamond-Stanic, A. M., et al. 2014, Nature, 516, 68, doi: 10.1038/nature14012

Gensior, J., Kruijssen, J. M. D., & Keller, B. W. 2020, Monthly Notices of the Royal Astronomical Society, 495, 199, doi: 10.1093/mnras/staa1184

González Delgado, R. M., Rodríguez-Martín, J. E., Díaz-García, L. A., et al. 2022, Astronomy and Astrophysics, 666, A84, doi: 10.1051/0004-6361/202244030

Goto, T. 2005, Monthly Notices of the Royal Astronomical Society, 357, 937, doi: 10.1111/j.1365-2966.2005.08701.x

—. 2007, Monthly Notices of the Royal Astronomical Society, 381, 187, doi: 10.1111/j.1365-2966.2007.12227.x

Goto, T., Nichol, R. C., Okamura, S., et al. 2003, Publications of the Astronomical Society of Japan, 55, 771, doi: 10.1093/pasj/55.4.771

Goulding, A. D., Greene, J. E., Bezanson, R., et al. 2018, Publications of the Astronomical Society of Japan, 70, S37, doi: 10.1093/pasj/psx135

Grützbauch, R., Conselice, C. J., Varela, J., et al. 2011, Monthly Notices of the Royal Astronomical Society, 411, 929, doi: 10.1111/j.1365-2966.2010.17727.x

Guillard, P., Boulanger, F., Lehnert, M. D., et al. 2015, Astronomy & Astrophysics, 574, A32, doi: 10.1051/0004-6361/201423612

Gunn, J. E., & Gott, III, J. R. 1972, The Astrophysical Journal, 176, 1, doi: 10.1086/151605

Gómez, P. L., Nichol, R. C., Miller, C. J., et al. 2003, The Astrophysical Journal, 584, 210, doi: 10.1086/345593

Hainline, K. N., Shapley, A. E., Greene, J. E., & Steidel, C. C. 2011, The Astrophysical Journal, 733, 31, doi: 10.1088/0004-637X/733/1/31

Hamadouche, M. L., Carnall, A. C., McLure, R. J., et al. 2023, Monthly Notices of the Royal Astronomical Society, 521, 5400, doi: 10.1093/mnras/stad773

Harrison, C. M., & Ramos Almeida, C. 2024, Galaxies, 12, 17, doi: 10.3390/galaxies12020017

Harrison, C. M., Alexander, D. M., Swinbank, A. M., et al. 2012, Monthly Notices of the Royal Astronomical Society, 426, 1073, doi: 10.1111/j.1365-2966.2012.21723.x

Heckman, T. M., Alexandroff, R. M., Borthakur, S., Overzier, R., & Leitherer, C. 2015, The Astrophysical Journal, 809, 147, doi: 10.1088/0004-637X/809/2/147

Heckman, T. M., & Best, P. N. 2014, Annual Review of Astronomy and Astrophysics, 52, 589, doi: 10.1146/annurev-astro-081913-035722

Heckman, T. M., & Borthakur, S. 2016, The Astrophysical Journal, 822, 9, doi: 10.3847/0004-637X/822/1/9

Heckman, T. M., & Thompson, T. A. 2017, Galactic Winds and the Role Played by Massive Stars, doi: 10.48550/arXiv.1701.09062

Hopkins, P. F., Hernquist, L., Cox, T. J., et al. 2006, The Astrophysical Journal Supplement Series, 163, 1, doi: 10.1086/499298

Hubble, E., & Humason, M. L. 1931, The Astrophysical Journal, 74, 43, doi: 10.1086/143323

Hubble, E. P. 1925a, The Observatory, 48, 139. https://ui.adsabs.harvard.edu/abs/1925Obs....48..139H

—. 1925b, The Astrophysical Journal, 62, 409, doi: 10.1086/142943

—. 1936, Realm of the Nebulae. https://ui.adsabs.harvard.edu/abs/1936rene.book.....H

Huchra, J. P., & Geller, M. J. 1982, The Astrophysical Journal, 257, 423, doi: 10.1086/160000

Huertas-Company, M., Mei, S., Shankar, F., et al. 2013, Monthly Notices of the Royal Astronomical Society, 428, 1715, doi: 10.1093/mnras/sts150

Humason, M. L. 1936, The Astrophysical Journal, 83, 10, doi: 10.1086/143696

Hwang, J.-S., Park, C., Banerjee, A., & Hwang, H. S. 2018, The Astrophysical Journal, 856, 160, doi: 10.3847/1538-4357/aab3ce

Icke, V. 1985, Astronomy and Astrophysics, 144, 115. https://ui.adsabs.harvard.edu/abs/1985A&A...144..115I

Ilbert, O., McCracken, H. J., Fèvre, O. L., et al. 2013, Astronomy & Astrophysics, 556, A55, doi: 10.1051/0004-6361/201321100

Jackson, R. A., Martin, G., Kaviraj, S., et al. 2019, Monthly Notices of the Royal Astronomical Society, 489, 4679, doi: 10.1093/mnras/stz2440

Jarvis, M. J., Bonfield, D. G., Bruce, V. A., et al. 2013, Monthly Notices of the Royal Astronomical Society, 428, 1281, doi: 10.1093/mnras/sts118

Jogee, S., Miller, S. H., Penner, K., et al. 2009, The Astrophysical Journal, 697, 1971, doi: 10.1088/0004-637X/697/2/1971

Kampczyk, P., Lilly, S. J., de Ravel, L., et al. 2013, The Astrophysical Journal, 762, 43, doi: 10.1088/0004-637X/762/1/43

Kauffmann, G., Heckman, T. M., White, S. D. M., et al. 2003, Monthly Notices of the Royal Astronomical Society, 341, 33, doi: 10.1046/j.1365-8711.2003.06291.x

Kawinwanichakij, L., Papovich, C., Quadri, R. F., et al. 2017, The Astrophysical Journal, 847, 134, doi: 10.3847/1538-4357/aa8b75

Kennicutt, R. C., & Evans, N. J. 2012, Annual Review of Astronomy and Astrophysics, 50, 531, doi: 10.1146/annurev-astro-081811-125610

Kim, C.-G., Ostriker, E. C., Somerville, R. S., et al. 2020, The Astrophysical Journal, 900, 61, doi: 10.3847/1538-4357/aba962

Knobel, C., Lilly, S. J., Woo, J., & Kovač, K. 2015, The Astrophysical Journal, 800, 24, doi: 10.1088/0004-637X/800/1/24

Kocevski, D. D., Hasinger, G., Brightman, M., et al. 2018, The Astrophysical Journal Supplement Series, 236, 48, doi: 10.3847/1538-4365/aab9b4

Kodama, T., Smail, I., Nakata, F., Okamura, S., & Bower, R. G. 2001, The Astrophysical Journal, 562, L9, doi: 10.1086/338100

Kormendy, J., & Illingworth, G. 1982, The Astrophysical Journal, 256, 460, doi: 10.1086/159923

Kovac, K., Lilly, S. J., Knobel, C., et al. 2014, Monthly Notices of the Royal Astronomical Society, 438, 717, doi: 10.1093/mnras/stt2241

Kravtsov, A., & Borgani, S. 2012, Annual Review of Astronomy and Astrophysics, 50, 353, doi: 10.1146/annurev-astro-081811-125502

Kuchner, U., Ziegler, B., Verdugo, M., Bamford, S., & Häußler, B. 2017, Astronomy and Astrophysics, 604, A54, doi: 10.1051/0004-6361/201630252

Lambas, D. G., Alonso, S., Mesa, V., & O'Mill, A. L. 2012, Astronomy & Astrophysics, 539, A45, doi: 10.1051/0004-6361/201117900

Lani, C., Almaini, O., Hartley, W. G., et al. 2013, Monthly Notices of the Royal Astronomical Society, 435, 207, doi: 10.1093/mnras/stt1275

Lanz, L., Stepanoff, S., Hickox, R. C., et al. 2022, The Astrophysical Journal, 935, 29, doi: 10.3847/1538-4357/ac7d56

Larson, R. B. 1974, Monthly Notices of the Royal Astronomical Society, 169, 229, doi: 10.1093/mnras/169.2.229

Larson, R. B., Tinsley, B. M., & Caldwell, C. N. 1980, The Astrophysical Journal, 237, 692, doi: 10.1086/157917

Lawrence, A., Warren, S. J., Almaini, O., et al. 2007, Monthly Notices of the Royal Astronomical Society, 379, 1599, doi: 10.1111/j.1365-2966.2007.12040.x

Leja, J., Speagle, J. S., Johnson, B. D., et al. 2020, The Astrophysical Journal, 893, 111, doi: 10.3847/1538-4357/ab7e27

Lemaux, B. C., Tomczak, A. R., Lubin, L. M., et al. 2019, Monthly Notices of the Royal Astronomical Society, 490, 1231, doi: 10.1093/mnras/stz2661

Lin, L., Patton, D. R., Koo, D. C., et al. 2008, The Astrophysical Journal, 681, 232, doi: 10.1086/587928

Lin, L., Jian, H.-Y., Foucaud, S., et al. 2014, The Astrophysical Journal, 782, 33, doi: 10.1088/0004-637X/782/1/33

Lotz, J. M., Jonsson, P., Cox, T. J., et al. 2011, The Astrophysical Journal, 742, 103, doi: 10.1088/0004-637X/742/2/103

Lotz, M., Dolag, K., Remus, R.-S., & Burkert, A. 2021, Monthly Notices of the Royal Astronomical Society, 506, 4516, doi: 10.1093/mnras/stab2037

Luo, Y., Rowlands, K., Alatalo, K., et al. 2022, The Astrophysical Journal, 938, 63, doi: 10.3847/1538-4357/ac8b7d

Madau, P., & Dickinson, M. 2014, Annual Review of Astronomy and Astrophysics, 52, 415, doi: 10.1146/annurev-astro-081811-125615

Maiolino, R., Gallerani, S., Neri, R., et al. 2012, Monthly Notices of the Royal Astronomical Society, 425, L66, doi: 10.1111/j.1745-3933.2012.01303.x

Maltby, D., Almaini, O., Wild, V., et al. 2016, Monthly Notices of the Royal Astronomical Society, 459, L114, doi: 10.1093/mnrasl/slw057

Maltby, D. T., Almaini, O., Wild, V., et al. 2018, Monthly Notices of the Royal Astronomical Society, 480, 381, doi: 10.1093/mnras/sty1794

Maltby, D. T., Aragón-Salamanca, A., Gray, M. E., et al. 2010, Monthly Notices of the Royal Astronomical Society, 402, 282, doi: 10.1111/j.1365-2966.2009.15953.x

Maltby, D. T., Almaini, O., McLure, R. J., et al. 2019, Monthly Notices of the Royal Astronomical Society, 489, 1139, doi: 10.1093/mnras/stz2211

Man, A. W. S., Zabl, J., Brammer, G. B., et al. 2021, The Astrophysical Journal, 919, 20, doi: 10.3847/1538-4357/ac0ae3

Mao, Z., Kodama, T., Pérez-Martínez, J. M., et al. 2022, Astronomy & Astrophysics, 666, A141, doi: 10.1051/0004-6361/202243733

Marasco, A., Crain, R. A., Schaye, J., et al. 2016, Monthly Notices of the Royal Astronomical Society, 461, 2630, doi: 10.1093/mnras/stw1498

Martig, M., Bournaud, F., Teyssier, R., & Dekel, A. 2009, The Astrophysical Journal, 707, 250, doi: 10.1088/0004-637X/707/1/250

Martig, M., Crocker, A. F., Bournaud, F., et al. 2013, Monthly Notices of the Royal Astronomical Society, 432, 1914, doi: 10.1093/mnras/sts594

Martin, C. L., & Bouché, N. 2009, The Astrophysical Journal, 703, 1394, doi: 10.1088/0004-637X/703/2/1394

McLeod, D. J., McLure, R. J., Dunlop, J. S., et al. 2021, Monthly Notices of the Royal Astronomical Society, 503, 4413, doi: 10.1093/mnras/stab731

McLure, R. J., Pearce, H. J., Dunlop, J. S., et al. 2013, Monthly Notices of the Royal Astronomical Society, 428, 1088, doi: 10.1093/mnras/sts092

McLure, R. J., Pentericci, L., Cimatti, A., et al. 2018, Monthly Notices of the Royal Astronomical Society, 479, 25, doi: 10.1093/mnras/sty1213

McNab, K., Balogh, M. L., van der Burg, R. F. J., et al. 2021, Monthly Notices of the Royal Astronomical Society, 508, 157, doi: 10.1093/mnras/stab2558

McNamara, B. R., & Nulsen, P. E. J. 2007, Annual Review of Astronomy and Astrophysics, 45, 117, doi: 10.1146/annurev.astro.45.051806.110625

McNamara, B. R., Nulsen, P. E. J., Wise, M. W., et al. 2005, Nature, 433, 45, doi: 10.1038/nature03202

Mei, S., Hatch, N. A., Amodeo, S., et al. 2023, Astronomy and Astrophysics, 670, A58, doi: 10.1051/0004-6361/202243551

Mihos, J. C., & Hernquist, L. 1994, The Astrophysical Journal, 425, L13, doi: 10.1086/187299

Moore, B., Katz, N., Lake, G., Dressler, A., & Oemler, A. 1996, Nature, 379, 613, doi: 10.1038/379613a0

Moore, B., Lake, G., Quinn, T., & Stadel, J. 1999, Monthly Notices of the Royal Astronomical Society, 304, 465, doi: 10.1046/j.1365-8711.1999.02345.x

Morganti, R. 2017, Frontiers in Astronomy and Space Sciences, 4, doi: 10.3389/fspas.2017.00042

Mortazavi, S. A., & Lotz, J. M. 2019, Monthly Notices of the Royal Astronomical Society, 487, 1551, doi: 10.1093/mnras/stz1331

Mortlock, A., Conselice, C. J., Hartley, W. G., et al. 2015, Monthly Notices of the Royal Astronomical Society, 447, 2, doi: 10.1093/mnras/stu2403

Moster, B. P., Somerville, R. S., Newman, J. A., & Rix, H.-W. 2011, The Astrophysical Journal, 731, 113, doi: 10.1088/0004-637X/731/2/113

Moustakas, J., Coil, A. L., Aird, J., et al. 2013, The Astrophysical Journal, 767, 50, doi: 10.1088/0004-637X/767/1/50

Muldrew, S. I., Croton, D. J., Skibba, R. A., et al. 2012, Monthly Notices of the Royal Astronomical Society, 419, 2670, doi: 10.1111/j.1365-2966.2011.19922.x

Mundy, C. J., Conselice, C. J., Duncan, K. J., et al. 2017, Monthly Notices of the Royal Astronomical Society, 470, 3507, doi: 10.1093/mnras/stx1238

Murray, N., Ménard, B., & Thompson, T. A. 2011, The Astrophysical Journal, 735, 66, doi: 10.1088/0004-637X/735/1/66

Muzzin, A., Wilson, G., Yee, H. K. C., et al. 2012, The Astrophysical Journal, 746, 188, doi: 10.1088/0004-637X/746/2/188

Muzzin, A., Marchesini, D., Stefanon, M., et al. 2013, The Astrophysical Journal, 777, 18, doi: 10.1088/0004-637X/777/1/18

Muzzin, A., van der Burg, R. F. J., McGee, S. L., et al. 2014, The Astrophysical Journal, 796, 65, doi: 10.1088/0004-637X/796/1/65

Nagamine, K. 2021, Proceedings of the International Astronomical Union, 17, 283, doi: 10.1017/S1743921323000133

Nantais, J. B., Burg, R. F. J. v. d., Lidman, C., et al. 2016, Astronomy & Astrophysics, 592, A161, doi: 10.1051/0004-6361/201628663

Noeske, K. G., Weiner, B. J., Faber, S. M., et al. 2007, The Astrophysical Journal, 660, L43, doi: 10.1086/517926

Noirot, G., Stern, D., Mei, S., et al. 2018, The Astrophysical Journal, 859, 38, doi: 10.3847/1538-4357/aabadb

Oemler, Jr., A. 1974, The Astrophysical Journal, 194, 1, doi: 10.1086/153216

Ostriker, J. P. 1980, Comments on Astrophysics, 8, 177. https://ui.adsabs.harvard.edu/abs/1980ComAp...8..177O

Otter, J. A., Rowlands, K., Alatalo, K., et al. 2022, The Astrophysical Journal, 941, 93, doi: 10.3847/1538-4357/ac9dee

Owers, M. S., Hudson, M. J., Oman, K. A., et al. 2019, Astrophysical Journal, 873, doi: 10.3847/1538-4357/ab0201

Ownsworth, J. R., Conselice, C. J., Mortlock, A., et al. 2014, Monthly Notices of the Royal Astronomical Society, 445, 2198, doi: 10.1093/mnras/stu1802

Paccagnella, A., Vulcani, B., Poggianti, B. M., et al. 2019, Monthly Notices of the Royal Astronomical Society, 482, 881, doi: 10.1093/mnras/sty2728

—. 2017, The Astrophysical Journal, 838, 148, doi: 10.3847/1538-4357/aa64d7

Papovich, C., Bassett, R., Lotz, J. M., et al. 2012, The Astrophysical Journal, 750, 93, doi: 10.1088/0004-637X/750/2/93

Papovich, C., Kawinwanichakij, L., Quadri, R. F., et al. 2018, The Astrophysical Journal, 854, 30, doi: 10.3847/1538-4357/aaa766

Park, M., Belli, S., Conroy, C., et al. 2023, The Astrophysical Journal, 953, 119, doi: 10.3847/1538-4357/acd54a

Pawlik, M. M., McAlpine, S., Trayford, J. W., et al. 2019, Nature Astronomy, 3, 440, doi: 10.1038/s41550-019-0725-z

Peebles, P. J. E. 1982, The Astrophysical Journal, 263, L1, doi: 10.1086/183911

Peng, Y.-j., Lilly, S. J., Kovač, K., et al. 2010, The Astrophysical Journal, 721, 193, doi: 10.1088/0004-637X/721/1/193

Perrotta, S., George, E. R., Coil, A. L., et al. 2021, The Astrophysical Journal, 923, 275, doi: 10.3847/1538-4357/ac2fa4

Perrotta, S., Coil, A. L., Rupke, D. S. N., et al. 2023, The Astrophysical Journal, 949, 9, doi: 10.3847/1538-4357/acc660

Pintos-Castro, I., Yee, H. K. C., Muzzin, A., Old, L., & Wilson, G. 2019, The Astrophysical Journal, 876, 40, doi: 10.3847/1538-4357/ab14ee

Poggianti, B. M., & Barbaro, G. 1997, Astronomy and Astrophysics, 325, 1025, doi: 10.48550/arXiv.astro-ph/9703067

Poggianti, B. M., von der Linden, A., De Lucia, G., et al. 2006, The Astrophysical Journal, 642, 188, doi: 10.1086/500666

Poggianti, B. M., Aragón-Salamanca, A., Zaritsky, D., et al. 2009, The Astrophysical Journal, 693, 112, doi: 10.1088/0004-637X/693/1/112

Popesso, P., Concas, A., Cresci, G., et al. 2022, Monthly Notices of the Royal Astronomical Society, 519, 1526, doi: 10.1093/mnras/stac3214

Pozzetti, L., Bolzonella, M., Zucca, E., et al. 2010, Astronomy and Astrophysics, 523, A13, doi: 10.1051/0004-6361/200913020

Prochaska, J. X., Kasen, D., & Rubin, K. 2011, The Astrophysical Journal, 734, 24, doi: 10.1088/0004-637X/734/1/24

Rich, J. A., Kewley, L. J., & Dopita, M. A. 2011, The Astrophysical Journal, 734, 87, doi: 10.1088/0004-637X/734/2/87

Roberts-Borsani, G. W., Saintonge, A., Masters, K. L., & Stark, D. V. 2020, Monthly Notices of the Royal Astronomical Society, 493, 3081, doi: 10.1093/mnras/staa464

Rowlands, K., Wild, V., Bourne, N., et al. 2018, Monthly Notices of the Royal Astronomical Society, 473, 1168, doi: 10.1093/mnras/stx1903

Rubin, K. H. R. 2017, in Gas Accretion onto Galaxies, ed. A. Fox & R. Davé (Cham: Springer International Publishing), 95–115, doi: 10.1007/978-3-319-52512-9_5

Rubin, K. H. R., Weiner, B. J., Koo, D. C., et al. 2010, The Astrophysical Journal, 719, 1503, doi: 10.1088/0004-637X/719/2/1503

Rupke, D. S., Veilleux, S., & Sanders, D. B. 2005a, The Astrophysical Journal Supplement Series, 160, 87, doi: 10.1086/432886

—. 2005b, The Astrophysical Journal Supplement Series, 160, 115, doi: 10.1086/432889

Rupke, D. S. N. 2018, Galaxies, 6, 138, doi: 10.3390/galaxies6040138

Rupke, D. S. N., & Veilleux, S. 2011, The Astrophysical Journal, 729, L27, doi: 10.1088/2041-8205/729/2/L27

Santini, P., Castellano, M., Fontana, A., et al. 2022, The Astrophysical Journal, 940, 135, doi: 10.3847/1538-4357/ac9a48

Santos, J. S., Altieri, B., Valtchanov, I., et al. 2015, Monthly Notices of the Royal Astronomical Society, 447, L65, doi: 10.1093/mnrasl/slu180

Sato, T., Martin, C. L., Noeske, K. G., Koo, D. C., & Lotz, J. M. 2009, The Astrophysical Journal, 696, 214, doi: 10.1088/0004-637X/696/1/214

Schawinski, K., Urry, C. M., Simmons, B. D., et al. 2014, Monthly Notices of the Royal Astronomical Society, 440, 889, doi: 10.1093/mnras/stu327

Schaye, J., Crain, R. A., Bower, R. G., et al. 2015, Monthly Notices of the Royal Astronomical Society, 446, 521, doi: 10.1093/mnras/stu2058

Schneider, E. E., & Robertson, B. E. 2018, The Astrophysical Journal, 860, 135, doi: 10.3847/1538-4357/aac329

Schreiber, N. M. F., & Wuyts, S. 2020, Annual Review of Astronomy and Astrophysics, 58, 661, doi: 10.1146/annurev-astro-032620-021910

Sell, P. H., Tremonti, C. A., Hickox, R. C., et al. 2014, Monthly Notices of the Royal Astronomical Society, 441, 3417, doi: 10.1093/mnras/stu636

Setton, D. J., Khullar, G., Miller, T. B., et al. 2024, UNCOVER NIRSpec/PRISM Spectroscopy Unveils Evidence of Early Core Formation in a Massive, Centrally Dusty Quiescent Galaxy at $z_{spec}=3.97$, arXiv, doi: 10.48550/arXiv.2402.05664

Sijacki, D., Vogelsberger, M., Genel, S., et al. 2015, Monthly Notices of the Royal Astronomical Society, 452, 575, doi: 10.1093/mnras/stv1340

Silk, J. 1977, The Astrophysical Journal, 211, 638, doi: 10.1086/154972

Silk, J., & Rees, M. J. 1998, Astronomy and Astrophysics, 331, L1, doi: 10.48550/arXiv.astro-ph/9801013

Simpson, C., Westoby, P., Arumugam, V., et al. 2013, Monthly Notices of the Royal Astronomical Society, 433, 2647, doi: 10.1093/mnras/stt940

Smercina, A., Smith, J. D. T., Dale, D. A., et al. 2018, The Astrophysical Journal, 855, 51, doi: 10.3847/1538-4357/aaafcd

Smercina, A., Smith, J.-D. T., French, K. D., et al. 2022, The Astrophysical Journal, 929, 154, doi: 10.3847/1538-4357/ac5d5f

Smith, R., Davies, J. I., & Nelson, A. H. 2010, Monthly Notices of the Royal Astronomical Society, no, doi: 10.1111/j.1365-2966.2010.16545.x

Socolovsky, M., Almaini, O., Hatch, N. A., et al. 2018, Monthly Notices of the Royal Astronomical Society, 476, 1242, doi: 10.1093/mnras/sty312

Sokal, K. R., Johnson, K. E., Indebetouw, R., & Massey, P. 2016, The Astrophysical Journal, 826, 194, doi: 10.3847/0004-637X/826/2/194

Sommariva, V., Mannucci, F., Cresci, G., et al. 2012, Astronomy and Astrophysics, 539, A136, doi: 10.1051/0004-6361/201118134

Soto, K. T., Martin, C. L., Prescott, M. K. M., & Armus, L. 2012, The Astrophysical Journal, 757, 86, doi: 10.1088/0004-637X/757/1/86

Springel, V., Di Matteo, T., & Hernquist, L. 2005, Monthly Notices of the Royal Astronomical Society, 361, 776, doi: 10.1111/j.1365-2966.2005.09238.x

Springel, V., & Hernquist, L. 2003, Monthly Notices of the Royal Astronomical Society, 339, 289, doi: 10.1046/j.1365-8711.2003.06206.x

Strateva, I., Ivezić, Z., Knapp, G. R., et al. 2001, The Astronomical Journal, 122, 1861, doi: 10.1086/323301

Sturm, E., González-Alfonso, E., Veilleux, S., et al. 2011, The Astrophysical Journal, 733, L16, doi: 10.1088/2041-8205/733/1/L16

Suess, K. A., Kriek, M., Price, S. H., & Barro, G. 2020, The Astrophysical Journal, 899, L26, doi: 10.3847/2041-8213/abacc9

Sun, Y., Lee, G.-H., Zabludoff, A. I., et al. 2024, Monthly Notices of the Royal Astronomical Society, 528, 5783, doi: 10.1093/mnras/stae366

Sureshkumar, U., Durkalec, A., Pollo, A., et al. 2024, Do galaxy mergers prefer underdense environments?, doi: 10.48550/arXiv.2402.18520

Tacchella, S., Conroy, C., Faber, S. M., et al. 2022, The Astrophysical Journal, 926, 134, doi: 10.3847/1538-4357/ac449b

Talia, M., Brusa, M., Cimatti, A., et al. 2017, Monthly Notices of the Royal Astronomical Society, 471, 4527, doi: 10.1093/mnras/stx1788

Taylor, E., Almaini, O., Merrifield, M., et al. 2023, Monthly Notices of the Royal Astronomical Society, 522, 2297, doi: 10.1093/mnras/stad1098

Taylor-Mager, V. A., Conselice, C. J., Windhorst, R. A., & Jansen, R. A. 2007, The Astrophysical Journal, 659, 162, doi: 10.1086/511806

Tomczak, A. R., Lemaux, B. C., Lubin, L. M., et al. 2019, Monthly Notices of the Royal Astronomical Society, 484, 4695, doi: 10.1093/mnras/stz342

Toomre, A., & Toomre, J. 1972, The Astrophysical Journal, 178, 623, doi: 10.1086/151823

Tran, K.-V. H., Franx, M., Illingworth, G., Kelson, D. D., & van Dokkum, P. 2003, The Astrophysical Journal, 599, 865, doi: 10.1086/379804

Tran, K.-V. H., Franx, M., Illingworth, G. D., et al. 2004, The Astrophysical Journal, 609, 683, doi: 10.1086/421237

Tran, K.-V. H., Papovich, C., Saintonge, A., et al. 2010, The Astrophysical Journal, 719, L126, doi: 10.1088/2041-8205/719/2/L126

Tremonti, C. A., Moustakas, J., & Diamond-Stanic, A. M. 2007, The Astrophysical Journal, 663, L77, doi: 10.1086/520083

van der Burg, R. F. J., McGee, S., Aussel, H., et al. 2018, Astronomy & Astrophysics, 618, A140, doi: 10.1051/0004-6361/201833572

van der Burg, R. F. J., Rudnick, G., Balogh, M. L., et al. 2020, Astronomy & Astrophysics, 638, A112, doi: 10.1051/0004-6361/202037754

van Dokkum, P. G. 2005, The Astronomical Journal, 130, 2647, doi: 10.1086/497593

van Dokkum, P. G., Franx, M., Fabricant, D., Kelson, D. D., & Illingworth, G. D. 1999, The Astrophysical Journal, 520, L95, doi: 10.1086/312154

Vazdekis, A., Koleva, M., Ricciardelli, E., Röck, B., & Falcón-Barroso, J. 2016, Monthly Notices of the Royal Astronomical Society, 463, 3409, doi: 10.1093/mnras/stw2231

Veilleux, S., Maiolino, R., Bolatto, A. D., & Aalto, S. 2020, The Astronomy and Astrophysics Review, 28, 2, doi: 10.1007/s00159-019-0121-9

Veilleux, S., Liu, W., Vayner, A., et al. 2023, The Astrophysical Journal, 953, 56, doi: 10.3847/1538-4357/ace10f

Vergani, D., Zamorani, G., Lilly, S., et al. 2010, Astronomy and Astrophysics, 509, A42, doi: 10.1051/0004-6361/200912802

Voit, G. M., Donahue, M., Bryan, G. L., & McDonald, M. 2015, Nature, 519, 203, doi: 10.1038/nature14167

von der Linden, A., Wild, V., Kauffmann, G., White, S. D. M., & Weinmann, S. 2010, Monthly Notices of the Royal Astronomical Society, 404, 1231, doi: 10.1111/j.1365-2966.2010.16375.x

Vulcani, B., Poggianti, B. M., Finn, R. A., et al. 2010, The Astrophysical Journal Letters, 710, L1, doi: 10.1088/2041-8205/710/1/L1

Wang, T., Elbaz, D., Daddi, E., et al. 2016, The Astrophysical Journal, 828, 56, doi: 10.3847/0004-637X/828/1/56

Weaver, J. R., Davidzon, I., Toft, S., et al. 2023, Astronomy and Astrophysics, 677, A184, doi: 10.1051/0004-6361/202245581

Weiner, B. J., Coil, A. L., Prochaska, J. X., et al. 2009, The Astrophysical Journal, 692, 187, doi: 10.1088/0004-637X/692/1/187

Werle, A., Poggianti, B., Moretti, A., et al. 2022, The Astrophysical Journal, 930, 43, doi: 10.3847/1538-4357/ac5f06

Wetzel, A. R., Tollerud, E. J., & Weisz, D. R. 2015, The Astrophysical Journal, 808, L27, doi: 10.1088/2041-8205/808/1/L27

Whitaker, K. E., Kriek, M., van Dokkum, P. G., et al. 2012, The Astrophysical Journal, 745, 179, doi: 10.1088/0004-637X/745/2/179

White, S. D. M., & Frenk, C. S. 1991, The Astrophysical Journal, 379, 52, doi: 10.1086/170483

White, S. D. M., & Rees, M. J. 1978, Monthly Notices of the Royal Astronomical Society, 183, 341, doi: 10.1093/mnras/183.3.341

Whitney, A., Ferreira, L., Conselice, C. J., & Duncan, K. 2021, The Astrophysical Journal, 919, 139, doi: 10.3847/1538-4357/ac1422

Wild, V., Almaini, O., Dunlop, J., et al. 2016, Monthly Notices of the Royal Astronomical Society, 463, 832, doi: 10.1093/mnras/stw1996

Wild, V., Kauffmann, G., Heckman, T., et al. 2007, Monthly Notices of the Royal Astronomical Society, 381, 543, doi: 10.1111/j.1365-2966.2007.12256.x

Wild, V., Walcher, C. J., Johansson, P. H., et al. 2009, Monthly Notices of the Royal Astronomical Society, 395, 144, doi: 10.1111/j.1365-2966.2009.14537.x

Wild, V., Almaini, O., Cirasuolo, M., et al. 2014, Monthly Notices of the Royal Astronomical Society, 440, 1880, doi: 10.1093/mnras/stu212

Wild, V., Aldeen, L. T., Carnall, A., et al. 2020, Monthly Notices of the Royal Astronomical Society, 494, 529, doi: 10.1093/mnras/staa674

Wilkinson, A., Almaini, O., Wild, V., et al. 2021, Monthly Notices of the Royal Astronomical Society, 504, 4533, doi: 10.1093/mnras/stab965

Williams, R. J., Quadri, R. F., Franx, M., van Dokkum, P., & Labbé, I. 2009, The Astrophysical Journal, 691, 1879, doi: 10.1088/0004-637X/691/2/1879

Worthey, G. 1994, The Astrophysical Journal Supplement Series, 95, 107, doi: 10.1086/192096

Worthey, G., & Ottaviani, D. L. 1997, The Astrophysical Journal Supplement Series, 111, 377, doi: 10.1086/313021

Wright, A. H., Driver, S. P., & Robotham, A. S. G. 2018, Monthly Notices of the Royal Astronomical Society, 480, 3491, doi: 10.1093/mnras/sty2136

Wu, P.-F. 2024, Ejective feedback as a quenching mechanism in the 1.5 billion years of the universe: detection of neutral gas outflow in a $z=4$ recently quenched galaxy, doi: 10.48550/arXiv.2409.00471

Wuyts, S., Förster Schreiber, N. M., van der Wel, A., et al. 2011, The Astrophysical Journal, 742, 96, doi: 10.1088/0004-637X/742/2/96

Yan, R., Newman, J. A., Faber, S. M., et al. 2006, The Astrophysical Journal, 648, 281, doi: 10.1086/505629

Yano, M., Kriek, M., van der Wel, A., & Whitaker, K. E. 2016, The Astrophysical Journal, 817, L21, doi: 10.3847/2041-8205/817/2/L21

Yoon, Y., Kim, J.-W., & Ko, J. 2023, The Astrophysical Journal, 957, 59, doi: 10.3847/1538-4357/acfed5

York, D. G., Adelman, J., Anderson, Jr., J. E., et al. 2000, The Astronomical Journal, 120, 1579, doi: 10.1086/301513

Young, L. M., Bendo, G. J., & Lucero, D. M. 2009, The Astronomical Journal, 137, 3053, doi: 10.1088/0004-6256/137/2/3053

Zabludoff, A. I., Zaritsky, D., Lin, H., et al. 1996, The Astrophysical Journal, 466, 104, doi: 10.1086/177495

Zhu, G., Ménard, B., Bizyaev, D., et al. 2014, Monthly Notices of the Royal Astronomical Society, 439, 3139, doi: 10.1093/mnras/stu186

Zubovas, K., & Maskeliūnas, G. 2023, Monthly Notices of the Royal Astronomical Society, 524, 4819, doi: 10.1093/mnras/stad1661